Title

Direct Observation of Extrasolar Planets and the Development of the Gemini Planet Imager Integral Field Spectrograph

Permalink

https://escholarship.org/uc/item/2rz2v5xb

Author

Chilcote, Jeffrey

Publication Date

2014

UNIVERSITY OF CALIFORNIA
Los Angeles

Direct Observation of Extrasolar Planets and the Development of the Gemini Planet Imager Integral Field Spectrograph

A dissertation submitted in partial satisfaction
of the requirements for the degree
Doctor of Philosophy in Astronomy

by

Jeffrey Kaplan Chilcote

2014

Abstract of the Dissertation

Direct Observation of Extrasolar Planets and the Development of the Gemini Planet Imager Integral Field Spectrograph

by

Jeffrey Kaplan Chilcote

Doctor of Philosophy in Astronomy

University of California, Los Angeles, 2014

Professor James Larkin, Chair

This thesis is focused on the development and testing of a new instrument capable of finding and characterizing recently-formed Jupiter-sized planets orbiting other stars. To observe these planets, I present the design, construction and testing of the Gemini Planet Imager (GPI) Integral Field Spectrograph (IFS). GPI is a facility class instrument for the Gemini Observatory with the primary goal of directly detecting young Jovian planets. The GPI IFS utilizes an infrared transmissive lenslet array to sample a rectangular 2.7 × 2.7 arcsecond field of view and provide low-resolution spectra across five bands between 1 and 2.5 μm. The dispersing element can be replaced with a Wollaston prism to provide broadband polarimetry across the same five filter bands. The IFS construction was based at the University of California, Los Angeles in collaboration with the Université de Montréal, Immervision and Lawrence Livermore National Laboratory.

I will present performance results, from in-lab testing, of the Integral Field Spectrograph (IFS) for the Gemini Planet Imager (GPI). The IFS is a large, complex, cryogenic, optical system requiring several years of development and testing. I will present the design and integration of the mechanical and optical performance of the spectrograph optics. The IFS passed its pre-ship review in

2011 and was shipped to University of California, Santa Cruz for integration with the remaining sub-systems of GPI. The UCLA built GPI IFS was integrated with the rest of GPI and is delivering high quality spectral datacubes of GPI's coronagraphic field.

Using the NIRC2 instrument located at the Keck Observatory, my collaborators and I observed the planetary companion to beta Pictoris in L' (3.5–4.1μm). Observations taken in the fall of 2009 and 2012 are used to find the location and inclination of the planet relative to the massive debris disk orbiting beta Pictoris. We find that the planet's orbit has a position angle on the sky of 211.9 ± 0.4 degrees, making the planet misaligned by 2.9 ± 0.5 degrees from the main disk, consistent with other observations that β Pic b is misaligned with the main disk, and part of the misaligned inner disk. In 2009 & 2012 we find a projected orbital separation of 312.8 ± 18.3 and 466.35 ± 8.4 milliarcseconds consistent with an orbital period of ~ 20 years, and a semi-major axis of ~ 9 AU as found by Macintosh et al. (2014).

During the first commissioning observations with the Gemini Planet Imager (GPI), my collaborators and I took the first H-band spectrum of the planetary companion to the nearby young star beta Pictoris. The spectrum has a resolving power of $\sim$ 45 and demonstrates the distinctive triangular shape of a cool substellar object with low surface gravity. Using atmospheric models, we find an effective temperature of 1650 $\pm$50 K and a surface gravity of $\log(g) = 4.0 \pm 0.25$ (cgs units). These values agree well with predictions from planetary evolution models for a gas giant with mass between 10 and 12 M_{Jup} and age between 10 and 20 Myrs. The spectrum is very similar to a known low mass field brown dwarf but has more flux at the long wavelength end of the filters compared to models. Given the very high signal-to-noise of our spectrum this likely indicates additional physics such as patchy clouds that need to be included in the model.

The dissertation of Jeffrey Kaplan Chilcote is approved.

Kevin McKeegan

Michael Fitzgerald

James Larkin, Committee Chair

University of California, Los Angeles
2014

For my family

Table of Contents

List of Figures

List of Tables

Acknowledgments

I owe thanks to more people than I can possibly express in one document. First, I owe a huge thanks to my advisor, James Larkin. He has allowed me the independence to do unique and inspiring work while at the same time encouraging me and teaching me more than I could have ever imagined. He has pushed me to be better than I was before, but has given me the freedom to find my own path. Further, I want to thank James for being more than just an advisor, but also a true friend. I also owe thanks to Michael Fitzgerald for being an advisor to me. He has been patient and encouraging not only in my science work, but has been a source of sound advice. I want to thank Bruce Macintosh for supporting me, encouraging me, allowing me to be part of a truly groundbreaking instrument, for all the help he has given me and for his advice over the years. Beyond their roles as my advisors, I owe great thanks to Ian Mclean, James Larkin, and Michael Fitzgerald for organizing and maintaining an absolutely phenomenal lab that truly supports and engages graduate students in instrumentation. I owe many thanks to every member of the lab. Thanks to Chris Johnson for all his advice, friendship, and IT support over the years. Thanks to Jason Weiss for all his software support and conversations. Thanks to Eric Wang for constantly working with all the engineering changes that we underwent. Thanks to Ken Magnone for his knowledge. Thanks to Ted Aliado for making things fit when they originally did not. I am also thankful for having had the opportunity to have interacted with an amazing group of graduate students. I especially want to acknowledge those who have become my true friends. They have helped to keep me upright and on course in the good times and the bad. Thank you to Kathy Kornei for being an amazing officemate. Having put up with me for several years and always being a friend to talk with. Thank you to Breann Sitarski for always being invaluable. Thanks to Kristin Kulas and Sarah Logsdon for being fellow lab rats and for living through the highs and lows of instrumentation with me. Thanks to Greg Mace,

the only other member of my entering class, for having battled through six years of graduate school with me. Thanks to Shane Frewen for being someone to talk with. Thanks to Fred Davies and Nate Ross for being someone to bounce ideas off of when I ended up confusing myself. And thank you to Tom Esposito and Kevin Hainline for working on the planetarium with me. I also owe a special thanks to my mom, dad, and brother for their support over these many years. I am not sure where I would be without them. Finally, thank you to everyone for all that you have done, it has meant so much to me.

VITA

2007–2008	Research Assistant, Physics and Astronomy Department, Northwestern University, Evanston, Illinois.
2008	B.A. (Physics with honors) and B.A. (Mathematics), Northwestern University.
2008–2009	Teaching Assistant, Physics and Astronomy Department, UCLA, Los Angeles, California.
2008–2009	UCLA Chancellors Prize.
2009–2013	Research Assistant, Physics and Astronomy Department, UCLA, Los Angeles, California.
2010	M.S. (Astronomy), UCLA, Los Angeles, California.
2012–2013	Bachmann Graduate Fellowship for Astronomical Instrumentation
2013–2014	Dissertation Year Fellow - Research Assistant, Physics and Astronomy Department, UCLA, Los Angeles, California.
2014	Research Assistant, Physics and Astronomy Department, UCLA, Los Angeles, California.

PUBLICATIONS

Chilcote, Jeffrey; Barman, Travis; Fitzgerald, Michael P.; Graham, James R.; Larkin, James E.; Macintosh, Bruce; Bauman, Brian; Burrows, Adam S.;

Cardwell, Andrew; De Rosa, Robert J.; Dillon, Daren; Doyon, Rene; Dunn, Jennifer; Erikson, Darren; Gavel, Donald; Goodsell, Stephen J.; Hartung, Markus; Hibon, Pascale; Ingraham, Patrick; Kalas, Paul; Konopacky, Quinn; Maire, Jrme; Marchis, Franck; Marley, Mark S.; Marois, Christian; Millar-Blanchaer, Max; Morzinski, Katie; Norton, Andrew; Oppenheimer, B. R.; Palmer, David; Patience, Jennifer; Perrin, Marshall D.; Poyneer, Lisa; Pueyo, Laurent; Rantakyr, Fredrik; Sadakuni, Naru; Saddlemyer, Leslie; Savransky, Dmitry; Serio, Andrew; Sivaramakrishnan, Anand; Song, Inseok; Soummer, Remi; Thomas, Sandrine; Wallace, J. Kent; Wiktorowicz, Sloane J.; Wolff, Schuyler, *"The First H-band Spectrum of the Massive Gas Giant Planet beta Pictoris b with the Gemini Planet Imager,"* Submitted ApJL 15 July, 2014

Perrin, Marshall D.; Duchene, Gaspard; Millar-Blanchaer, Max; Fitzgerald, Michael P.; Graham, James R.; Wiktorowicz, Sloane J.; Kalas, Paul G.; Macintosh, Bruce; Bauman, Brian; Cardwell, Andrew; Chilcote, Jeffrey; De Rosa, Robert J.; Dillon, Daren; Doyon, Ren; Dunn, Jennifer; Gavel, Donald; Goodsell, Stephen; Hartung, Markus; Hibon, Pascale; Ingraham, Patrick; Kerley, Daniel; Konapacky, Quinn; Larkin, James E.; Maire, Jrme; Marchis, Franck; Marois, Christian; Mittal, Tushar; Morzinski, Katie M.; Oppenheimer, B. R.; Palmer, David W.; Patience, Jennifer; Poyneer, Lisa; Pueyo, Laurent; Rantakyr, Fredrik T.; Sadakuni, Naru; Saddlemyer, Leslie; Savransky, Dmitry; Soummer, Rmi; Sivaramakrishnan, Anand; Song, Inseok; Thomas, Sandrine; Wallace, J. Kent; Wang, Jason J.; Wolff, Schuyler G., *"Polarimetry with the Gemini Planet Imager: Methods, Performance at First Light, and the Circumstellar Ring around HR 4796A,"* Submitted to the Astrophysical Journal, 2014

Larkin, James E.; Chilcote, Jeffrey K.; Aliado, Theodore; Bauman, Brian J.; Brims, George; Canfield, John M.; Cardwell, Andrew; Dillon, Daren; Doyon, Ren;

Dunn, Jennifer; Fitzgerald, Michael P.; Graham, James R.; Goodsell, Stephen; Hartung, Markus; Hibon, Pascale; Ingraham, Patrick; Johnson, Christopher A; Kress, Evan; Konopacky, Quinn M.; Macintosh, Bruce A.; Magnone, Kenneth G.; Maire, Jrme; McLean, Ian S.; Palmer, David; Perrin, Marshall D.; Quiroz, Carlos; Rantakyr, Fredrik; Sadakuni, Naru; Saddlemyer, Leslie; Serio, Andrew; Thibault, Simon; Thomas, Sandrine J.; Vallee, Philippe; Weiss, Jason L. *"The Integral Field Spectrograph for the Gemini Planet Imager,"* Society of Photo-Optical Instrumentation Engineers (SPIE) Conference Series, Vol 9147-55, 2014

Rantakyr, Fredrik T.; Cardwell, Andrew; Chilcote, Jeffrey; Dunn, Jennifer; Goodsell, Stephen; Hibon, Pascale; Macintosh, Bruce; Quiroz, Carlos; Perrin, Marshall D.; Sadakuni, Naru; Saddlemyer, Leslie; Savransky, Dmitry; Serio, Andrew; Winge, Claudia; Galvez, Ramon; Gausachs, Gaston; Hardie, Kayla; Hartung, Markus; Luhrs, Javier; Poyneer, Lisa; Thomas, Sandrine *"Gemini Planet Imager integration to the Gemini South telescope software environment,"* Society of Photo-Optical Instrumentation Engineers (SPIE) Conference Series, Vol 9149-87, 2014

Wiktorowicz, Sloane J.; Millar-Blanchaer, Max; Perrin, Marshall D.; Graham, James R.; Fitzgerald, Michael P.; Maire, Jrme; Ingraham, Patrick; Savransky, Dmitry; Macintosh, Bruce A.; Thomas, Sandrine J.; Chilcote, Jeffrey K.; Draper, Zachary H.; Song, Inseok; Cardwell, Andrew; Goodsell, Stephen J.; Hartung, Markus; Hibon, Pascale; Rantakyr, Fredrik; Sadakuni, Naru; the GPI team *"Gemini Planet Imager Observational Calibrations VII: On-Sky Polarimetric Performance of the Gemini Planet Imager,"* Society of Photo-Optical Instrumentation Engineers (SPIE) Conference Series, Vol 9147-305, 2014

Maire, Jrme; Ingraham, Patrick J.; De Rosa, Robert J.; Perrin, Marshall D.; Rajan, Abhijith; Savransky, Dmitry; Wang, Jason J.; Ruffio, Jean-Baptiste; Wolff, Schuyler G.; Chilcote, Jeffrey K.; Doyon, Ren; Graham, James R.; Greenbaum, Alexandra Z.; Konopacky, Quinn M.; Larkin, James E.; Macintosh, Bruce A.; Marois, Christian; Millar-Blanchaer, Max; Patience, Jennifer; Pueyo, Laurent A.; Sivaramakrishnan, Anand; Thomas, Sandrine J.; Weiss, Jason L. *"Gemini Planet Imager Observational Calibrations VI: Photometric and Spectroscopic Calibration for the Integral Field Spectrograph,"* Society of Photo-Optical Instrumentation Engineers (SPIE) Conference Series, Vol 9147-307, 2014

Konopacky, Quinn M.; Thomas, Sandrine J.; Macintosh, Bruce A.; Dillon, Daren; Sadakuni, Naru; Maire, Jrme; Fitzgerald, Michael; Hinkley, Sasha; Kalas, Paul; Esposito, Thomas; Marois, Christian; Ingraham, Patrick J.; Marchis, Franck; Perrin, Marshall D.; Graham, James R.; Wang, Jason J.; De Rosa, Robert J.; Morzinski, Katie; Pueyo, Laurent; Chilcote, Jeffrey K.; Larkin, James E.; Fabrycky, Daniel; Goodsell, Stephen J.; Oppenheimer, B. R.; Patience, Jenny; Saddlemyer, Leslie; Sivaramakrishnan, Anand *"Gemini Planet Imager Observational Calibrations V: Astrometry and Distortion,"* Society of Photo-Optical Instrumentation Engineers (SPIE) Conference Series, Vol 9147-306, 2014

Ingraham, Patrick; Perrin, Marshall D.; Sadakuni, Naru; Ruffio, Jean-Baptiste; Maire, Jerome; Chilcote, Jeff; Larkin, James; Marchis, Franck; Galicher, Raphael; Weiss, Jason *"Gemini Planet Imager Observational Calibrations II: Detector Performance and Calibration,"* Society of Photo-Optical Instrumentation Engineers (SPIE) Conference Series, Vol 9147-286, 2014

Perrin, Marshall D.; Maire, Jrme; Ingraham, Patrick; Savransky, Dmitry;

Millar-Blanchaer, Max; Wolff, Schuyler G.; Ruffio, Jean-Baptiste; Wang, Jason J.; Draper, Zachary H.; Sadakuni, Naru; Marois, Christian; Rajan, Abhijith; Fitzgerald, Michael P.; Macintosh, Bruce; Graham, James R.; Doyon, Ren; Larkin, James E.; Chilcote, Jeffrey K.; Goodsell, Stephen J.; Palmer, David W.; Labrie, Kathleen; Beaulieu, Mathilde; De Rosa, Robert J.; Greenbaum, Alexandra Z.; Hartung, Markus; Hibon, Pascale; Konopacky, Quinn; Lafreniere, David; Lavigne, Jean-Francois; Marchis, Franck; Patience, Jenny; Pueyo, Laurent; Rantakyr, Fredrik T.; Soummer, Rmi; Sivaramakrishnan, Anand; Thomas, Sandrine; Ward-Duong, Kimberly; Wiktorowicz, Sloane *"Gemini Planet Imager Observational Calibrations I: Overview of the GPI Data Reduction Pipeline,"* Society of Photo-Optical Instrumentation Engineers (SPIE) Conference Series, Vol 9147-133, 2014

Poyneer, Lisa A.; De Rosa, Robert J.; Macintosh, Bruce; Palmer, David W.; Perrin, Marshall D.; Sadakuni, Naru; Savransky, Dmitry; Bauman, Brian; Cardwell, Andrew; Chilcote, Jeffrey K.; Dillon, Daren; Gavel, Donald; Goodsell, Stephen J.; Hartung, Markus; Hibon, Pascale; Rantakyro, Fredrik T.; Thomas, Sandrine; Veran, Jean-Pierre *"On-sky performance during verification and commissioning of the Gemini Planet Imager's adaptive optics system,"* Society of Photo-Optical Instrumentation Engineers (SPIE) Conference Series, Vol 9148, 2014

Macintosh, Bruce; Graham, James R.; Ingraham, Patrick; Konopacky, Quinn; Marois, Christian; Perrin, Marshall; Poyneer, Lisa; Bauman, Brian; Barman, Travis; Burrows, Adam; Cardwell, Andrew; Chilcote, Jeffrey; De Rosa, Robert J.; Dillon, Daren; Doyon, Rene; Dunn, Jennifer; Erikson, Darren; Fitzgerald, Michael; Gavel, Donald; Goodsell, Stephen; Hartung, Markus; Hibon, Pascale; Kalas, Paul G.; Larkin, James; Maire, Jerome; Marchis, Franck; Marley,

Mark; McBride, James; Millar-Blanchaer, Max; Morzinski, Katie; Norton, Andew; Oppenheimer, B. R.; Palmer, Dave; Patience, Jennifer; Pueyo, Laurent; Rantakyro, Fredrik; Sadakuni, Naru; Saddlemyer, Leslie; Savransky, Dmitry; Serio, Andrew; Soummer, Remi; Sivaramakrishnan, Anand; Song, Inseok; Thomas, Sandrine; Wallace, J. Kent; Wiktorowicz, Sloane; Wolff, Schuyler, The Gemini Planet Imager: First Light, Proc. Natl. Acad. Sci, (2014).

Hartung, M., Macintosh, B., Poyneer, L., Savransky, D., Gavel, D., Palmer, D., Thomas, S., Dillon, D., Chilcote, J., Ingraham, P., Sadakuni, N., Wallace, K., Perin, M. D., Marois, C., Maire, J., Rantakyro, F., Hibon, P., Saddlemyer, L., Goodsell, S. *"Final A&T Stages of the Gemini Planet Finder."* Proceedings of AO4ELT3 conference, Florence, Italy, May 2013

Chilcote, Jeffrey K.; Larkin, James E.; Maire, Jrme; Perrin, Marshall D.; Fitzgerald, Michael P.; Doyon, Ren; Thibault, Simon; Bauman, Brian; Macintosh, Bruce A.; Graham, James R.; Saddlemyer, Les. *"Performance of the integral field spectrograph for the Gemini Planet Imager."* Ground-based and Airborne Instrumentation for Astronomy IV. Proceedings of the SPIE, Volume 8446. Amsterdam, Netherlands. July 1–6, 2012.

Maire, Jerome; Perrin, Marshall D.; Doyon, Ren; Chilcote, Jeffrey; Larkin, James E.; Weiss, Jason L.; Marois, Christian; Konopacky, Quinn M.; Millar-Blanchaer, Maxwell; Graham, James R.; Dunn, Jennifer; Galicher, Raphael; Marchis, Franck; Wiktorowicz, Sloane J.; Labrie, Kathleen; Thomas, Sandrine J.; Goodsell, Stephen J.; Rantakyro, Fredrik T.; Palmer, David W.; Macintosh, Bruce A. *"Test results for the Gemini Planet Imager data reduction pipeline."* Software and Cyberinfrastructure for Astronomy II. Proceedings of the SPIE, Volume 8451. Amsterdam, Netherlands. July 1–6, 2012.

Macintosh, Bruce A.; Anthony, Andre; Atwood, Jennifer; Barriga, Nicolas; Bauman, Brian; Caputa, Kris; Chilcote, Jeffery; Dillon, Daren; Doyon, Ren; Dunn, Jennifer; Gavel, Donald T.; Galvez, Ramon; Goodsell, Stephen J.; Graham, James R.; Hartung, Markus; Isaacs, Joshua; Kerley, Dan; Konopacky, Quinn; Labrie, Kathleen; Larkin, James E.; Maire, Jerome; Marois, Christian; Millar-Blanchaer, Max; Nunez, Arturo; Oppenheimer, Ben R.; Palmer, David W.; Pazder, John; Perrin, Marshall; Poyneer, Lisa A.; Quirez, Carlos; Rantakyro, Frederik; Reshtov, Vlad; Saddlemyer, Leslie; Sadakuni, Naru; Savransky, Dmitry; Sivaramakrishnan, Anand; Smith, Malcolm; Soummer, Remi; Thomas, Sandrine; Wallace, J. Kent; Weiss, Jason; Wiktorowicz, Sloane. *"The Gemini Planet Imager: integration and status."* Ground-based and Airborne Instrumentation for Astronomy IV. Proceedings of the SPIE, Volume 8446. Amsterdam, Netherlands. July 1–6, 2012.

Jeffrey K. Chilcote, J. E. Larkin, R. Doyon, M. P. Fitzgerald, J R. Graham, B.A. Macintosh, D.W. Palmer, L.Saddlemyer, *"Test Results for the Integral Field Spectrograph for the Gemini Planet Imager."* Extreme Solar Systems II. Jackson Lake Lodge, Grand Teton National Park, Moran, Wyoming. September 11–17, 2011.

Jeffrey K. Chilcote, James E. Larkin, Jerome Maire, Marshall D. Perrin, Ren Doyon, Simon Thibault, Philippe Valle, Bruce. A. Macintosh, James R. Graham, Les Saddlemyer, David W. Palmer and the Gemini Planet Imager team, *"Test Results for the Integral Field Spectrograph for the Gemini Planet Imager."* Exploring Strange New Worlds: From Giant Planets to Super Earths. High Country Conference Center, Flagstaff, AZ. May 1-6, 2011.

Perrin, M., Fitzgerald, M., Chilcote, J., Wiktorowicz, S., Graham, J., Poyneer, L., Macintosh, B. *"Circumstellar Disk Studies with the Gemini Planet Imager: Simulations and Sensitivities."* Gemini Planet Imager team, American Astronomical Society, AAS Meeting #217, #339.04; Bulletin of the American Astronomical Society, Vol. 43, 2011. January 9–13, 2011

Chilcote, J., Larkin, J., Perrin, M., *"Test Results for the Integral Field Spectrograph for the Gemini Planet Imager."* Proceedings of In the Spirit of Lyot 2010: Direct Detection of Exoplanets and Circumstellar Disks. University of Paris Diderot. Paris, France. October 25 – 29, 2010.

Perrin, M. Larkin, J. Doyon, R., Thibault, S. Chilcote, J. Valle, P. Maire, J. Macintosh, B. Graham, J. et.al. *"The Integral Field Spectrograph of the Gemini Planet Imager."* Proceedings of In the Spirit of Lyot 2010: Direct Detection of Exoplanets and Circumstellar Disks. University of Paris Diderot. Paris, France. October 25 – 29, 2010.

Chilcote, J., Larkin, J., Aliado, T., Brims, G., Canfield, J., Corlies, L., et.al. *"Status of the Integral Field Spectrograph for the Gemini Planet Imager."* American Astronomical Society, AAS Meeting #215, #441.15; Bulletin of the American Astronomical Society, Vol. 42, p.403. January 3–7, 2010.

CHAPTER 1

Introduction

1.1 Motivation

Since the discovery of 51 Pegasi in 1995 (Mayor & Queloz, 1995), the search for and discovery of extrasolar planets has become a rapidly developing and exciting field of scientific research. However, to date almost all of the discovered planets and planet candidates have been found by the indirect techniques of radial velocity measurements (e.g., Marcy & Butler, 1996; Howard et al., 2010) and transit searches (e.g., Charbonneau et al., 2000; Lissauer et al., 2011; Batalha et al., 2012). The majority of the planetary systems that have been found have architectures radically different from our own solar system, many with giant planets orbiting much closer to their sun than expected two decades ago. These disparate extrasolar planetary systems have caused us to re-evaluate the processes for their development and have challenged our understanding of solar system formation. But given the inability of indirect searches to find solar systems like our own, we remain ignorant whether or not solar systems architectures like our own are typical or not and struggle to produce a comprehensive model.

Central to our understanding of solar system formation is the role of ices in the outer solar system. The explanation encompassing our own terestrial and Jovian planets and the solar systems discovered so far involves scattering the outer Jovians into the inner solar system. But, we have not been able to observe many systems with a planetary architecture similar to our own solar system.

Indirect techniques such as radial velocity surveys and transit surveys infer the presence of a planet by its effect on the more readily observed host star. Radial velocity measurements are derived from the fact that the center of mass of any solar system is not the center of mass of the star itself but is the center of mass of the entire solar system. All of the objects in a solar system including the central star orbit around this center of mass. The orbit of the central star causes spectral lines of the star to become blue or red Doppler shifted as the star moves towards or away from us respectively during its orbit. Fine measurements of this Doppler shift can be used to determine the existence of planetary mass companions.

Alternatively, the transit search technique is used to infer the presence of a planet by measuring a slight decrease in the light of a planet's host star as the planet transits between the observer and the star. The phenomenally successful Kepler spacecraft has used the transit method. Neither the Doppler nor transit techniques observe the planet directly, but look for the indirect effects that a planetary companion has upon its star.

Radial velocity and transit techniques have increasing difficulty detecting planets at wide separations from their host star. Radial velocity surveys require a significant portion of the orbit to be observed. For wide orbital separations, this requires a substantial amount of time and a quiet, stable star and spectrograph. Transit surveys not only require a long period of time, but the chance of alignment of the planet, star, and observer at wide separations becomes vanishingly small. While indirect methods are well suited for searching the region in close proximity to their host star these difficulties make indirect methods less effective at looking for solar system bodies, like our own Jovian planets, in wider orbits. Indirect observation methods are inefficient at observing past the "ice line" – the region in protoplanetary disks where it is cold enough for hydrogen compounds such as water, ammonia, and methane to condense into solid ice grains. To search for planets in wider orbits we must turn to different techniques.

Direct imaging of extrasolar planets is a nascent technique, which allows for the discovery of planets in wide orbits, provides new insight into the formation and characteristics of extrasolar systems as well as enabling spectroscopic observation of their atmospheres. Although planets in our own solar system are primarily imaged through reflected light from the sun, this typically makes a planet only one billionth as bright as its host star and no extrasolar planets have been imaged in reflected light.

Instead direct imaging focuses on young solar systems where planets are self-luminous. Heat generated during their formation causes planets to be highly luminous in the infrared (IR) when they are young. By investigating planets in wide orbits the ability to directly detect Jovian planets opens up new regions of extrasolar planet phase space (Figure 1.1) that in turn will inform our understanding of the processes through which these systems form.

The first step in the challenge of direct extrasolar planetary imaging is building a new generation of dedicated instruments to explore the young hot Jupiters in the 5–40 AU region, unreachable with Doppler and transit methods, but accessible from ground based facilities using state of the art technology. Instruments such as Palomar/P1640 (Oppenheimer et al., 2012), Gemini/GPI (Macintosh et al., 2012, 2014), and VLT/SPHERE (Beuzit et al., 2008) have been recently built and more, like Subaru/CHARIS (Peters et al., 2012), are under construction. These instruments are dedicated to searching for and characterizing these young extrasolar planets.

Direct imaging of extrasolar planets will allow new observations opening new horizons on our understanding of extrasolar planet formation. These accomplishments cannot be attained through theoretical analysis of the current data, but require us to establish statistics and make observations that help us to understand such information as planetary masses, orbital elements, and host star properties, including an understanding of their atmospheric chemistry and

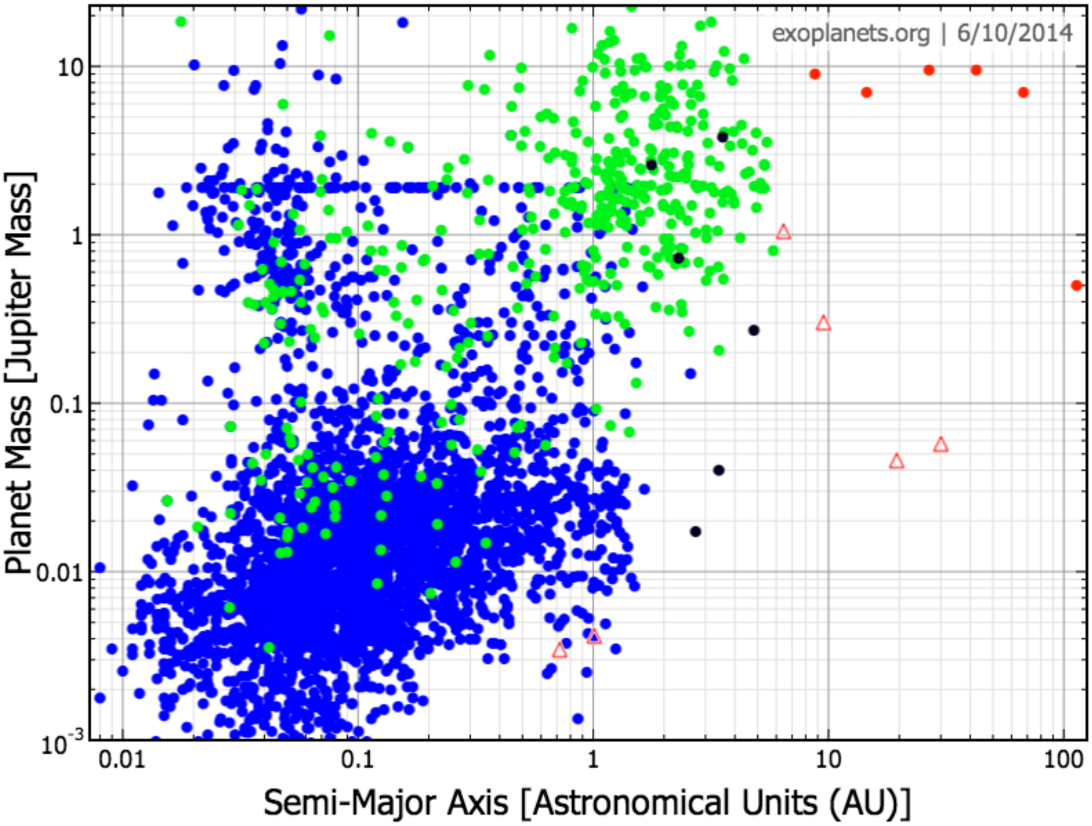

Figure 1.1: The known extrasolar planets (Transit/Blue, Radial Velocity/Green, Microlensing/Black, Direct Imaging/Red, Solar System Planets/Orange-Triangle). The number of planets which have been discovered via direct imaging is small, but has the potential to expand into the relatively unpopulated high-mass and high semi-major axis area of of the Mass versus Semi-major phase space (Wright et al., 2011).

the processes that they underwent during formation.

There are two competing models of Jovian planet formation commonly referred to as “hot-start” (Burrows et al., 1997) and “cold-start” (Pollack et al., 1996; Marley et al., 2007). “Hot-start” models are where planets are formed by disk instability, where if a disk is sufficiently massive, the disk fragments into a dense core, and the planet cool from an initial hot state. The gas that collapses directly to form a giant planet retains most of it initial entropy, resulting in high initial temperature. “Cold-start” models are where giant planet formation is a result of core accretion, where a heavy element core is built by the accretion of planetesimals and as the core grows, its ability to accrete gas from the surrounding disk increases. This process cools the gas, causing it to lose much of its initial entropy, and forms a giant planet that has a lower initial temperature. For a planet of a given mass and young age, hot start models predict more luminous planets. Even with a well determined stellar age, determining the planet's mass is difficult especially with only photometry. The key is to take spectra of the planet to determine which molecules are present and to constrain the scale height and temperature of the atmosphere which in turn yields mass.

We are just beginning to take the initial steps in our understanding of the giant planets that form beyond the "ice-line". Direct imaging of extrasolar planets is an exceptional technique, distinctly separate from other indirect techniques, fraught with its own set of unique challenges which require novel solutions. As we push closer to the parent star, and towards smaller, older, and fainter objects, even newer techniques, technology, and dedicated specialty built instruments will be required to image this challenging zone. However, this scientific advancement is not a trivial step; it has the potential to considerably advance our models and understanding of the makeup and formation processes present in extrasolar planetary systems.

1.2 Direct Imaging

The primary challenge of directly imaging a planet is differentiating it from the light from its host star. For stars under consideration, the distances are typically tens of parsecs from the Earth which places their potential outer solar systems less than one arc second in radius. But due to turbulence in the atmosphere, light from the star is traditionally blurred into a halo of light called the point spread function (PSF) with an angular full width at half maximum of approximately one arc second. So even with significant self-luminosity, the light of a planet is completely swamped by star light. Hubble Space Telescope is above the atmosphere but is a relatively small telescope and diffracted and scattered light from its optical system can still make the discovery of even bright exoplanets difficult. The first discovery of an exoplanet using its own emission was made with a modern adaptive optics (AO) system at the W.M. Keck Observatory (Marois et al., 2008).

An adaptive optics system is one of a variety of optical systems that measures the optical effect of turbulence in the atmosphere and in real-time uses a deformable mirror to restore a fraction of the light to an ideal plane wave limited by telescope diffraction. The performance of any AO system is limited by the rate of its operation (typically a few hundred hertz to a kilohertz), inaccuracies in its atmospheric measurements and the number of degrees of freedom (actuators on one or more deformable mirrors) it can control. As large telescopes in the mid-90's began installing AO systems, it became common to produce stellar PSFs smaller than 0.1 arc seconds in diameter with 30% or more of the light restored to this inner core. But, with the remainder of the light still uncontrolled and spread over a large PSF, planets remained undetected.

In parallel with these early AO systems, algorithms for modeling and removing the stellar light in the PSF made considerable progress and are of comparable importance to the detection of planets. Much of the early work focused on the Hubble Space Telescope where the atmosphere was gone and the PSF remained stable for long periods of time (but still typically less than a full orbit). The diffraction dominated PSF was largely symmetric under rotations of 90 degrees which led to a very successful technique of taking two or more images of a star at different telescope rotations and then subtracting one image from the other. A planet, disk or other faint structure would be different in the two images and would not subtract out or would partially remain (Schneider & Silverstone, 2003). But even in space, irregularities of the optics create unique and asymmetric diffractive effects called speckles and typically limit contrast within one arc second of a star to roughly 10^{-5}.

From the ground, speckles and diffraction from the telescope and optics are normally minor compared to the effects of the atmosphere. But, as AO systems improved, instrumental effects became more and more important. Many speckles are thought to be quasi-static in that they slowly vary with time, ambient temperature, pressure, mechanical flexure, guiding errors, and other phenomena (Marois et al., 2005a,b, 2006; Hinkley et al., 2007). All variations within the PSF show some level of time stability and there are several symmetries of the PSF which can help to remove the starlight and reveal a planet. These PSF symmetries fall into two categories of either spatial structure, such as an azimuthally symmetric component, or predictable wavelength dependency. Diffractive effects in particular have a predictable wavelength dependency making it possible to scale portions of the PSF at one wavelength to another and this was a prime motivator for building an integral field spectrograph for the science instrument of GPI.

The latest techniques for modeling the PSF use angular differential imaging (ADI, Marois et al. (2005b); Liu (2004)) and/or spectral differential imaging (SDI, McElwain et al. (2007)) to allow techniques such as locally optimized combination of images (LOCI, Lafrenière et al. (2007)) to build reference PSFs. The algorithms are detailed in chapter 4 where I apply them to imaging data on Beta Pictoris b and in chapter 5 on the first spectra from the GPI instrument. ADI, combined with the Keck AO system and the NIRC2 camera led to the first published direct image of a planet around another star (Marois et al., 2008).

1.3 Gemini Planet Imager Overview

The Gemini Planet Imager combines all of the lessons from the last two decades in adaptive optics development, coronography, integral field spectroscopy and image analysis to try to achieve two orders of magnitude of improvement in direct imaging contrast. We are now planning a survey of 600 nearby young stars to characterize their outer solar systems. GPI is led by Bruce Macintosh and involves eight institutions collaborating on the design and construction of the instrument (Macintosh et al., 2008, 2012, 2014). GPI was built for the Gemini Observatory, and installed at Gemini South in the Fall of 2013. Due to the high dynamic ranges involved in directly imaging extrasolar planets, GPI is designed to pay special attention to occulting and speckle suppression in order to distinguish planetary companions from PSF speckle noise. GPI was built with the major goal of detecting and characterizing young, Jovian-mass planetary companions by distinguishing them from PSF speckle noise, recording low-resolution spectra of the planets (0.98–2.4 μm), and detecting and then measuring debris disks through polarization (Graham, 2009). GPI consists of seven major sub-components: the adaptive optics (AO) system, the coronagraph masks, the calibration interferometer (CAL), the cryogenic integral field spectrograph (IFS), the opto-mechanical superstructure (OMSS), top level software and a data reduction pipeline. The different sub-systems are shown in figure 1.2.

One of the critical new technologies is a state-of-the-art AO system to compensate for distortion due to the atmosphere. Adaptive optics systems were designed to measure fast atmospheric wave-front errors and correct these errors using a deformable mirror. The GPI AO system is designed to improve on previous facilities by having, in comparison to other AO systems, a large number of degrees of freedom and operating on a short time scale to reduce the residuals caused by atmospheric turbulence (Macintosh et al., 2012). The goal of the AO system, compared to previous facilities, is to lower the total waterfront error from dynamic sources and to lower quasi-static errors by an order of magnitude.

The GPI AO system is composed of a low spatial frequency, high stroke, 11x11 actuator deformable mirror, and a 64x64 Microelectromechanical System (MEMS) low stroke, high frequency, deformable mirror from Boston Micromachines (BMC) (Poyneer et al., 2011), with a 43-actuator-diameter region for high order corrections. Light travels through a spatially-filtered wave-front sensor, to remove high spatial frequency signals that would violate the sampling theorem and be aliased as low-frequency signals. Spatial filtering is implemented as a hard-edged stop in the focal plane before the wavefront sensor (Poyneer & Macintosh, 2003). This allows for attenuation of spatial frequencies up to $1/2d$; reducing scattered light from the dark hole. The GPI AO system uses a 160×160 pixel Lincoln Labs CCD to sample the sky at a typical operation speed of one kilohertz. The use of two deformable mirrors in GPI is due to the fact that the MEMS, while having a high number of actuators, does not have the stroke needed to correct the large, low frequency changes in the atmosphere. The MEMS deformable mirror did not exist as part of the original conceptual design of GPI, but because of the need for a 43-acuator-diameter region, the 4,096 (64×64) actuator MEMS was developed starting in 2004 (Poyneer et al., 2011).

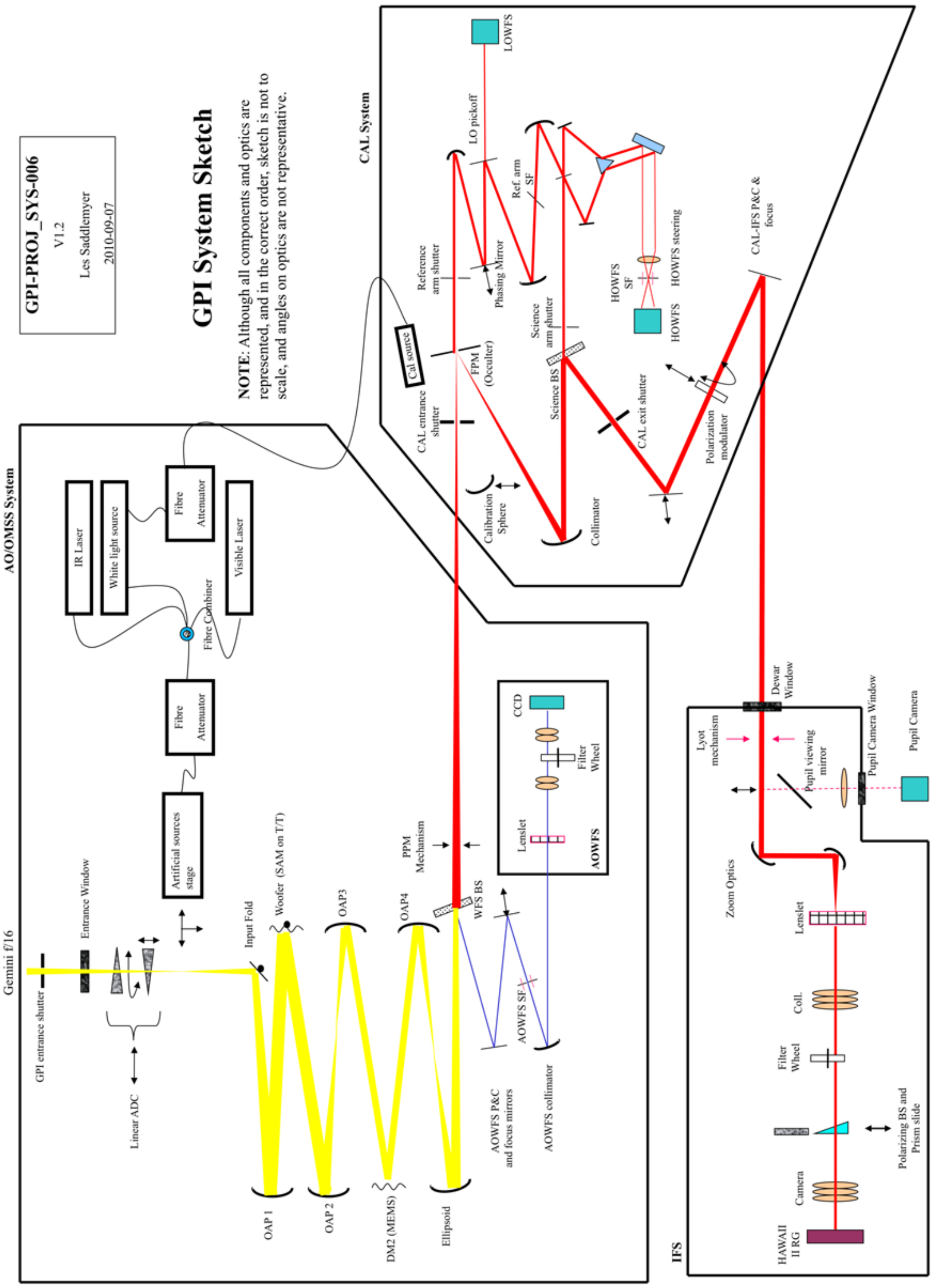

Figure 1.2: A component drawing of the Gemini Planet Imager layout

Unfortunately, a perfectly functioning MEMS could not be obtained (Macintosh et al., 2012). A bad actuator can have enormous effects on contrast. However, the scattered light as a result of this malfunction is well-confined in the Lyot plane (Sivaramakrishnan et al., 2009), allowing customized Lyot masks, installed in the IFS, to block out the scattered light, nearly restoring contrast to its previous level. Additionally, the AO system is innovative in that it includes a spatial filter to prevent aliasing and produces a dark region very close to the star (Poyneer & Macintosh, 2004). The AO system and software was designed and written by Lawrence Livermore National Laboratory (LLNL) (Macintosh et al., 2008). The AO system and its first light performance results are described in Macintosh et al. (2014).

Residual diffraction is removed by an apodized-pupil Lyot coronagraph (APLC) (Soummer et al., 2011; Macintosh et al., 2014). A classical Lyot coronagraph has a hard-edged focal plane occultor, an APLC combines a hard edged Lyot coronagraph with a apodization function introduced in the pupil plane. A grid of narrow, widely-spaced lines printed onto the apodizer forms a two-dimensional grating, producing diffracted images of the central star in a square pattern (Sivaramakrishnan & Oppenheimer, 2006; Marois et al., 2006). These four satellite spots allow for a sampling of the central star spectrum, instrumental, and atmospheric effects in the same image as the object of interest (Wang et al., 2014).

The calibration wavefront sensor (CAL) is designed to deal with non-common path wave front errors (Wallace et al., 2010), providing feedback to the AO system about these wave front errors in the IR. The speckles generated as a result of these errors are not perfectly static as they vary over tens of minutes, nor are they random (averaging out over time). The CAL is unique in that it provides feedback to the AO system about the wave front errors, which are in the science instrument wavelength bands, but are not sensed by the AO system. The CAL is designed to measure the wave front at the focal plane mask, where a thin gold-coated mask with an occultor hole has been etched through the mirror and is used to "block" the central star light. The CAL uses a near-infrared (1.5–1.7 micron) camera to sample these non-common path wavefront errors. The light picked off by the coronagraphic mask is used to feed a low-order Shack-Harman wave-front sensor.

Light from the CAL is fed to the IFS after a pair of pointing and centering mirrors located in the CAL to keep the beam aligned into the cryogenic IFS. The IFS is a $1-2.5\mu$m instrument capable of sampling spectral and spatial information simultaneously. The IFS is discussed in more detail in section 2.

The entire GPI structure is supported by the OMSS constructed by the National Research Council — Herzberg Institute of Astrophysics (NRC-HIA). It is the overarching structure which contains, and holds the major subsystems and electronics for GPI. The OMSS precisely holds the subcomponents of GPI in a predictable alignment and mounts the entire system to one of the five Gemini instrument ports (figure 1.3).

1.4 Outline of Thesis

This thesis is centered on the direct detection and observation of extrasolar planets using the facility class Gemini Planet Imager. The first component of this thesis was the construction and testing of the integral field spectrograph for GPI (Chapter: 3). This included the construction of the actual instrument itself, trouble shooting and resolving unforeseen challenges in the construction and operation of the IFS, and the verification that the instrument performance met the stringent requirements for a the camera for the Gemini Planet Imager. This work continued with the testing and verification of the instrument performance at the University of California, Santa Cruz where the instrument was integrated with the other components of GPI, and concluded with the integration and commissioning

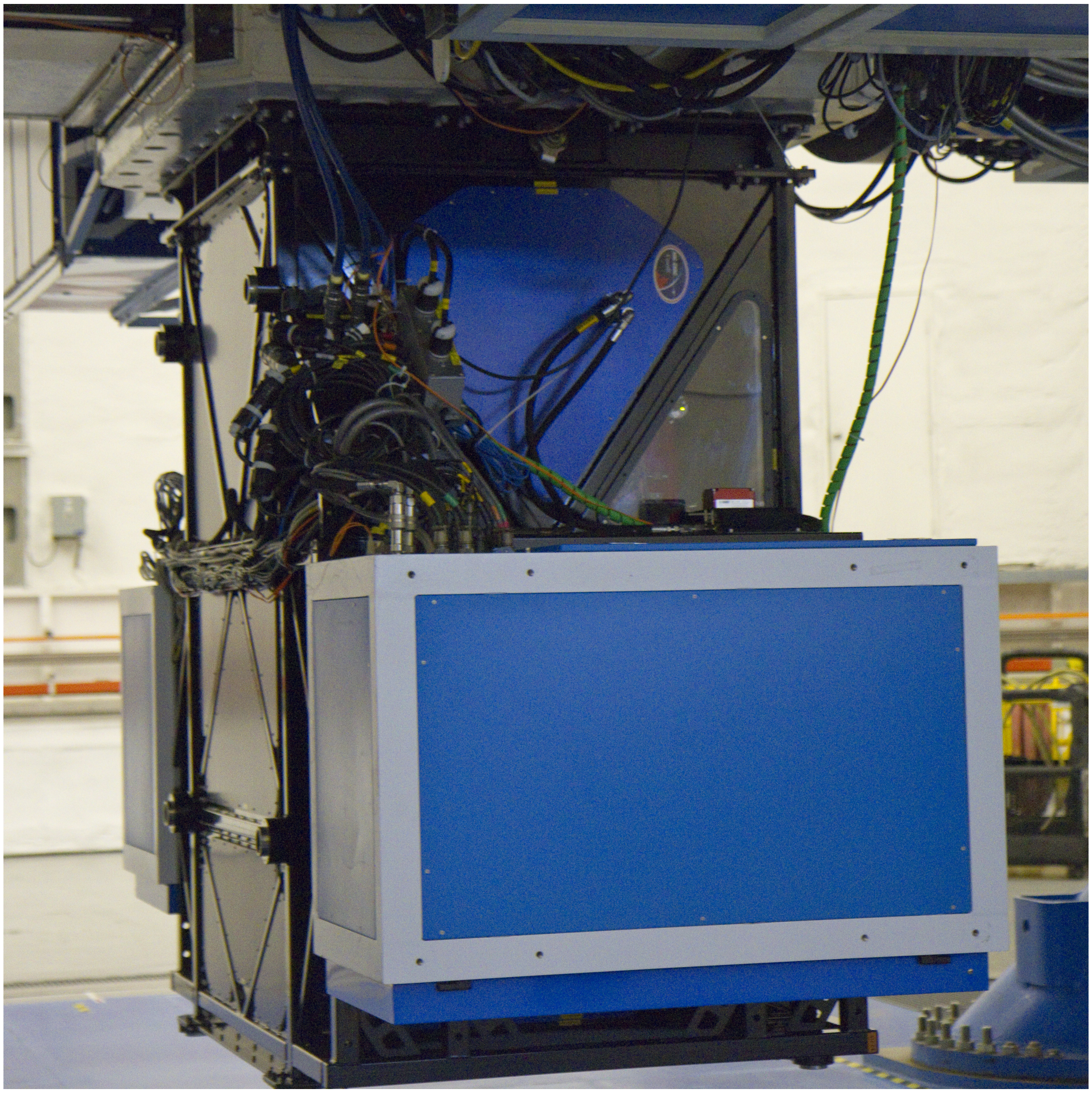

Figure 1.3: GPI mounted to the bottom port of Gemini South.

at Gemini South, located on Cerro Pachón, Chile.

Subsequently, in line with the goals of GPI, studies were performed on β Pictoris b — a Jupiter sized extrasolar planet — bright enough to be directly detected using current AO systems. Many questions related to extrasolar planetary formation and many of the future goals related to directly observing extrasolar planets will be answered only based upon the results from a large number of observations. A large survey will begin in the Fall of 2014, but is outside of the scope of the research contained in this thesis. The study of the singular object β Pictoris b serves as one foundational building block towards answering these complex questions. Before GPI was installed, I performed a multi-epoch broadband imaging and position monitoring campaign of β Pictoris b with the NIRC2 instrument at the Keck Observatory. This work constrained the orbit of the planet and helped prepare for the GPI observations. As part of GPI's early science effort, we obtained the first H-band spectrum of β Pic b (Chapter 5).

CHAPTER 2

Gemini Planet Imager Integral Field Spectrograph

2.1 Introduction

In this chapter, we will focus on components and systems I was intricately involved with especially those I tested and will describe in chapter 3. The science instrument designed for GPI is an integral field spectrograph (IFS). The GPI IFS is a cryogenically cooled infrared science instrument designed for GPI and capable of gathering spatial and spectral information simultaneously (Figures 2.1,2.2,2.5). For an IFS, the spatial field is sampled with an image slicer, a bundle of fibers, or in the case of GPI with a lenslet array. With these methods the spatial field is sampled and then broken up into its spectral information. The GPI IFS principle investigator is James Larkin and the instrument was constructed at the University of California, Los Angeles (UCLA). The GPI IFS design is similar to the OSIRIS instrument (Larkin et al., 2006) currently employed at the Keck observatory. All of the lenslet based spectrographs rely on the ground breaking designs from Roland Bacon such as the optical Tiger Instrument (Bacon et al., 1995).

The GPI IFS is a cryogenic instrument cooled with a mechanical closed cycle refrigerators (CCRs) and sensitive from $\sim 1-2.5\mu$m. A collimated beam produced by the CAL unit (Wallace et al., 2010) enters the spectrograph through an infrared transmissive window that serves as a vacuum seal (Section 2.2). The light then passes through a wheel with 10 positions located in the pupil plane

(Section 2.3). For alignment purposes, a fold mirror can be inserted after the pupil plane to intercept the incoming beam and redirect the light though a small optic, through another infrared transmissive window and onto a small commercial infrared camera (Section 2.3). While in science operation, the fold mirror is not inserted into the beam and a pair of highly polished spherical mirrors are used to reimage the focal plane at F/200 onto the lenslet array (Section 2.5).

The lenslet array is the heart of the IFS and samples the focal plane to produce a grid of "spots" which are each an image of the telescope pupil. The choice of an all reflective design for the reimging optics was made to minimize chromatic aberrations that can degrade speckle suppression, which is completely dependent on modeling of chromatic shifts in the speckles. The only aberrations affecting the image quality of the field are from elements in front of the lenslet array. After the lenslet array all of the spectrograph optics are refractive with a collimator and camera system based on Petzval lens systems and is detailed in an earlier SPIE paper by Thibault et al. (2010). The filters and prisms lie between the collimator and camera in the spectrograph system (Section 2.7). The filter wheel contains 5 filters covering the 1–2.5 micron near-IR regime. The physical location of the filter wheel is located in spectrograph portion of the optics, down stream of the lenslet to remove the filters effects on image quality. The detector finally sits in the spectrograph focus conjugate to the pupil plane from the lenslet array. For the polarization mode, the primary prism is removed and a Wollaston prism is inserted into the collimated space to separate the two polarization states.

Table 2.1: IFS Performance Characteristics

Filters	*Y*, *J*, *H*, *K1*, *K2*
Spatial Sampling	0.01414”/lenslet
FOV	$\sim$ 2.7” $\times$ 2.7” (198$\times$199 lenslets)
Spectrograph flexure	$<$ 1 detector pixel from 0 to 90 degrees
Lenslet Array	110 μm pitch in F/200 focus
Full Mechanism Reconfiguration	$\leq$30 seconds
Optical Throughput	$>$ 62%
Spaxel Crosstalk	$<$ 5.1%
Dark Current	Median 0.02 e-/second

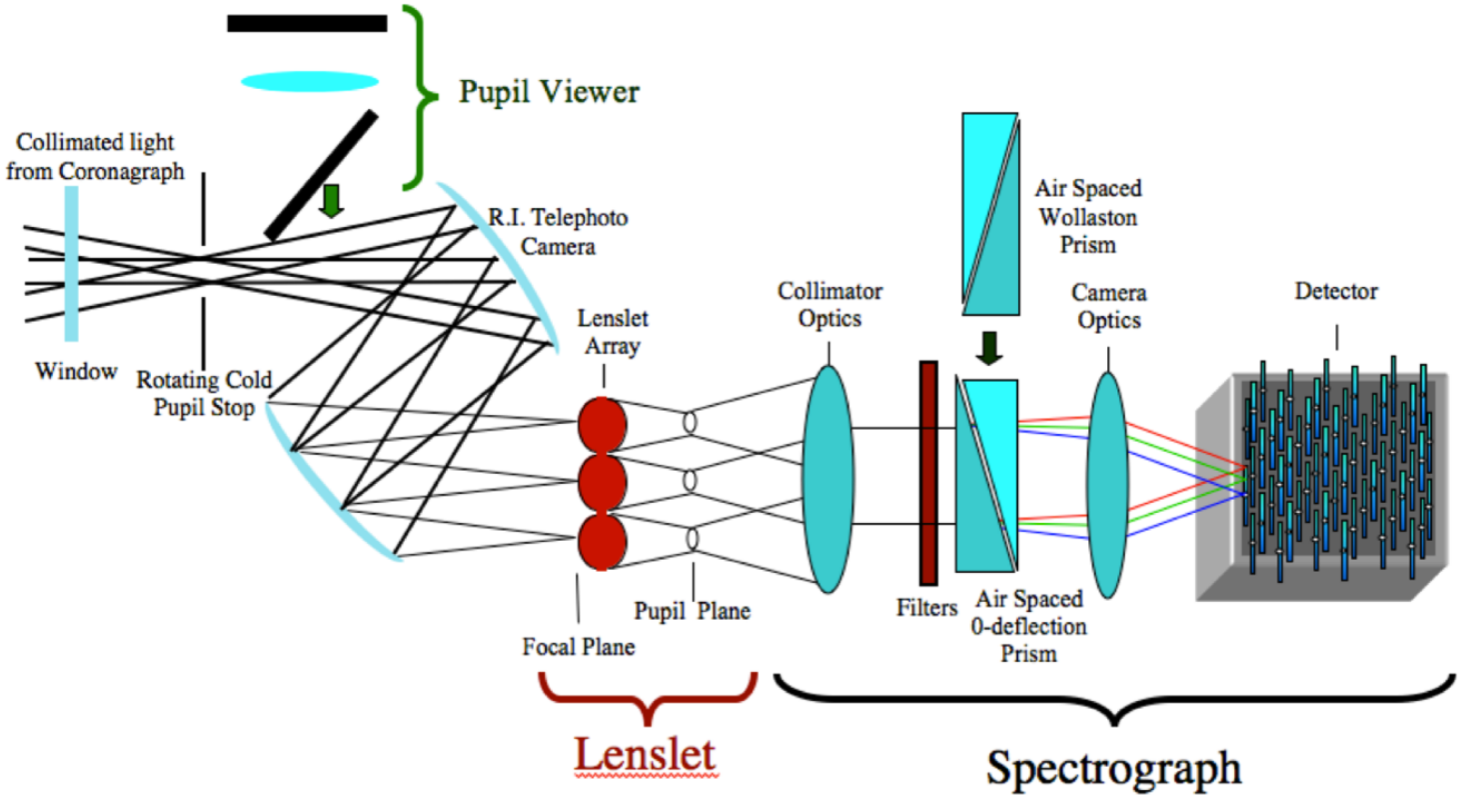

Figure 2.1: A cartoon drawing of the optical components in the GPI IFS.

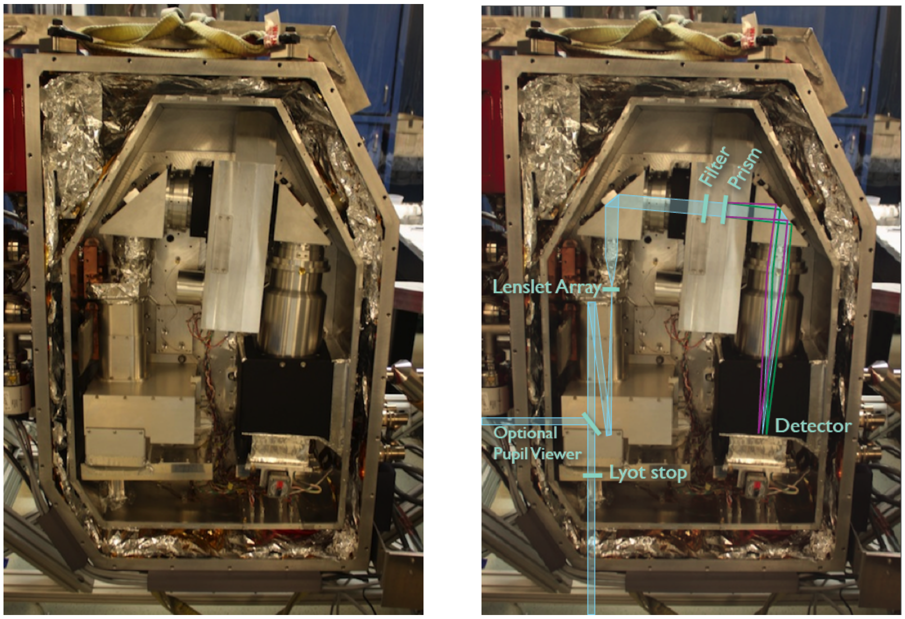

Figure 2.2: **Left:** The integral field spectrograph (IFS) is shown from the top with the vacuum cover and cold shield removed. The light baffles inside the cold shield are still in place. **Right:** The same image overlaid with the optical path through the system. The optional pupil view is used by inserting a mirror into the optical path. This mirror determines if light goes to the pupil viewer or the lenset array. It is not possible to send light to the pupil viewer and the lenslet array simultaneously.

The final result sampled by a Hawaii-2RG (Section 2.8) is that the IFS has a field of view of 198 × 199 spatial locations and can measure either eighteen simultaneous spectral channels[1] The lenslet spatial scale, 14.14 ± 0.01 milliarcseconds per lenslet (Konopacky et al., 2014), was chosen to Nyquist sample the PSF at the shortest wavelength. Given the IFS plate scale, this leads to a greater than 2.7×2.7 arcsecond field of view; approximately the size of the dark hole created by the AO system at the longest wavelength of operation. By sampling both spectral and spatial information simultaneously, artifacts within the PSF, such as residual speckles, can be suppressed due to the location — wavelength dependence of interference artifacts compared to planets. Thus for a given observation, the location of the planet is invariant compared to the central

---

[1] In H-band. Other wavelengths have slightly different spectral dispersion (see Table 2.2).

Table 2.2: IFS Filters

Filter Name	Short 1/2 Power (μm)	Long 1/2 Power (μm)	Central Wavelength (μm)	Spectral Resolution ($R = \lambda/\delta\lambda$)
Y	0.95	1.14	1.045	~ 43
J	1.12	1.35	1.232	~ 48
H	1.5	1.8	1.647	~ 52
K1	1.9	2.19	2.045	~ 65
K2	2.13	2.4	2.255	~ 90

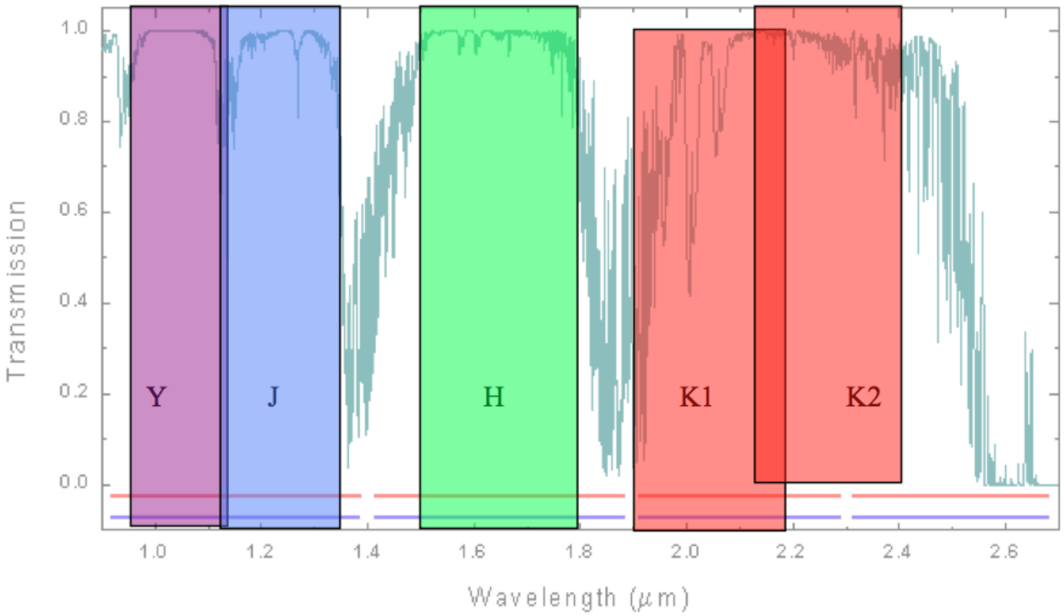

Figure 2.3: *Y*, *J*, *H*, *K1*, *K2* filters shown overlaid on an atmospheric transmission curve with approximately 1.6 mm of precipitable water vapour.

star location, but because speckles are interference artifacts their spatial location is wavelength dependent. Additionally, the initial detection of a candidate planet will include spectral information to distinguish it from background objects.

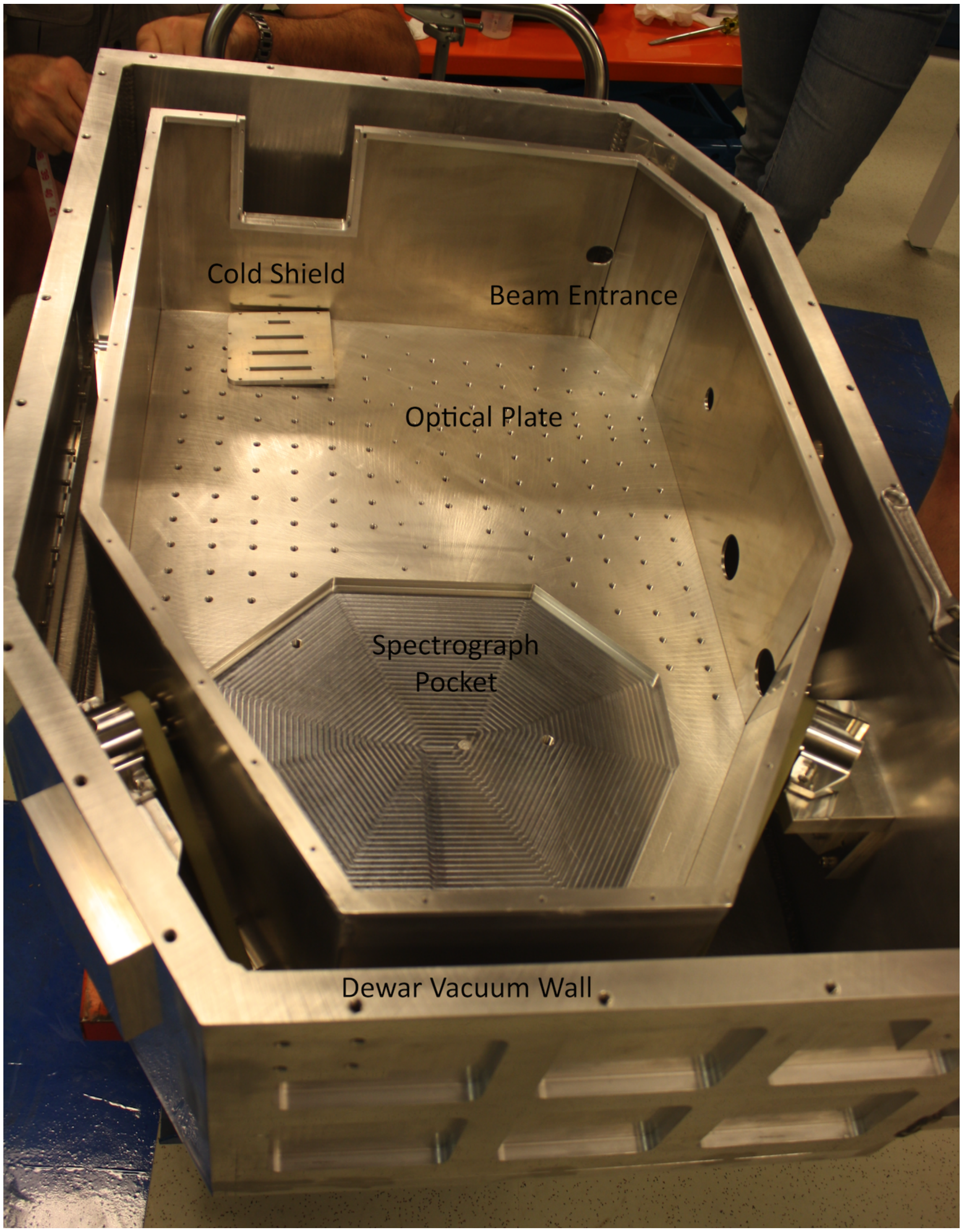

Figure 2.4: The major structural components of the IFS.

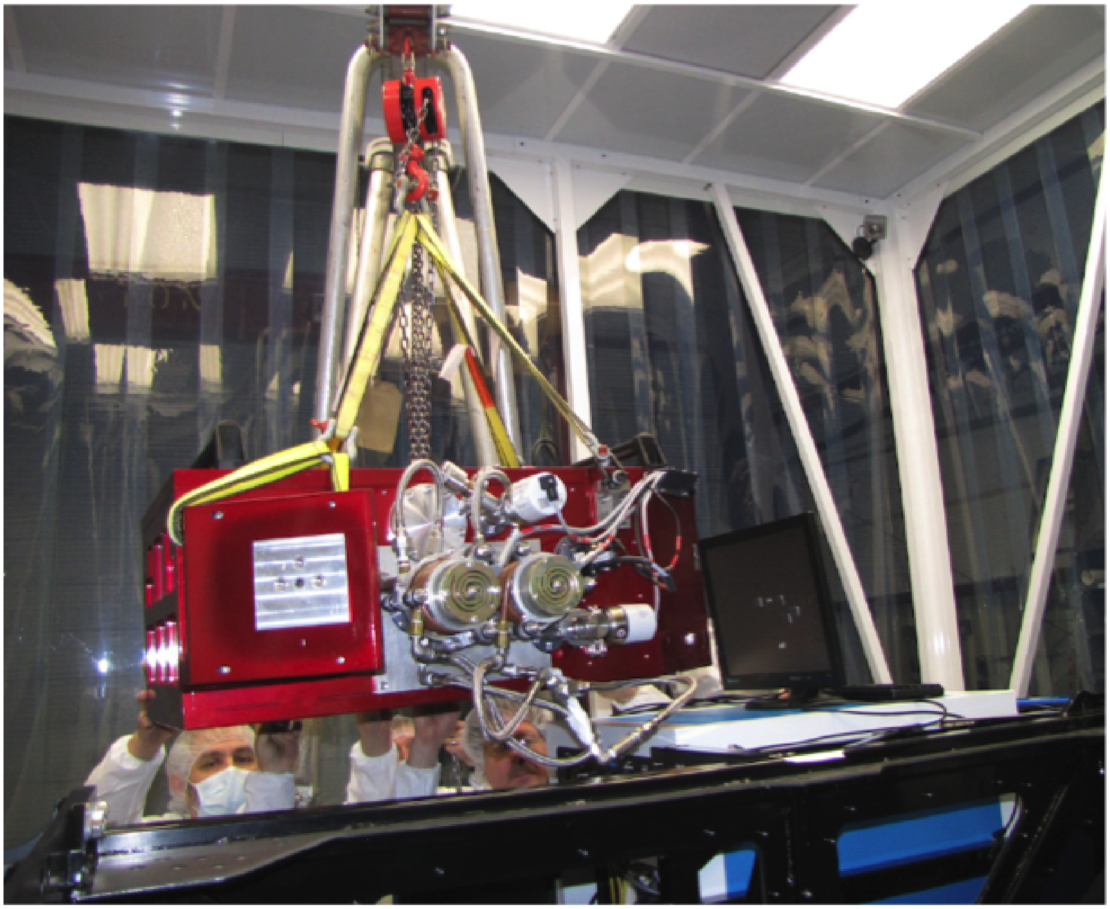

Figure 2.5: Installation of the UCLA-built IFS into GPI at UCSC

2.2 Vacuum Enclosure & Overall structure

The IFS vacuum enclosure is made of 25mm thick aluminum walls which have been welded together to form a 6-sided box with a separate lid. At strategic points the IFS walls have been light-weighted in order to reduce the overall dewar weight, but not to significantly effect the strength. All of the seals are made with Buna-N O-rings. The outside of the vacuum enclosure has three precision machined pads, referenced to tooling balls locations inside the dewar to allow for precise mounting of the IFS to the OMSS (Section 1.3). Two windows are located in the dewar to allow light to pass between the inside vacuum and outside environment. These windows are an infrared grade of fused silica (Infrasil) and are the only transmissive elements before the lenslet array samples the field of view. Infrared grade fused silica has a much lower water content leading to excellent infrared transmission. Five vacuum pass-through connections are made to allow for electrical cables to pass signals between the atmospheric IFS electronics and the internal electronics mechanisms, switches, sensors, heater, and detector. Mounted on the outside of the dewar are 5 additional vacuum ports, two for the Sunpower inc. CCRs (Section 2.9), two for the two vacuum gauges & over-pressurization prevention valves, and a fifth port which was installed in case a replacement CCR was needed. The fifth port was created as part of a backup strategy and implemented by cutting an additional port in the dewar wall so that a Pulse Tube cooler or other future CCR system could be mounted there if needed. This port was cut and sealed with great care while all optics and electronics were already inside the dewar. The IFS dewar is powder coated to protect the aluminum walls, but all vacuum seals have been left as bare aluminum.

The internal components of the IFS are mounted on a cold optical plate, which is cooled via the CCR (Section 2.9). The optical plate is connected to the CCR via flexible copper straps (Section 3.10). The optical bench contains all the optics of the IFS and is structurally connected to the outside dewar wall by three A-frames made of fiberglass Micarta (known as Garolite or G-10). Bolted to the optical bench is an aluminum cold shield to mask the internal components operation in the IR from the $\sim$ 300K glowing vacuum enclosure walls. The IFS is surrounded by several layers of aluminized Mylar and gold Kapton to reduce the radiation load on the cold shield walls from the external vacuum walls. Additionally, the three mounting brackets for the G-10 A-frames located on the vacuum enclosure wall are gold coated. A nickel coating was applied by an outside vender, then the mounting brackets were gold plated by the UCLA Infrared Lab.

2.3 Lyot Stop & Pupil Camera

Within GPI, an occulting spot in a focal plane masks off much of the light from the star. Much of the remaining light is diffracted into a ring corresponding to the outer edge of the primary mirror. To remove this ring of light, block thermal emission from the telescope and diffraction from the spiders, we have selectable Lyot stops located in a pupil plane. Once light has passed through the entrance window and through a hole in the cold shield, it passes though the Lyot stop selector wheel. The IFS uses 10 different positions in a rotating wheel located in the pupil plane. This wheel contains a total of 9 cold Lyot stops and one blank. The GPI Lyot stops are unique in that they contain tabs to block off bad actuators located in the AO system. This blank plate is the only light blocking point in the IFS science optical path.

The precision of the Lyot positions is maintained by individual detents — a notch in the cryogenic wheel used to locate and hold each position — and switches are used to confirm the positions. The switches are placed in such a way that each individual position generates a unique switch pattern, but does not require the same number of switches as positions. For alignment and calibration the pupil can be imaged by inserting a fold mirror into the light path so the beam is redirected through a H-band filter and into an off-the-shelf, external, indium gallium arsenide (InGaAs) camera from Sensors Unlimited, Inc. The InGaAs camera is located external to the IFS dewar operating at atmospheric pressure. The IR sensitive camera has a cut-off wavelength of 1.7 microns, and we use an H-band filter to limit its bandpass to $1.5 - 1.7$ microns. The camera utilizes an industry standard Camera Link interface to a model PCIe DV C-Link frame grabber from Engineering Design Team Inc. (EDT).

2.4 Reimaging system

The re-imaging system is used to focus the input collimated beam into an image on the lenslet array. The incoming beam has an F/200 focal ratio resulting in the need for a 2 meter focal length. In order to fit this length into the small space constraints of the dewar, a pair of spherical mirrors is used to relay the beam across the optical bench. To reduce chromatic aberration, a reflective design was selected using two super polished gold coated spherical mirrors acting as a telephoto system. To minimize wavefront error due to differential contraction the mirror substrates are made of the ultra-low expansion material Zerodur. The entire optical path is covered by light tight tongue and groove baffle system, with all interior surfaces painted with the IR absorbing material Aeroglaze® Z306. The resulting focal plane falls on the lenslet array (Section 2.5).

2.5 Lenslet Array

The lenslet array is the heart of the optical system and serves as the location where the field of view is sampled. The lenslet array consists of an array of micro-lenses, having a pitch of 110 μm. The lenslet was produced by MEMs optical with a grayscale lithographic technique that produces a monolithic optic with no internal surfaces. The lenslet array acts at the boundary between the spectrograph and the re-imaging optics by sampling the focal array, and generating a grid of micro-pupil images in a plane. The lenslet array is rotated by ~ 24.8 degrees with respect to the incoming field orientation allowing the interlacing of the micro-spectra. Given the diffraction limited sampling of the lenslets, the size of the pupils is dominated by diffraction effects and geometric aberrations are negligible for the very slow input beam.

2.6 Spectrograph Optics

The spectrograph optics (Figure 2.6) were designed, built, and installed onto the UCLA sub-plate by the Université de Montréal and Immervision (Thibault et al., 2010). The spectrograph optics are made up of 8 lenses include three of Cleartran (ZnS), four of BaF2 and one of S-FTM16, making an all-refractive design except for two fold mirrors, which are used to package the optics in the IFS space envelope. The optics between the lenslet array and the detector form a standard spectrograph with a collimating set of lenses, a dispersive prism (Section 2.7) and a camera set of lenses. The spectrograph collimator has a focal ratio of F/3.52 (to the corner of the square beam from the lenslet elements) with a 22.44 mm square field. The spectrograph camera has a focal ratio of F/5.89 and remaps the micro-pupil array onto the science detector. Additionally, located with the prisms between the spectrograph optics and the camera lenses is a five position filter wheel (Table 2.2).

2.7 Prisms

While the spectrograph optics are provided by the Université de Montréal and Immervision, the filters and dispersing elements were installed by UCLA. In order to select a spectral mode or polarization mode, a spectral prism and the Wollaston prism were designed to have no net deflection on light at 1.65 microns and to be inserted into the middle of the spectrography optics (Figures 2.1,2.7). The spectral prism uses a pair of prism elements to produce the required R=45 primary spectrum but with no net deflection at the central wavelength of 1.65 μm. The spectral prism pair was designed consisting of BaF2 and S-FTM16. Polarization observations are made by removing the primary prism and inserting a Wollaston prism made of MgF2. Because of the necessity that it operate at cryogenic temperatures, an “air-spaced” Wollaston prism is used to avoid thermal stresses between the two prism elements.

2.8 IFS Detector

The GPI IFS uses a 1–2.5 μm 2048×2048 Mercury-Cadmium-Telluride (HgCdTe) H2RG (HgCdTe Astronomical Wide Area Infrared Imager, where R denotes reference pixels, and G denotes guide window capability) with a SIDECAR (System for Image Digitization, Enhancement, Control and Retrieval) ASIC (Application Specific Integrated Circuit). The detector is a hybrid CMOS imaging sensor, combining infrared sensitive materials with CMOS integrated circuits. The GPI IFS detector was built by Teledyne and is an October 2008 generation device. The GPI detector is capable of 1, 4, or 32 readout channels[2]. The border of the 2048×2048 array is made up of a 4 pixel wide band of non-photosensitive pixels, which are read out as “reference” pixels. These reference pixels at the top and bottom of the columns are used to track any bias voltage fluctuations that occur in each of the individual readout channels. While GPI reads the side reference channels, they are measured too sparsely to improve the data quality and are thus ignored for any noise tracking in the IFS readout. The CMOS design allows for non-destructive readouts of the pixel amplifiers, allowing for multiple reads of the array. The detector is operated in a continuous readout or reset mode, such that the entire array is clocked over every 1.45479s (including overheads), at a 100 kHz pixel clock rate.

The SIDECAR ASIC operating in a cryogenic environment, is connected to a JADE2 (JWST ASIC Drive Electronics) with a single continuous, uninterrupted connection cable. This cable, is passed through the vacuum wall and potted in Emerson-Cumming Stycast 2850-FT, using a custom built in-house holder, adopted from an initial design by the University of Hawaii. The JADE2 is used to

---

[2] For science operations the GPI detector is operated solely in 32 readout mode.

connect the detector subsystem to the GPI Windows XP computer ("IFS Brick").

2.9 Sunpower Closed Cycle Refrigerators

The IFS uses two CryoTel GT closed cycle refrigerators (CCR) from Sunpower Inc., each rated at 15W of cooling power at 77K[3]. The decision was made to use these Stirling cycle based cryo coolers instead of Gifford McMahan closed cycle refrigerators, to avoid the substantial broad-band vibration generated by Gifford McMahan CCRs. Several Cryocoolers were considered, but due to their low vibration levels and availability Sunpower CryoTel GT cryocoolers were selected to cool the GPI IFS optical bench (Figure 3.8). These Cryocoolers operate at a 60 Hz frequency, only producing vibration and electrical interference at 60 Hz and its harmonics. On the back of each CCR is a vibration absorber tuned precisely to 60 hertz and intended to absorb and dissipate some of the vibrational energy generated by the CCR and to prevent this energy from being translated into the IFS.

2.10 Mechanisms

The GPI IFS contains five cryogenic mechanisms based upon previous mechanisms from the UCLA Infrared Laboratory. There are four active mechanisms used in the standard operation of the spectrograph and one mechanism which has been disabled, but was part of the initial alignment of the detector. The mechanisms are based upon a long history of tried-and-true mechanisms in other IR instruments built by the UCLA Infrared Laboratory: OSIRIS, MOSFIRE, NIRSPEC and GEMINI. All mechanisms use off-the-shelf components and air cooled motors which have been modified by the UCLA Infrared Laboratory to operate in a

---

[3] With a reject temperature of 35C.

cryogenic environment. Similar mechanisms with similar modifications have been in use in other IR lab instruments, with some motors demonstrating a lifespan of over a decade. Motion control is provided by a Galil DMC-2183 controller, which was chosen as a standard for all mechanism controls within GPI resulting in simpler development, reduced cost, and the ability to carry spares available to the entire instrument. All the IFS mechanisms operate cold, with zero holding current when they are not in motion. The GPI software provides movement limits on the motors in a given period of time to prevent over heating of the windings in each motor. Motor limits are high enough as to not interfere with standard observing sequences, but without risk of thermal damage to the motor windings. The two slides (Pupil Camera & Prism Slide) use hard stops to control their position, while the two wheels (Lyot wheel & Filter wheel) use roller detents to hold their position after the motor is de-energized. Due to the extended cycle time needed to warmup, pump, and cool-down the instrument, prototype mechanisms using cryogenically prepared parts were tested to avoid breakdowns once they were installed in GPI. One wheel and one slide mechanism prototype were operated through thousands of moves to simulate an expected instrument lifetime of movement. These components were then inspected for signs of wear. Despite these early tests, minor modifications were made during the integration and testing phases and a problem with incorrect compression of drive train elements in the two slides was not remediated fully until January 2014 after the first light observations.

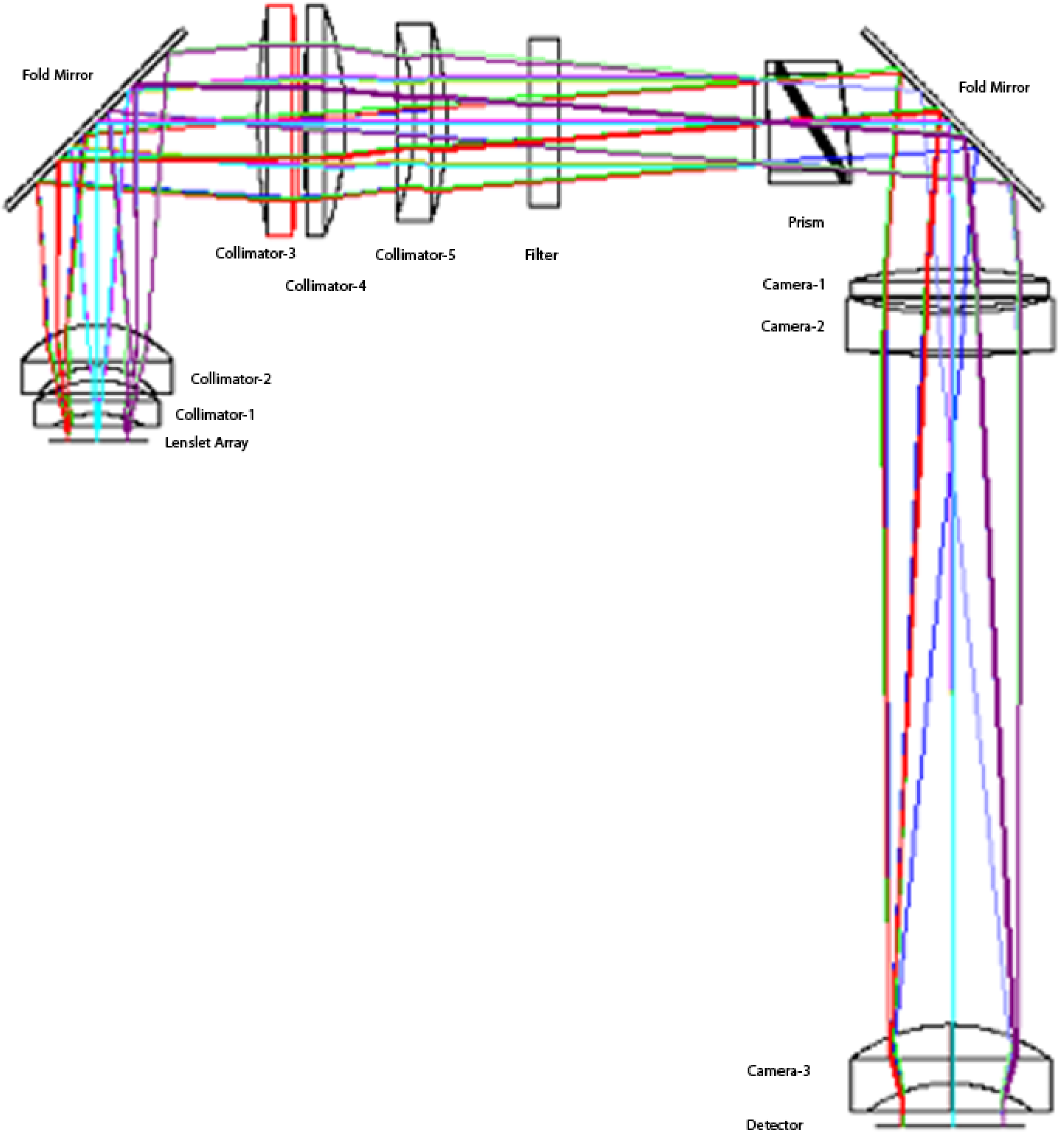

Figure 2.6: Zemax representation of the Université de Montréal and Immervision optics (Thibault et al., 2010).

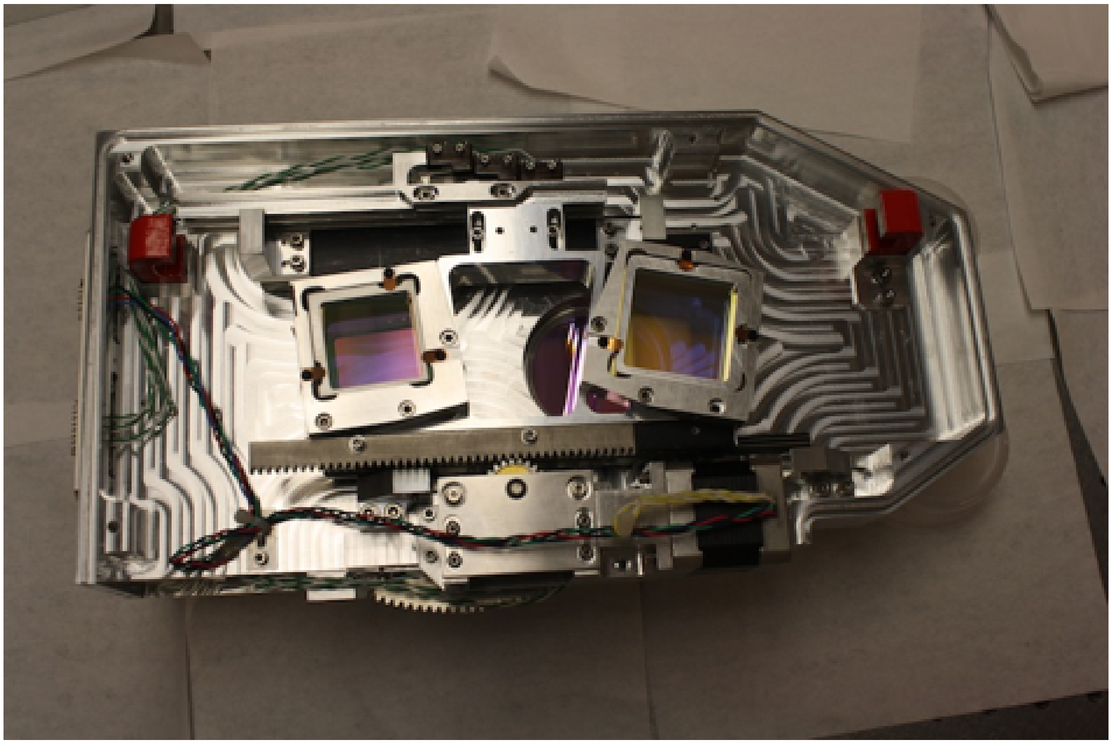

Figure 2.7: The IFS Prism Slide. The prism on the right is the Wollaston prism, while the prism on the left is the spectral prism.

CHAPTER 3

Integral Field Spectrograph Testing and Performance

3.1 Introduction

The GPI IFS (Chapter 2) underwent performance testing at UCLA prior to shipment in December 2011 to the University of California, Santa Cruz (UCSC), where it was integrated into GPI. Additional performance testing was completed at UCSC once the IFS was fully integrated into the entire system. Understanding the performance of the instrument is critical to verifying that the IFS meets the needs of GPI, and to provide feedback to the general astronomical community as to the performance of the instrument. We present the performance of several key subsystems and the investigation and solution of several interesting technical challenges encountered during the construction and integration of the instrument.

3.2 Lyot Stop and Pupil Camera

Nine Lyot masks and a blank are mounted in a wheel mechanism located at the pupil plane. Due to the need to mask small features like individual bad actuators in the deformable mirror and the secondary support spiders the masks need to be aligned to each other and repeatedly moved into the beam. The masks were installed to a tolerance of ±0.5 degrees by aligning the masks to a precision of ±0.109 mm using two vertical alignment marks on the edge of the masks (Figure 3.1). To measure repeatability, the Lyot wheel was moved to different positions and then returned to its initial position. This was movement was performed multiple times without resetting and homing the location of the wheel. Images of the Lyot masks were taken with the pupil camera (Figures 3.3,3.4) after each set of moves and the resulting images were then cross-correlated to measure mechanism repeatability. This testing indicated that the Lyot stop movement is highly repeatable to within 0.1% of the beam diameter. Because GPI cannot be rotated while observing, the orientation of the Lyot masks to each other is critical. Further, because misalignment of the Lyot mask to the central spiders can cause significant diffraction effects in the imaging plane, a high level of repeatability of the Lyot mechanism is required to reduce the need to realign GPI between observation configuration changes. An alignment to a tolerance of ±0.5 degrees between Lyot masks and is an acceptable level. As this amount of rotation is about 0.2 actuators at the edge of the pupil and within the overall system goal of having an alignment tolerance of half an actuator, including terms for flexure.

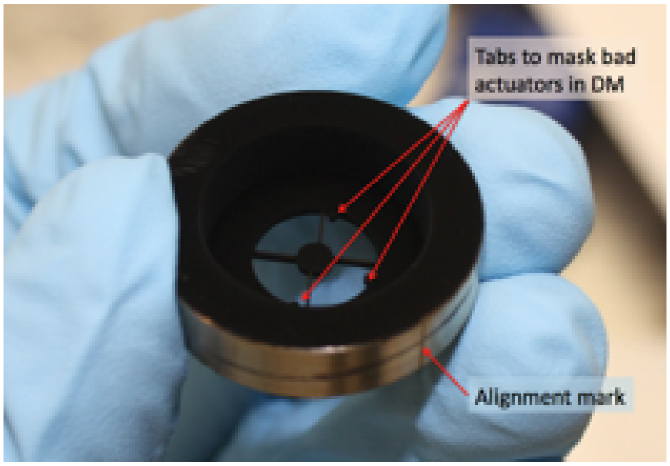

Figure 3.1: This is an image of one of the Lyot Masks. In addition to masking off the secondary, outer edge of the primary and the secondary support spiders, three tabs are used to mask bad actuators in the MEMS mirror. An external alignment mark was used to coalign the 9 transmissive masks.

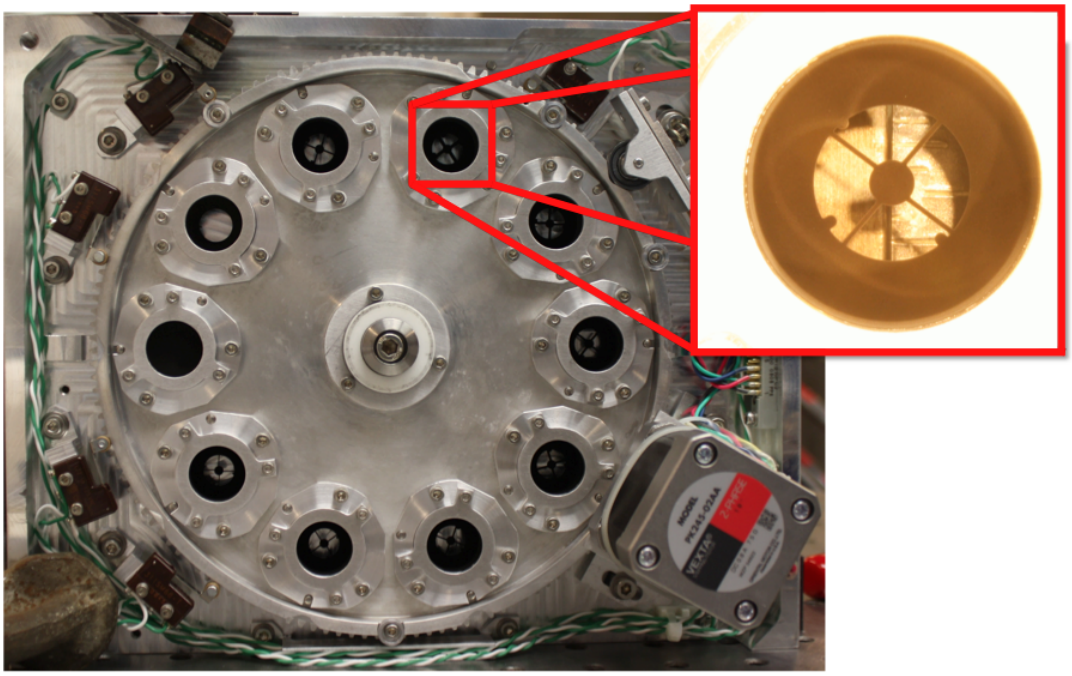

Figure 3.2: An image of the IFS Lyot wheel. This set of Lyot stops was replaced during integration and testing at the University of California, Santa Cruz by the UCLA IR Lab following the failure of one of an additional AO MEMS actuators which occurred after the shipment of the IFS. Each small tab shown in the Lyot stop is intended to block out the stray light generated by bad MEMS actuators. This expanded image of the Lyot stop was taken with an external camera to verify alignment of the Lyot stop before installation in the IFS.

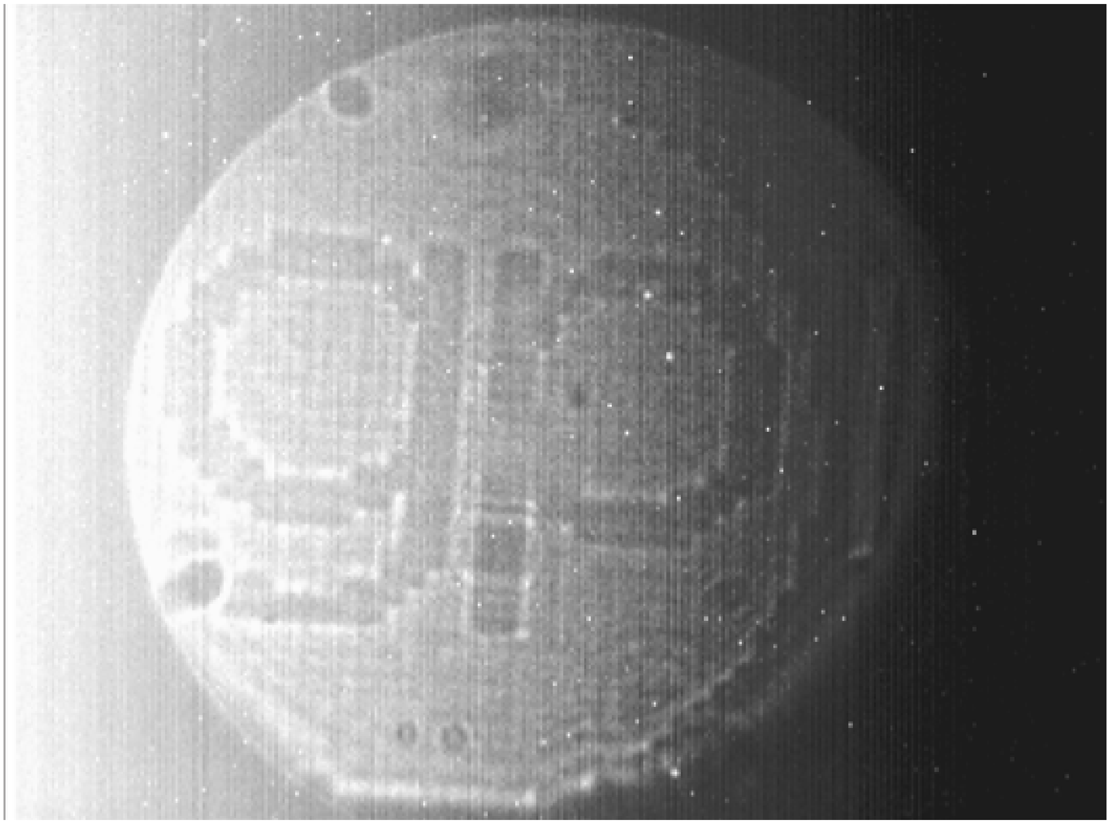

Figure 3.3: First light image of the IFS pupil camera, after install into GPI, with the instrument still warm (Figure: 2.5). An image of the GPI logo generated by deforming the MEMS to cause constructive and destructive interference in the pupil plane allowing the GPI logo to be generated by the AO system and imaged by the IFS pupil camera.

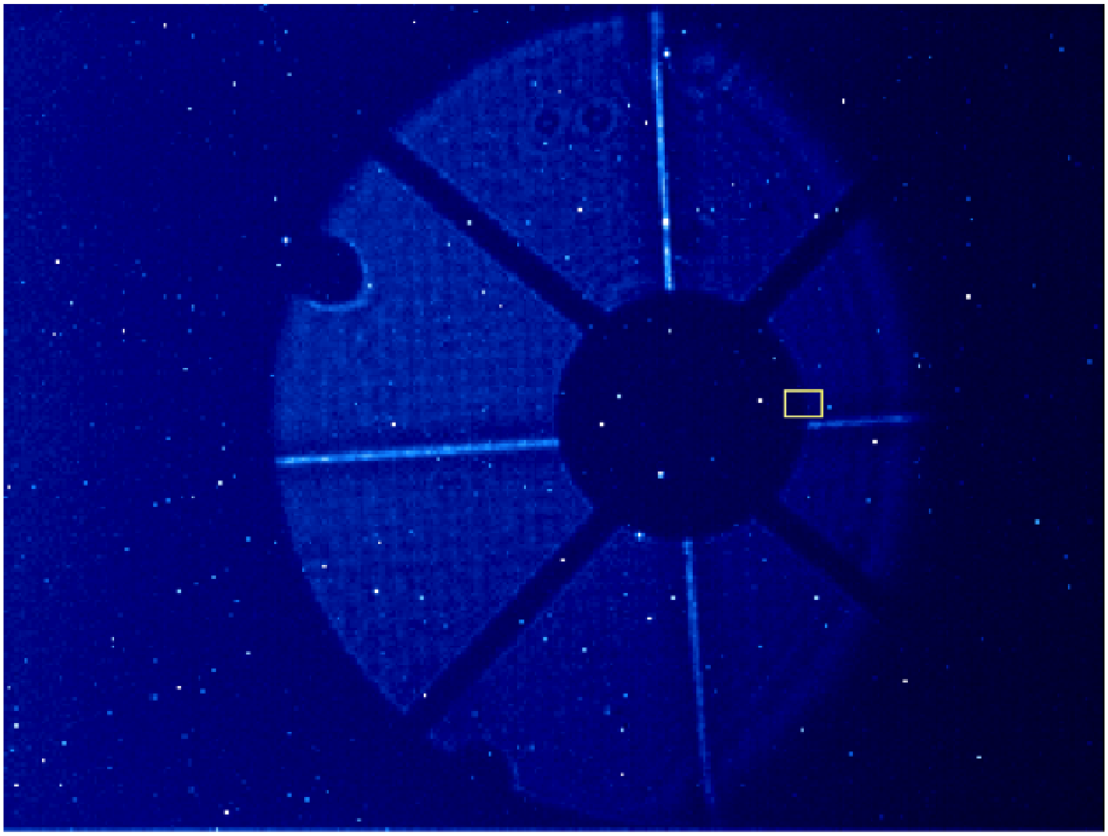

Figure 3.4: An image from the IFS pupil camera with a lyot stop moved into the beam. The lines are displayed by pistoning the MEMS in the AO system to measure the rotation between the AO system and the IFS.

3.3 Reimaging Optics

The reimaging optics within the IFS consist of a pair of spherical mirrors used as a telephoto system to relay the image onto the lenslet array (Section 2.4). The system must be aligned warm in such a way that it will be in focus and aligned at cryogenic operating temperatures. In order to accomplish this alignment, a combined warm and cold model was calculated using CAD software in order to predict the correct warm positions of optical elements and mounts that would allow them to maintain focus and alignment during cryogenic operations. A coordinate measuring machine was then used to make precision measurements and compared to the model. This was done by touching the outside reference surfaces of the IFS (Section 2.2) and then touching the optical and back surface of the individual relay mirrors to initially align them. In the final configuration, typical residuals to the warm model were on the order of 50μm. A beam passed into the IFS at UCLA through a precision 10×10 pinhole grid at 1 μm has pinhole images under two lenslets in FWHM and overlapping Airy rings (Figure 3.5). This shows an excellent optical alignment and quality can be achieved in projection of an image onto the focal plane at the lenslet array (Section 2.5). A final optics alignment was performed after cold tests at UCSC and when the IFS had been integrated with the rest of GPI.

3.4 Alignment & Characterization of the Spectrograph Optics

The spectrograph optics are needed to relay the lenslet pupil to the detector. Therefore it is critical that the spectrograph optics are aligned to the detector. The optics in the spectrograph were assembled, aligned and cryogenically tested using an engineering grade H2RG at the University of Montreal prior to delivery

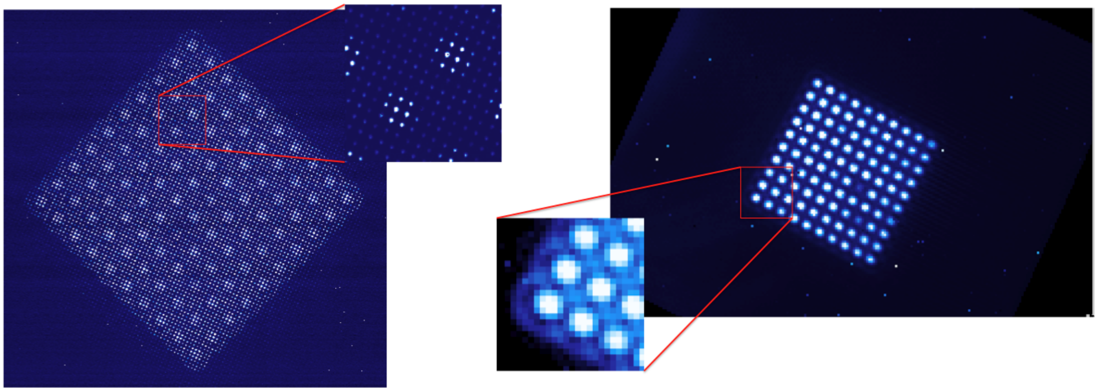

Figure 3.5: The image quality of the IFS reimaging optics. **Left:** This is a raw frame in the undispersed mode in which a 10 × 10 grid of precision pinholes are illuminated by a whitelight source. Upon closer inspection, the small size of the micro-pupil, less than 2 pixels fwhm, indicates the alignment and high quality of the spectrograph optics. **Right:** Putting the IFS into spectral mode for the same 10 × 10 pinhole grid, the data was then processed by the GPI data pipeline. In both images, overlapping Airy rings can be seen from the focused pinholes, indicating the high quality of the reimaging optics.

to UCLA (Thibault et al., 2010). The final step in the alignment process was to focus the spectrograph optics on the H2RG (Section 2.8) using a cryogenic focus mechanism. We used this cryogenic focus mechanism so that we would not need to cyro-cycle the entire instrument. If this mechanism did not exist, focus could only be achieved through multiple cryogenic cycles of the instrument, with the detector mounting stage moved between subsequent cool downs.

To assist in this focusing process, it is possible to remove all prisms (direct mode), which results in an image of the micro-pupils. These 40,000 micro-pupil were focused onto the detector array using a cryogenic focus stage with a range $\sim 390\mu m$. Since this focus is only used for the spectrograph optics, and is only internal to the IFS, it was disabled after a final focus was reached. Measurements of the pupil spots gives a FWHM < 2 pixels across the array. Spectral resolution is limited to the ability to Nyquist sample the spectra, allowing no spectral improvement in resolution for a spot FWHM < 2 pixels.

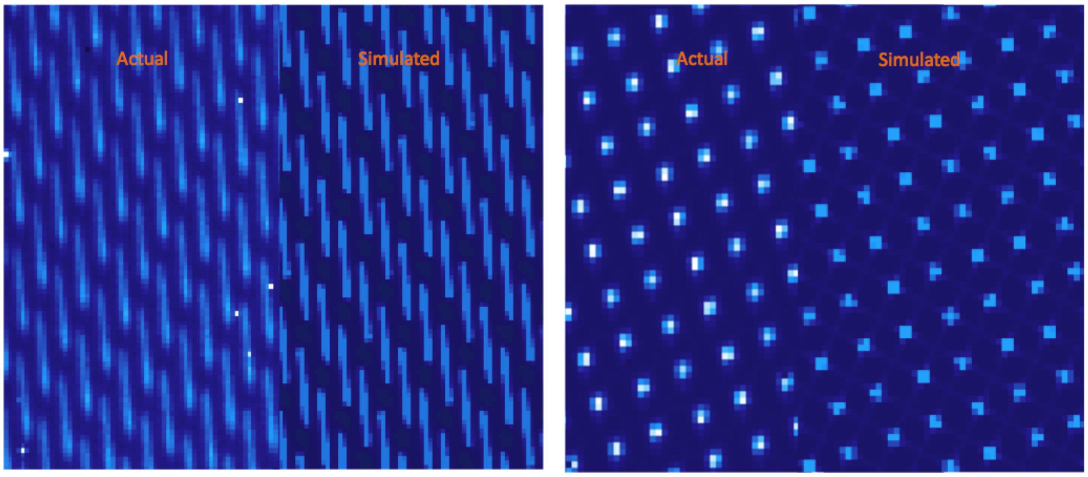

Figure 3.6: Images of the spectrograph portion of the instrument show good agreement with the predicted Zemax model. **Left:** An actual spectral image taken with the IFS versus a simulated image based on Zemax predictions. **Right:** An actual polarization image compared to a simulated Zemax result for polarization.

By measuring the position of the spots, we find that the lenslet separation is 10.63 pixels. Spectral separation is ~ 4.3 pixels perpendicular to dispersion and is ~ 23.5 pixels[1] along the dispersion axis, leading to a separation of ~ 6 pixels in H-band at the center of the detector. By measuring a bright emission line, we are able to determine that 94.9% of the light from a lenslet goes into a 3.5 pixel-wide spectral swath. To obtain polarization information, a Wollaston prism is inserted into the re-imaging optics path (Perrin et al., 2010). This generates two sets of microdots measuring the separate linear polarizations simultaneously. Spectral polarization is not possible since the Wollaston and spectral prisms cannot be installed at the same time. In polarization mode the micro-pupil are separated by ~ 7.2 pixels. The rotation, dispersion distance, spectral spacing, and overall performance of the spectra are in very good agreement with the Zemax model (Figure 3.6).

Measurements of the spectral resolution of the instrument were made by using

---

[1] Distance between two identical wavelengths

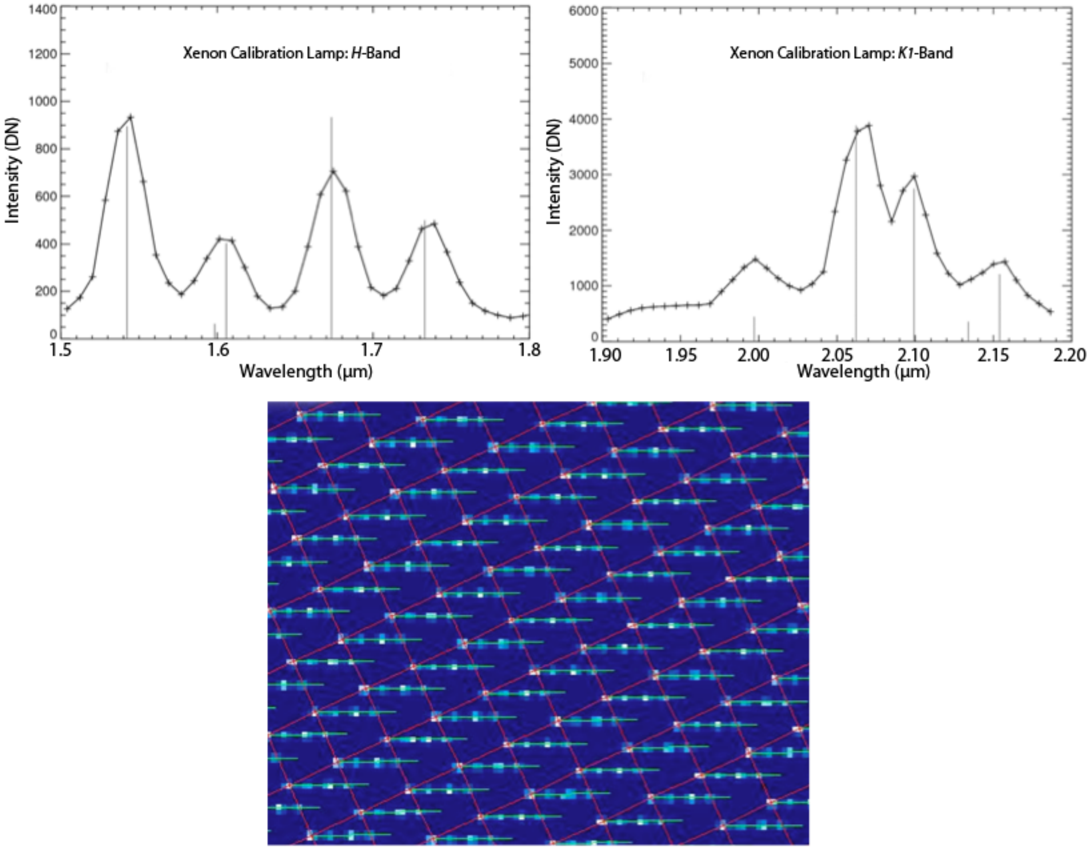

Figure 3.7: **Top Left:** *H*-band spectra of a Xenon source as reduced using the GPI pipeline. Results indicate a resolution of $R \sim 52$. **Top Right:** K1 (1.9-2.19 μm) spectra of Xenon source as reduced using the GPI pipeline. Results indicate a resolution of $R \sim 65$. Each meets or exceed the required resolution of the instrument. **Bottom:** Actual image as taken by the IFS detector with Xenon source in *H*-band before reduction with the Pipeline. Overlaid are the locations and length of the spectra as found by the GPI pipeline.

Xenon and Argon calibration lamps. These were fed into the GPI Data Reduction Pipeline (DRP) (Maire et al., 2010, 2012). The DRP identifies spectral features from the lamps to deduce a wavelength solution (Figure 3.7).

3.5 CCR Vibration and Induced Microphonics in H2RG Detector

The IFS uses two CryoTel GT closed cycle refrigerators (CCR) from Sunpower Inc., each rated at 15W of cooling power at 77K (Section: 2.9, Figure 3.8). The Sunpower CryoTel GT is a Stirling cycle cryocooler. The cryocoolers are cooled at the heat rejection surface via a removable water cooling jacket provided by Sunpower. Originally a custom copper jacket designed to cool the body of the CCR was cooled by using the waste heat from the CCR heat reject collars, but the cooling source has been subsequently replaced with air running though the same body copper jacket to reduce the chance of a glycol spill by reducing the number of lines inside the optics enclosure which carry glycol. The bodies are designed to operate without any cooling but will reach temperatures in excess of sixty degrees Celsius without cooling jackets.

The coolers were provided with a removable KF-50 vacuum flange. This was initially used to directly mount the CCR to the IFS dewar wall. While the Sunpower coolers are low in overall vibration, each cooler operates at 60Hz generating significant vibration at this frequency and its harmonics. A passive vibration absorber, tuned to 60Hz, was provided by Sunpower and when added into the system decreases the transmitted 60Hz vibration. However, by rigidly connecting the CCRs to the IFS, vibration energy not dissipated by the vibration absorbers is transferred into the dewar.

During lab testing, a localized source of read noise, on the order of ~ 100 electrons, was noticed in frames from the H2RG detector (Figure 3.9). This noise was seen to occur at a frequency of 120 Hz. Subsequent changes in the grounding scheme made little or no difference to the detector noise, in the localized region. Additionally, changes in the number of read channels (32, 4, 1) did not affect the position of the region of enhanced read noise. We determined that the amplitude

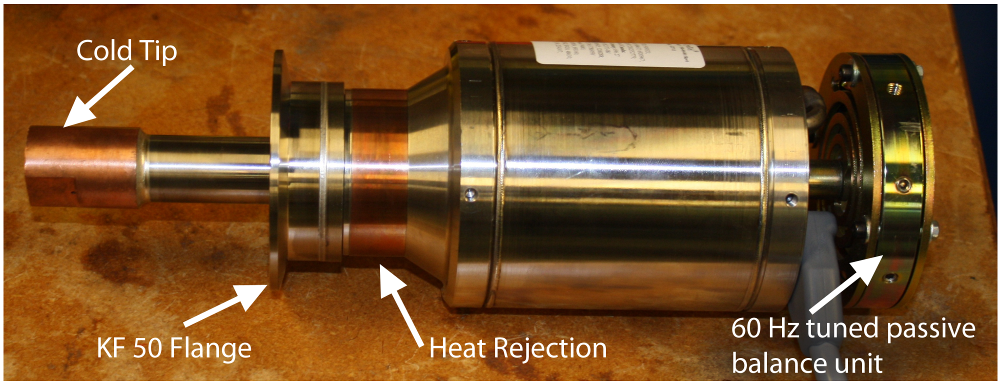

Figure 3.8: Sunpower CryoTel GT 15W cryocooler.

of the noise was dependent on the way in which the dewar was supported. By placing the dewar on the ground as opposed to suspending it from a rotation frame (figure 3.10), the noise was considerably diminished from ∼ 100 electrons to a few 10s of electrons. Further, by changing the amplitude of the CCR stroke, the amplitude of the noise was correlated to the power and vibration of the CCRs. The IFS H2RG detector uses three posts to attach it to its support structure (Figure 3.11). It was realized that the noise was located approximately between the H2RG detector's support legs.

Analysis of the vibration dampers showed that while reducing 60 Hz vibration along the CCR axis, some energy was shifted to 120 Hz in both the perpendicular axes to the CCR's center line axis. One of these axes is appropriate to stimulating a drumhead-like vibration in the detector, essentially causing microphonic noise in the detector. It is impractical to isolate the IFS detector head, so we decided to isolate the Sunpower CCRs from the rest of the Dewar and GPI as a whole. This was done by adding a set of all steel bellows at the KF-50 vacuum connection, and suspending the CCRs via a series of Sorbothane washers. This dramatically reduced the vibrational energy translated into the dewar.

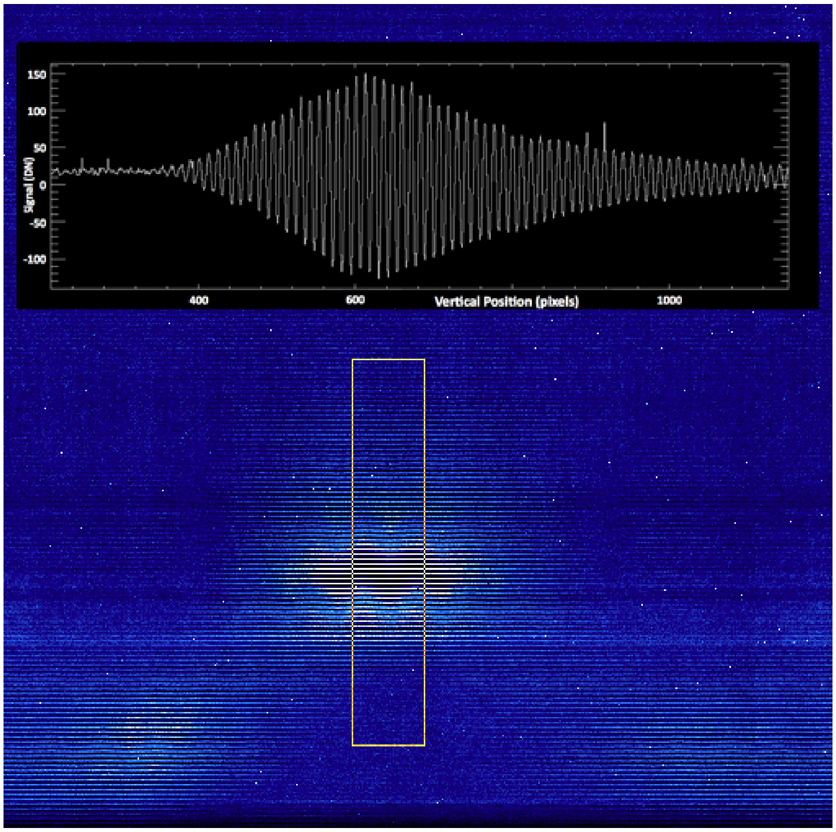

Figure 3.9: Microphonics noise pickup on the IFS H2RG detector. **Top:** A vertical slice though the displayed box region revealing the 120Hz frequency.

3.6 Vibration Management

While the CryoTel GP CCRs were picked for their low vibration in most frequency bands, they do produce significant vibration at 60 Hz and its harmonics. It was originally believed that the CCRs could be hard mounted to the IFS dewar, but over time this proved to be problematic, as the vibration was found to be extremely high in the narrow operational bands and could effect the GPI H2RG (Section: 3.5) by introducing a strong vibration in the detector and detector head. Further, concerns over the lifetime of internal mechanisms, vacuum seals, and the overall performance of GPI led to attempts to mitigate the overall vibration.

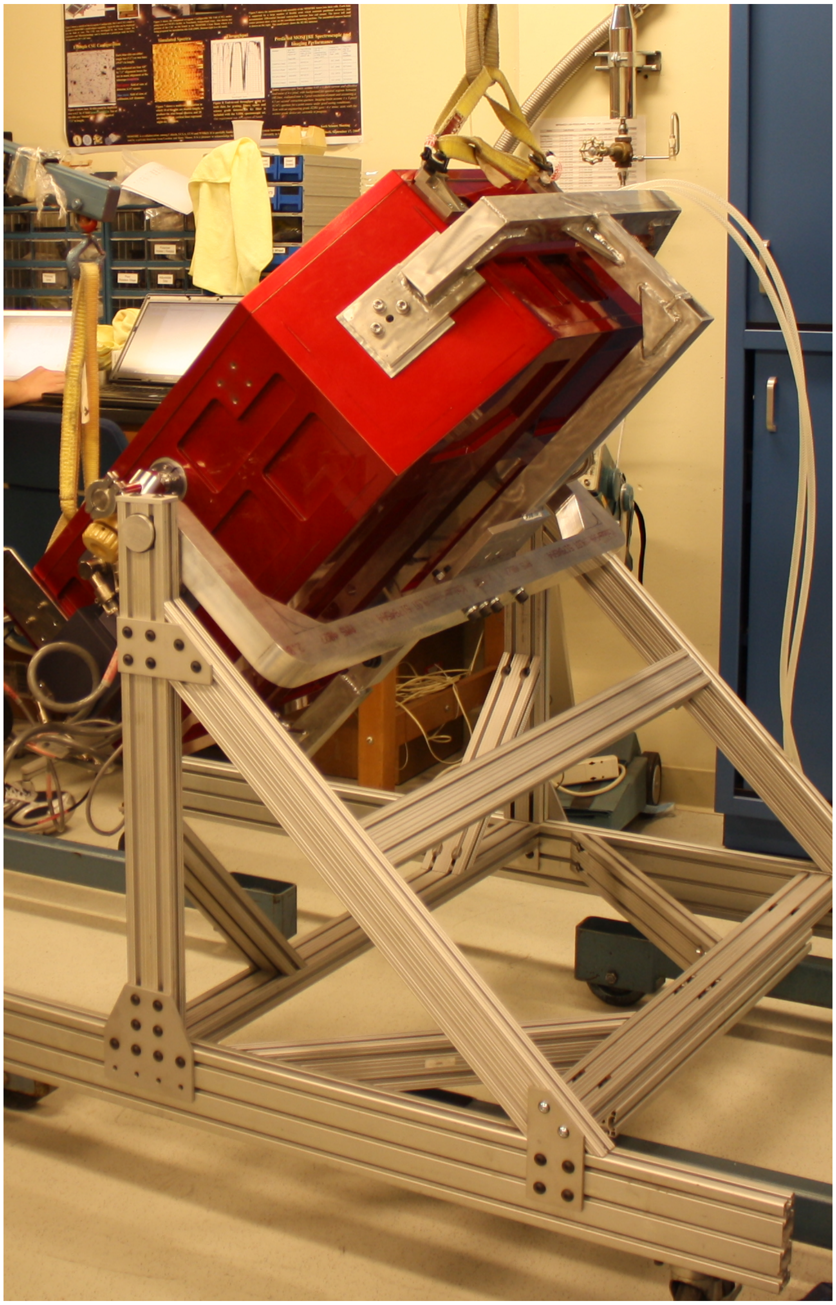

Figure 3.10: The IFS rotation stand with the IFS partially rotated between 0 and 90 degrees.

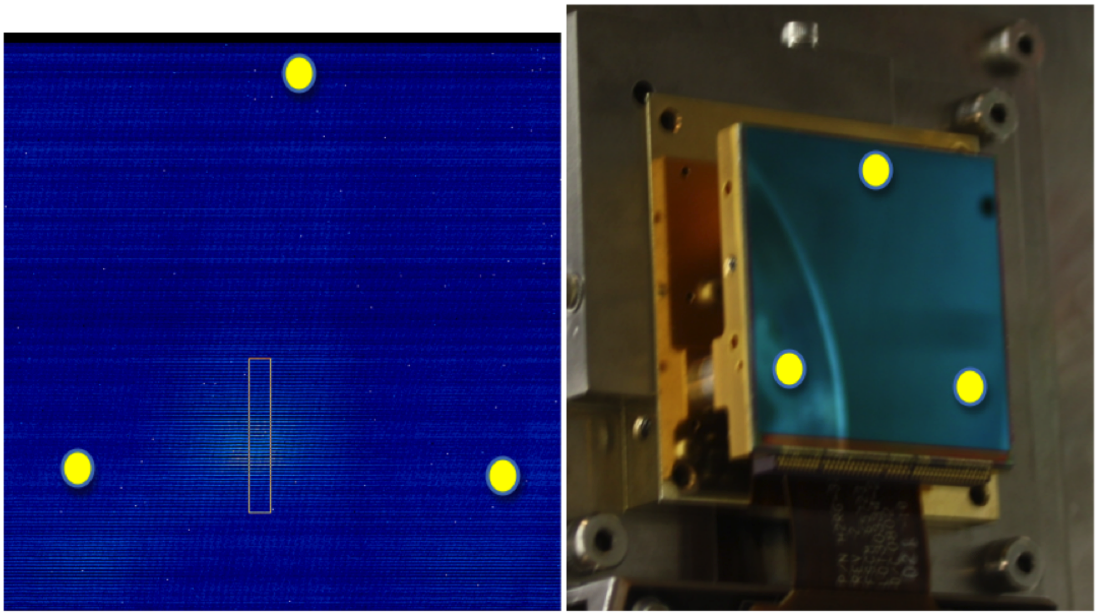

Figure 3.11: The location of the three legs of the H2RG detector in comparison to the location of the vibrationally induced noise.

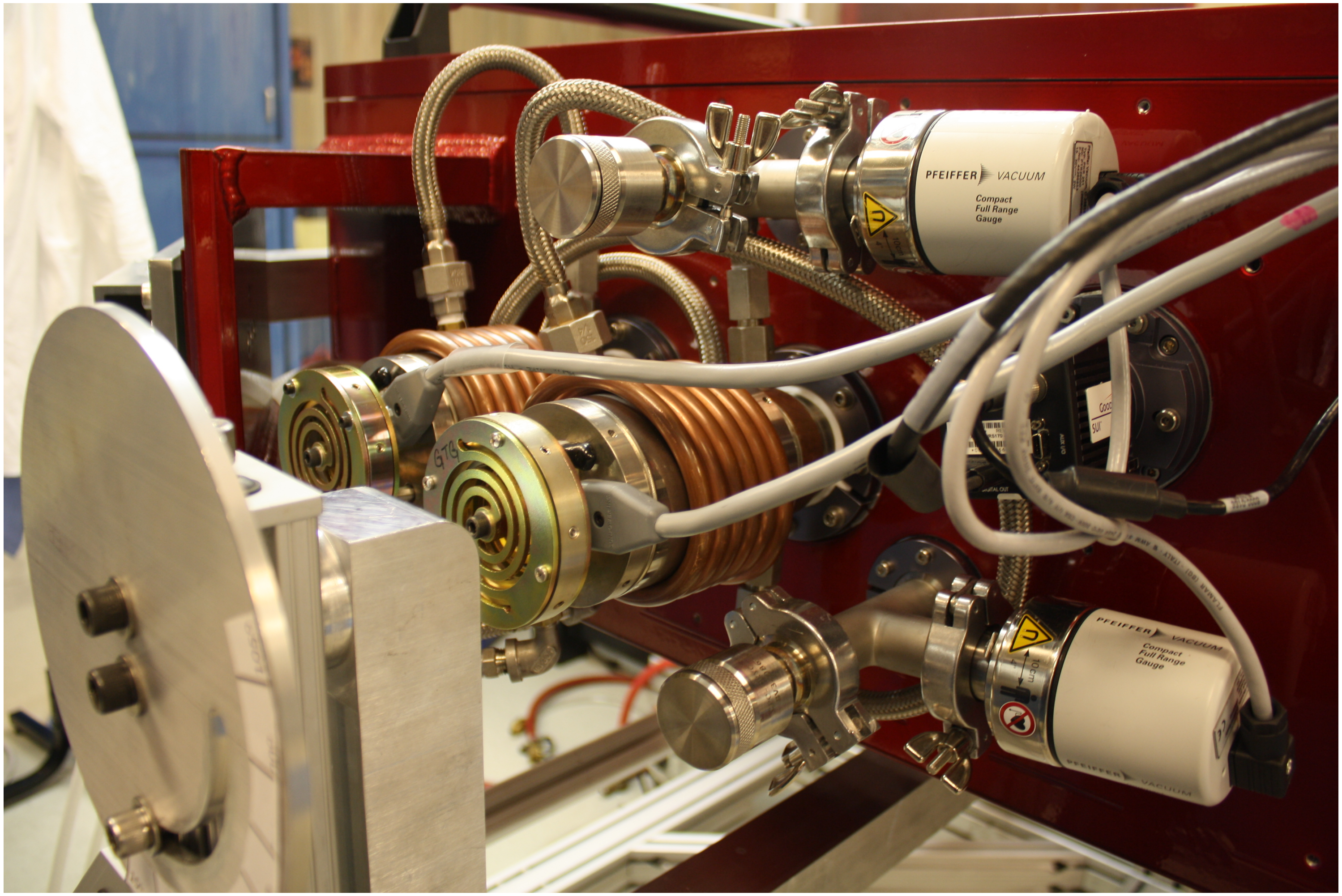

Figure 3.12: GPI IFS CCRs without rubber absorption assembly.

The problem was approached from two angles. The first, was to attempt to eliminate the generation of the vibration, and the second was to reduce the vibrational transmission into the IFS. The first attempt to reduce the source of vibration was to utilize the advantage that the two GT CCRs generated more cooling power then was needed and a small increase in temperature of the optics bench to reduce the power in each CCR was advantageous. Further, through discussion with the manufacturer they were able to produce a prototype board that had one logic unit to generate the CCR control signals and two driver units, where the second driver (slave) was connected to the master board, but with the piston movement commands reversed.

This setup was found to be problematic in that each driver board was powered independently, and it is possible to provide power to the slave driver without powering the logic board. This resulted in the CCR piston being driven hard into one end of its range, effectively turning the magnetic coil which drives the piston into a large resistor. Additionally, the slave driver board will immediately be damaged, to an unrecoverable state. Due to the occurrence of such an event, it was decided to abandon this method of reducing vibration with the generation one controllers.

The second approach used to reduce vibration involved reducing the amount of vibration transmitted into the IFS from the CCRs. Isolation was achieved by separating the CCRs with a set of steel welded bellows, and supporting the CCRs (Figures 3.12,3.13) by a set of washers made up of a vibration isolating material. As was reported in Chilcote et al. (2012), duromater 70 sorbothane did a spectacular job of isolating vibration from the dewar.

Using accelerometer measurements, the g-load on the detector head, going in and out of the plane of the detector decreased from an absolute peak of 2.0 g's to a peak of 0.17 g's at 60Hz. This reduction in vibration virtually eliminated any detectable level of microphonics when reading out the detector.

Unfortunately, design constraints, limited the size and amount of Sorbothane used. Further, after approximately six months we noticed that the Sorbothane washers were deteriorating under the atmospheric load, and vibrational stress. This resulted in a redesign, using instead rubber isolation pads. They are more robust against deterioration, but unfortunately transmit more vibration than the Sorbothane. While the rubber transmits slightly more vibration than Sorbothane, it is significantly less than would be present without any vibration isolation incorporated into mounting structure for the IFS CCRs. Further vibration mitigation was performed using a set of synchronized controllers. We now estimate that the microphonics is less than ten percent of the original amount observed.

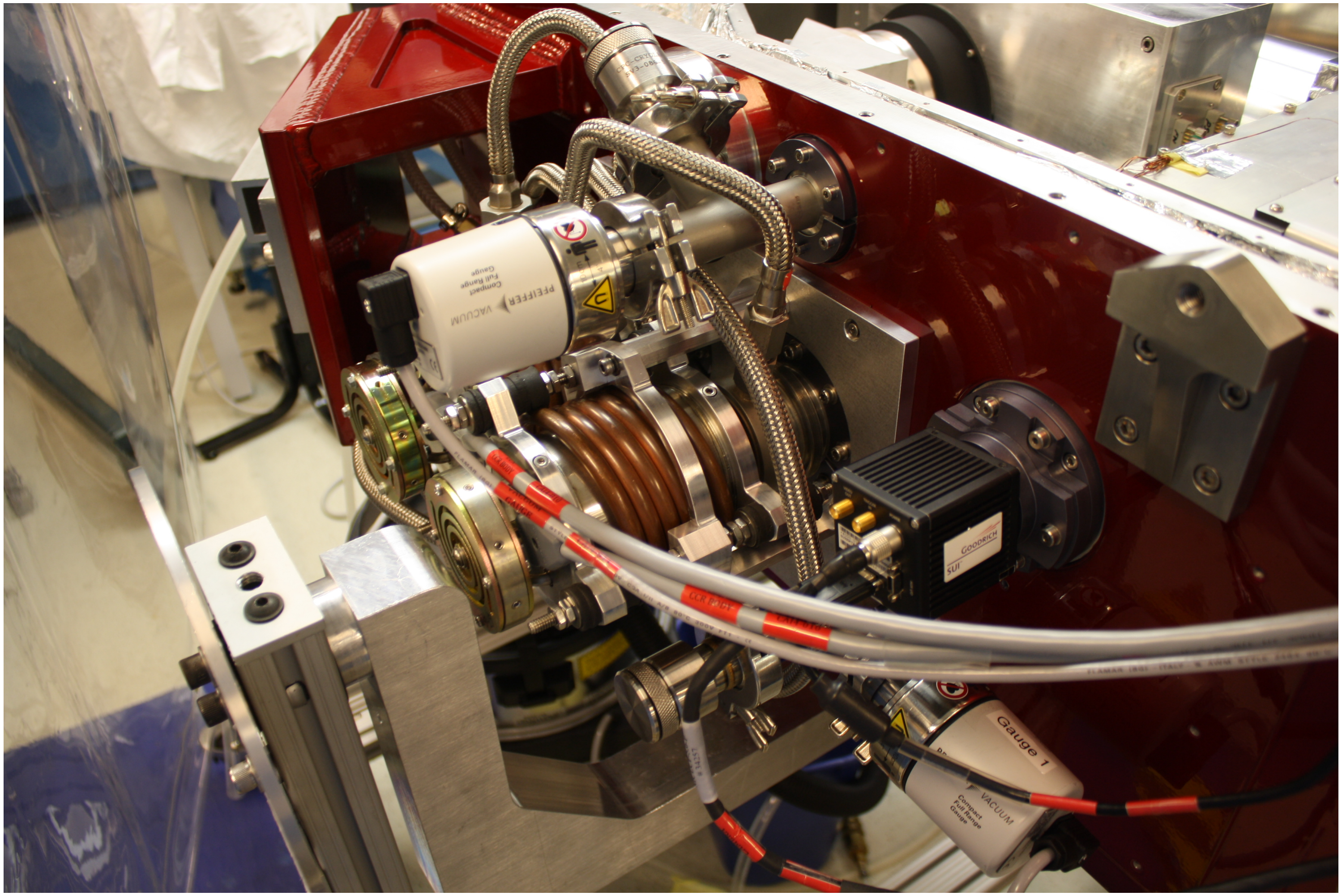

Figure 3.13: GPI IFS CCRs with the rubber absorption assembly.

In the Fall of 2013, Sunpower Inc. began producing their second generation controller with an add on to have one master 60 Hz sinusoidal wave to keep the pistons out of sync, but to allow the logic boards to remain separate. This second generation controller was installed into the IFS electronics enclosure in January 2014 in Chile, replacing the original first generation controllers. The overall solution to reducing vibration in the IFS and GPI due to the cryocoolers is to use both rubber washer supported cryocoolers to control the phase of each cryocooler to operate the cryocoolers in a state so that the overall vibration is minimized.

3.7 Evaluation of GPI IFS H2RG Readout Modes

The IFS detector is a $1 - 2.5\mu$m Teledyne H2RG (Section 2.8). Because the CMOS design allows for the detector to be sampled without the destruction of the original data there are multiple methods employed to measure the final signal value. The most frequently used method is Multiple Correlated Double Sampling (MCDS), sometimes called Fowler Sampling. In MCDS, the first half of the reads are subtracted from the second half of the reads producing a result which is proportional to the flux. This method serves as our primary noise baseline, but it is important to remember that it can be confusing to talk about a read noise in electrons for such an image, since the noise will depend on the exposure time that you scale the flux to. In other words, if the reads densely fill the exposure time, then the flux one naively calculates in a traditional MCDS is the integrated flux for an exposure time of

$$\frac{N}{2 \times (N-1)}. \tag{3.1}$$

Where N defines the number of reads performed.

The second main method is often called Up-The-Ramp (UTR) sampling, where the reads are treated as points along a linear graph of integrated flux vs. time. They are then fit to a straight line which is proportional to the flux. In our particular variation, it is also important to check for problems along the way, such as a cosmic ray hit. So, we compute the traditional linear fit, but do so through a weighted sum of the difference between any two adjacent readouts. Since each neighboring difference is itself proportional to the flux, the weights can be tuned to a particular expectation of the flux. This is explored in some detail in a set of papers by Offenberg et al. (2001) and others.

An important consideration in these weighted sums is that adjacent measurements of the slopes contain the same read in the middle, making the covariance matrix off-diagonal. If there is no flux expected (as with a dark), the ideal weight is to value the individual reads equally which is achieved by linearly increasing the weight towards the middle set of deltas (neighbor differences), and then linearly decreasing the weight. If no other changes were made, this would be mathematically identical to MCDS for a set of exposures spread throughout the integration time.

If, however there was a very strong flux present, then read noise is unimportant and one wants to maximize the weight for the first and last read (essentially ignoring middle reads which contain redundant information). In that case, an equal weight should be applied to all of the deltas. As Offenberg showed, choosing weights intermediate to flat and linearly varying often produced the best results.

To evaluate the readout modes and weighting schemes for the IFS, 50 dark images were taken in a mode where all the raw frames are dumped to disk (here after referred to as “write-all” mode). Traditionally these frames are interpreted by the IFS and a single reduced detector frame is written out. For this test each individual dark exposure produced 102 individual frames read from the H2RG detector. The frames were combined together using a variety of proposed algorithms to estimate the flux contained in the images and determine the equivalent noise of the particular algorithm, by comparing the results across the 50 images. The limit of 102 readouts was set by the ability to reliably get the entire set of write-all frames processed and written to disk due to memory constraints. The write-all frames are the reads returned by the JADE2 to the IFS brick before any processing, allowing the frames to be post reprocessed.

For all algorithms, 50 images were generated. These 50 images are then used to generate 2d standard deviation and median absolute deviation maps of the detector (Figures 3.14,3.15). A sub-region to avoid the microphonics is selected in each deviation map, and then the median is plotted in Figure 3.16, reweighted into an effective read noise in MCDS.

Each of the 32 output channels has a set of 4×64 pixels at the top and a second set of 4×64 pixels at the bottom of the column that are not exposed to light. These reference pixels can be used in a variety of ways to track common channel noise. These pixels can be medianed together to track changes in detector bias and subtracted from individual frames, or differences. In MCDS, this subtraction is always done after calculating the flux. In this analysis, we analyzed the case of UTR weighted sums where only reference pixels in the final flux measurement are used to subtract the weight once versus where the reference pixels are subtracted on each individual delta. With 512 reference pixels, the basic assumption was that the median of any one frame would have negligible noise so this variation would have no effect.

We calculate noise as a function of readouts, using the following possible algorithms:

- UTR fixed time: The first and last reads are always used, but as more reads are included, these are spaced out equally through the exposure time. For two reads, the first and last readouts are the only frames used. For three reads, a frame in the middle of the exposure time is used. For four reads, two intermediate reads are added, etc... In this case each pair of frames is subtracted, vertical reference pixel subtracted, and added to a weighted average. In the graphed data, the original weighting scheme was used (between flat and linear).

- Calculated as MCDS, fixed itime: The image is calculated as an MCDS with varying numbers of reads, but with the same total integration time. For example an MCDS-1 is two reads, with an integration time of 74 seconds, while an MCDS-32 has thirty-two reads on each end, with an integration time of 74 seconds.

- UTR reads define itime: For each number of reads N specified, the first N reads out of the 102 is used to calculate the flux. So in comparing to UTR fixed time, this is identical except the frames are packed closely together in time, while in UTR fixed time, they are spaced across the roughly 2.5 minute total exposure time. Again, vertical reference pixels are subtracted to each pair difference, and again this data used the original weighting scheme.

- UTR with MCDS weighting reads define itime: This is a computed image like “UTR reads define itime” but with a linear weighting scheme to the final value should be equal to having the lower half of the reads subtracted from the upper half (an MCDS). The difference is the reference pixels are subtracted to each delta.

Additionally, we calculate all of the above, but with the reference pixel subtraction moved to the final step, as opposed to subtracting it from frame difference. All of these different schemes are plotted in Figure 3.16. Further, this scheme is not overly effected by the microphonics caused by vibrational noise (Figure 3.17). In conclusion, we find that a weighted intermediate scheme is best, but with the reference pixel subtraction moved to the last step.

While we do not evaluate the noise of the system for an exposure time longer than roughly 2.5 minutes of total exposure time, this 2.5 minutes covers the major fraction of the integration times expected to be performed with GPI.

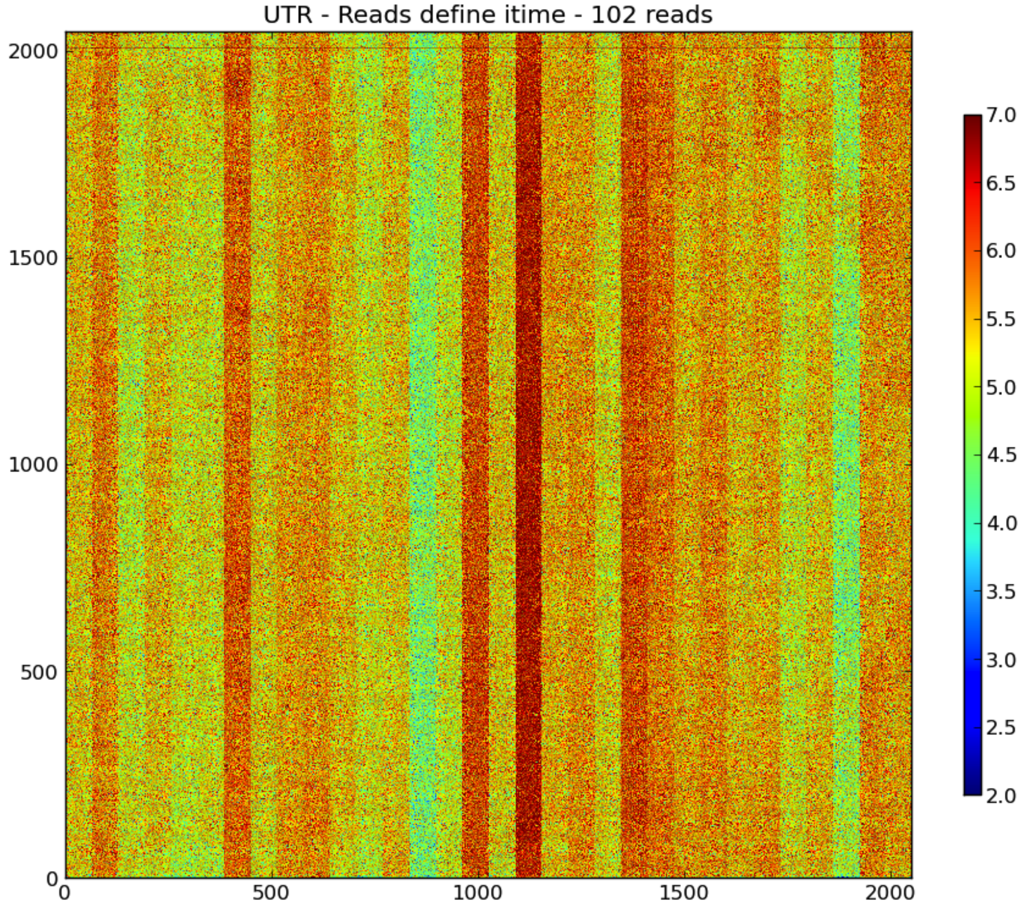

Figure 3.14: An evaluation of the read noise after 102 reads in the detector with the channel bias reference pixels subtracted from each delta in the UTR readout.

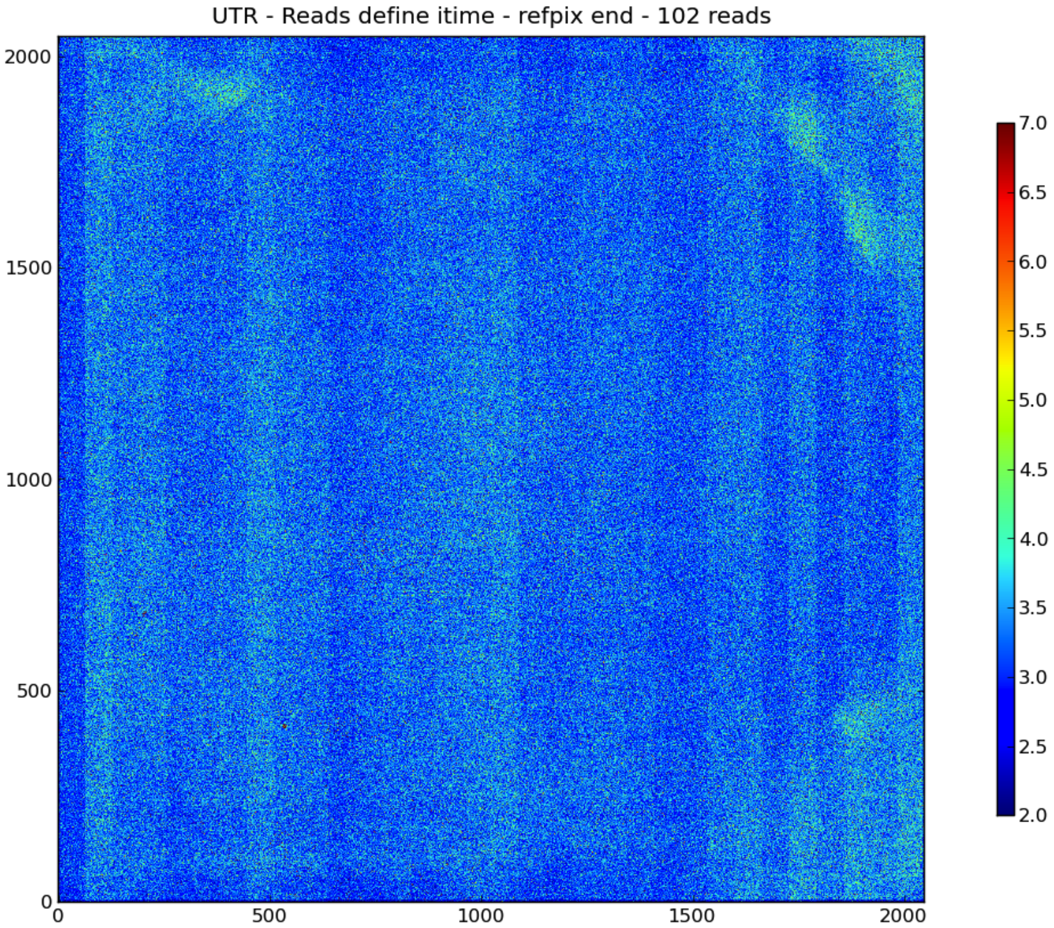

Figure 3.15: An evaluation of the read noise after 102 reads in the detector with the channel bias reference pixels subtracted from the final frame.

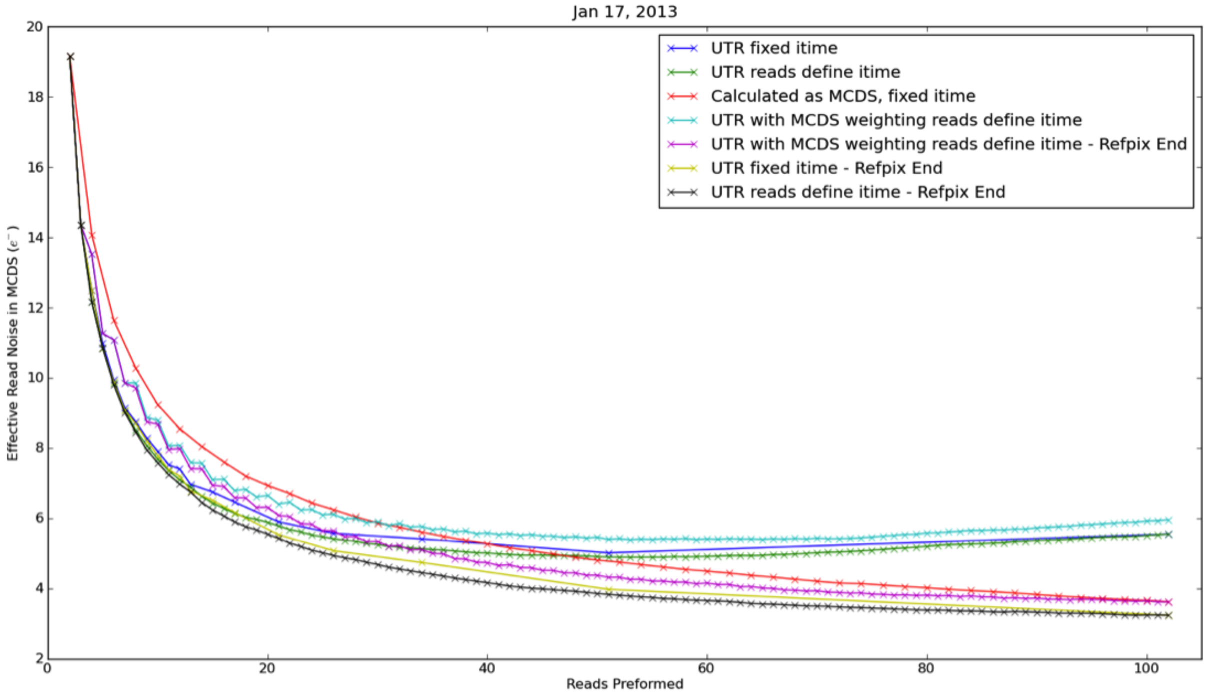

Figure 3.16: An evaluation of different weighting schemes for UTR sampling from the GPI H2RG. These different weighting schemes are evaluated against the reference pixels being subtracted on each delta between individual reads versus at the end of the entire sequence.

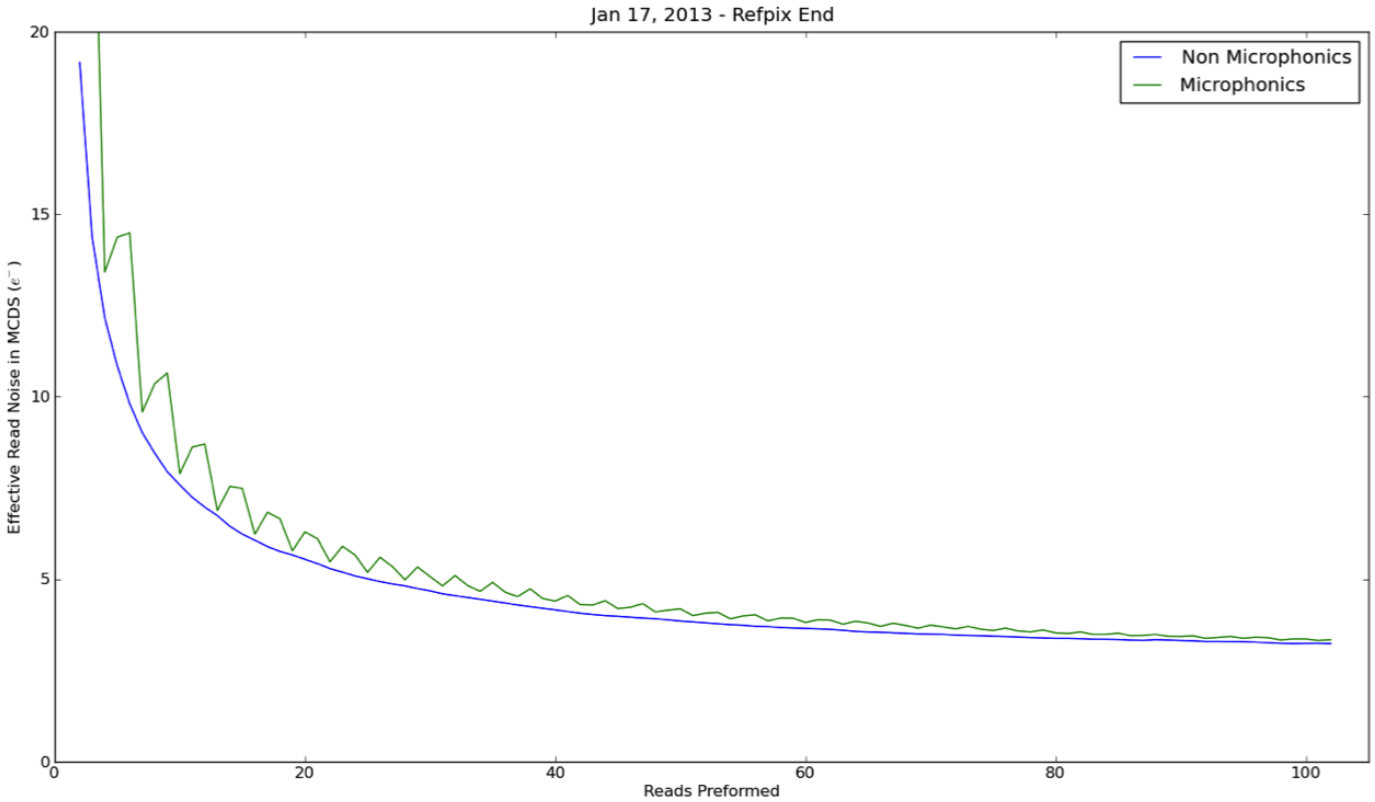

Figure 3.17: Using the selected UTR weighting, we compare the read noise of a region with microphonics to a region without microphonics.

3.8 Detector Ground Loop

Upon delivery of the integral field spectrograph to the University of California, Santa Cruz in late 2011, and subsequent integration with the other GPI subsystems in early 2012, a substantial increase in noise was discerned in the GPI detector (Figure 3.18). This noise did not have the same pattern and look like microphonics noise (Section: 3.5), but instead varied in location with time, indicative of an electrical issue. Unlike a pickup signal, the noise was not sinusoidal in its appearance, but was pulsed, having a very abrupt start and end, with a regular period (Figure 3.19).

Suspicions quickly focused on the GPI detector power supplies. While both the digital side and analog side of the detector electronics require 5V, it is to the user's advantage to run the two sides off of separate 5V sources. The digital electronics are powered from the possibly noisy 5V power supply used in the Windows computer, while the analog side, which is used to set and maintain voltage on the detector, are derived from a clean, regulated 5V power supply. At the UCLA Infrared Lab there was no effect seen from operating in this configuration.

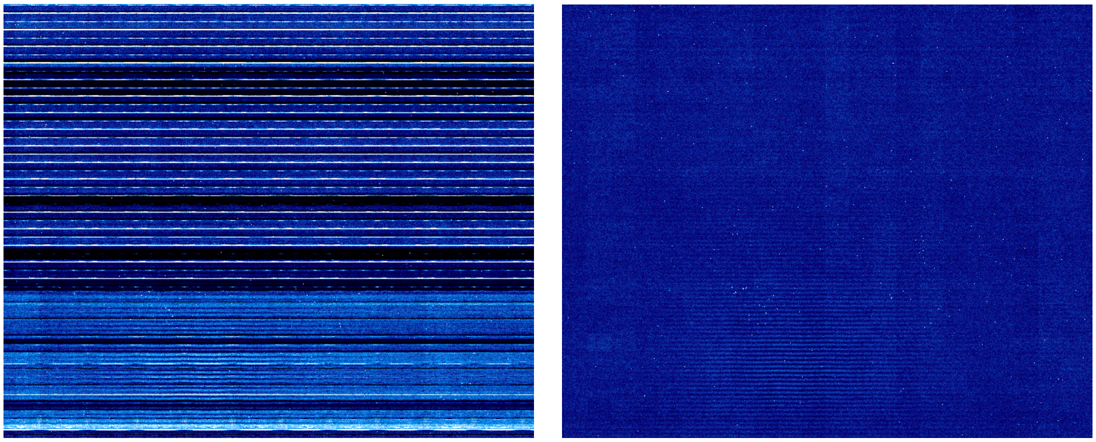

Figure 3.18: **Left:** The IFS with the ground loop introduced from the power outlet ground line. **Right:** The IFS detector running on wall power for its clean 5V analog power supply, but with the computer running from battery power isolated from the GPI main facility power.

By changing the gain in the analog-to-digital converter, we noticed that the noise increased in proportion to the change in gain. This indicated that the noise was not localized to the detector itself, but was more likely present in the analog-to-digital converter, and was possibly leaking between the digital and analog power sides of the electronics, at a point where they merged. Isolating both the analog and digital electronics power supplies was shown to improve the readout noise in certain circumstances by Dorn et al. (2008). This was achieved by using a fiber based USB communications scheme. Powering both the analog side and the digital side of the GPI detector off of a battery, removed the ground loop (Figure 3.18). Further investigation showed that the noise only appeared when using the 5V computer power supply, while the computer was connected to the ground used in the GPI power strip. To isolate the computer, the power supply was modified to use the chassis ground through the computer case instead of the power supply ground. This kept the computer grounded, but removed the noise source from propagating along the 5V digital supply.

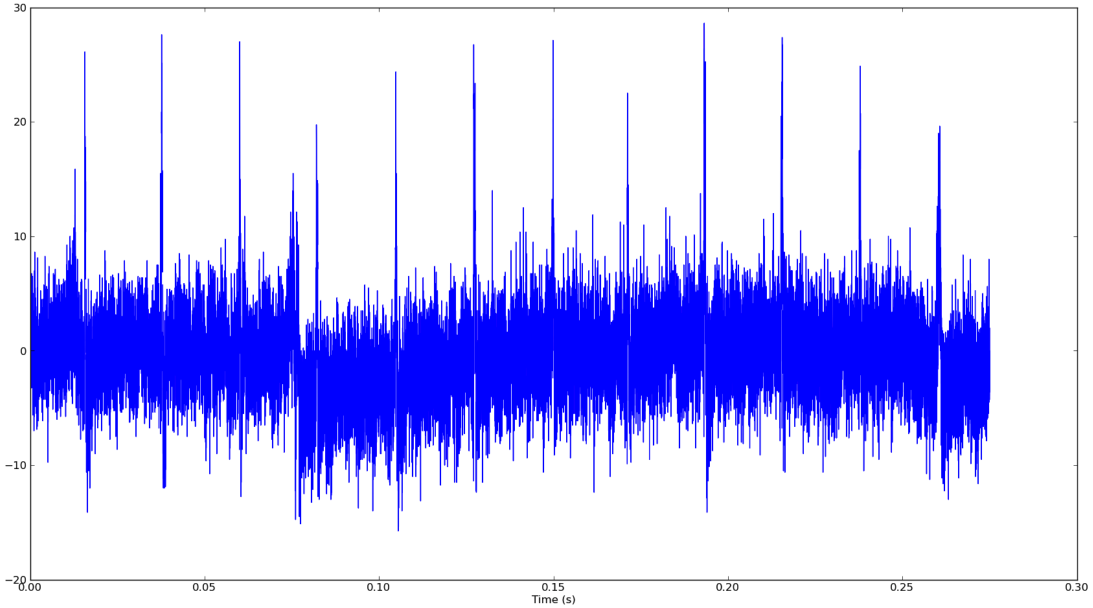

Figure 3.19: Because it takes a period of time to readout the detector, by using the clocking cycle the H2RG can act as an oscilloscope to sample the read noise. This figure represents a small sample of the 1.45479s readout time, but shows the non-sinusoidal nature of the ground loop.

3.9 Spaxel Flexure and Improvements

Since GPI is not installed in a gravity invariant environment, it was important to check for movement of the lenslet micropupil PSFs with respect to the detector. With spaxel movements, differences in the quantum efficiency both pixel-to-pixel and intra-pixel sensitivity can effect the flat field. Additionally, in spectral mode, the spectral solution can change as the spectra shift on the detector. We performed testing on the IFS flexure (figure 3.10) to identify possible shifts, and to attempt to reduce their effects. The work presented here encompasses the testing performed at the UCLA Infrared Lab before the IFS was integrated with the remainder of GPI. No modifications have been performed on the instrument after shipment to attempt to change these performance results; though testing has been performed by other members of the GPI team after delivery to UCSC.

The cryogenic slide which holds the prisms has three different operating modes; spectral: where an "air-spaced" dispersion prism can be inserted, polarimetry: where a Wollaston prism can be inserted in place of the spectral prism, or open: where nothing is inserted into the beam and the lenslet array pupil images can be sampled by the detector. This allows for each prism and the open optics to be considered independently for flexure.

Initial testing showed that the pupil spots and spectra were observed to move multiple pixels when the dewar was rotated around its center of mass from 0 to 90 degrees. This included the direct mode when no prism elements were inserted into the beam. To correct for this movement, blocks were glued beneath the IFS detector head to reduce the possibility of the IFS detector focus flexure sagging with gravity due to the cantilevered weight of the detector and its mount. Further, we reinforced the clips holding the two fold mirrors to prevent their movement with changing gravity orientation of the IFS.

On the subsequent cool down of the dewar, we noticed smaller movements without the prism inserted, but a significant shift in the spectra remained when using the prisms. The spectra mode moved by greater than three pixels perpendicular to the dispersion direction. A smaller but still significant motion was notice in the Wollaston prism as well.

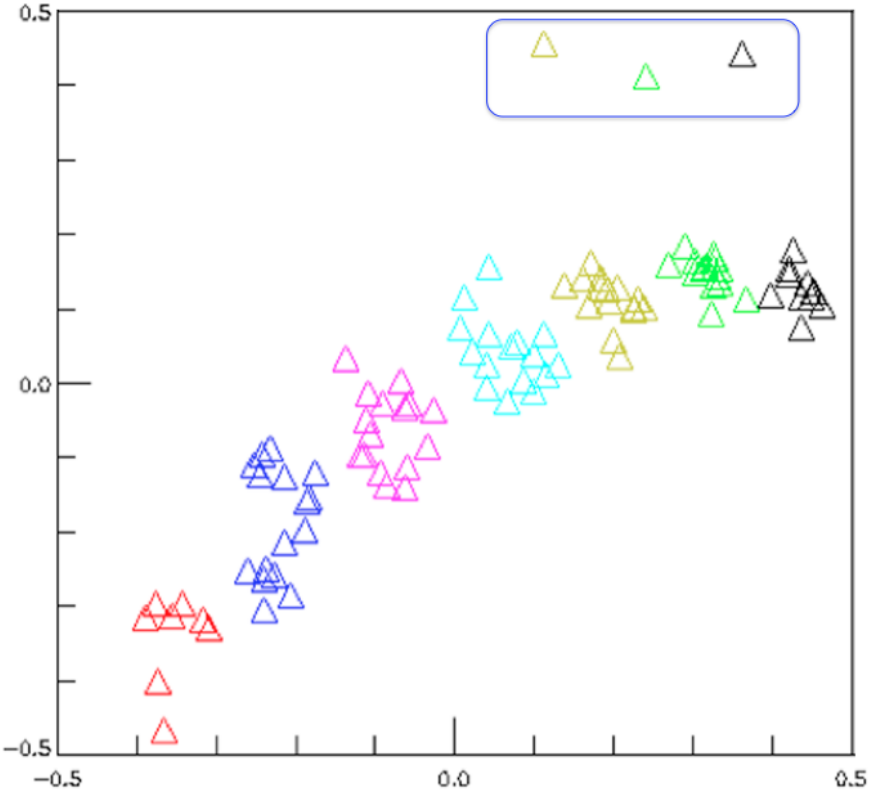

Figure 3.20: Measurements made in the final configuration of the lenslet flexure on the detector at UCLA. These measurements of the position of lenslet spots as the dewar is rotated between different gravity orientations. The entire box represents one pixel, with the measurement made by measuring the shift of many lenslet spots The first three triangles identified by a blue box are the first three points after the IFS has been cooled down, but before any rotation has occurred such as to allow the optics to settle into their holders. Black: 0 degrees, Green: 15 degrees, Yellow: 30 degrees, Cyan: 45 degrees, Magenta: 60 degrees, Blue: 75 degrees, Red: 90 degrees.

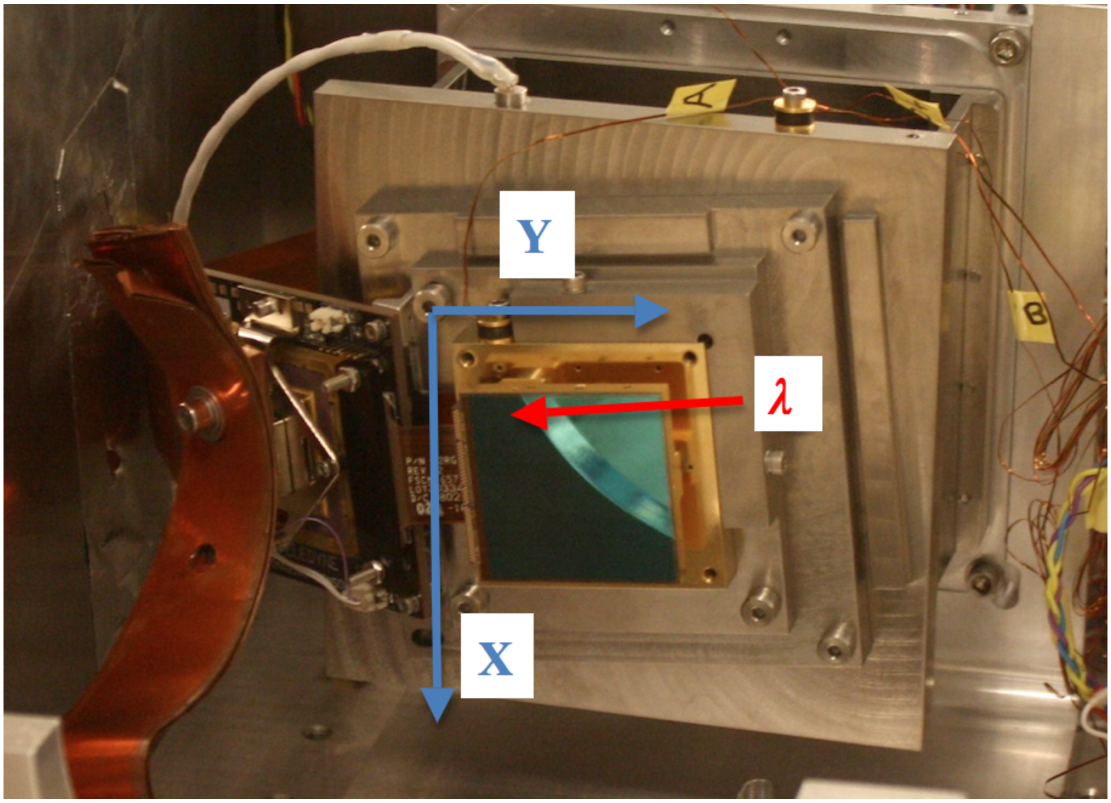

Figure 3.21: The IFS H2RG installed on the flexure / focus stage with the orientation of the spectral dispersion labeled.

Element	Motion from 0.1mm displacement higher on bench (mm)	Motion from 0.1mm displacement inward on horseshoe (mm)	Motion from 0.1 degree tip (mm)	Motion from 0.1 degree tilt of inside edge forward (mm)
Collimator-1 (ZnS)	-35, 0	0, 34.5	22, 0	0, -22
Collimator-2 (BaF2)	-13.8, 0	0, 14	35.5, 0	0, -35
Collimator-3 (BaF2)	-73, 0	0, -72	14.5, 0	0, 13
Collimator-4 (BaF2)	-110, 0	0, -109	6, 0	0, 6
Collimator-5 (ZnS)	60, 0	0, 59	23, 0	0, 21
Camera-1 (BaF2)	-145, 0	0, 145	-12, 0	0, 12
Camera-2 (S-FTM16)	67, 0	0, -67	-6, 0	0, 7
Camera-3 (ZnS)	-22, 0	0, 22	-22, 0	0, 22

Table 3.1: Tipping and tilting individual lenses in the IFS causes different displacements of the lenslet pupil pattern on the detector.

Element	0 – 45 degrees	45 – 90 degrees
Collimator-1 (ZnS)	**shift up** / **tilt back**	up & out / tip back & outer edge back
Collimator-2 (BaF2)	**shift up** / **tilt back**	up & out / tip back & inner edge back
Collimator-3 (BaF2)	**shift up** / tilt back	**up & in** / tip back & inner edge back
Collimator-4 (BaF2)	**shift up** / tilt back	**up & in** / tip back & inner edge back
Collimator-5 (ZnS)	shift down / tilt back	down & out / tip back & inner edge back
Camera-1 (BaF2)	**shift up** / **tilt forward**	up & out / tip forward & inner edge back
Camera-2 (S-FTM16)	shift down / **tilt forward**	down & in / tip forward & inner edge back
Camera-3 (ZnS)	**shift up** / **tilt forward**	down & out / tip forward & inner edge back

Table 3.2: A comparison of the motion required to shift the pupil pattern as seen on the detector, with bold indicating the motin the lens could physical undergo while the dewar is rotated.

Because this flexure only occurred when the prisms were inserted, the most likely cause was related to the insertion of the prisms. Zemax modeling was done to identify the type of motion which could produce this movement. Inserting or removing the prism elements perpendicular to the beam causes no shift in the spot locations. This was further verified through testing, as it is a controllable movement parameter. Tipping the entire prism assembly forward by 0.1 degrees caused only a one micron shift in the focal plane[2]. Rotating the entire prism by 0.1 degrees made a one-micron shift in the dispersion direction, but no shift perpendicular to dispersion. Tipping the second prism forward, so that the separation between the prism changed, by only 0.1 degrees caused 30 microns of displacement perpendicular to the dispersion with a shift of less than one micron in the dispersion directing. Tipping the second prism along the dispersion direction by 0.1 degrees caused a 124-micron shift in the dispersion direction but no associated perpendicular shift (Figures 3.20,3.21).

Upon closer inspection, we noticed that it was possible for the prisms to tip and tilt independently in their holders. Further, the extra play in the prisms while in their holders was consistent with the non-repeatable and jerky motion seen in the spectral mode. By modifying the spectral prism mounts, we were able to remove their independent movement, which was verified with the remaining flexure that was seen with subsequent testing being uniform in the spectra, Wollaston, and open positions, indicating that it is derived from the remaining optical components. This modification consisted of increasing the strength of the flexible washers holding the prisms in place, but not strengthening them to the level where the prism optics might be damaged.

The remaining motion was most likely due to another optic flexing in its mount. We rotated the dewar between 0 and 90 degree orientations many times tracking the motion of the spots on the detector due to flexure[3]. This included

---

[2] The H2RG has a pitch of 18 microns.

[3] We ignored the very first tipping and tilting of the IFS after a cryocycle as to allow optics

measurements in the spectral, Wollaston, and open prism positions. We found that over all of these measurements, there was no discernable dependency on which prism was used, leading us to the conclusion that the motion was due to another optic. We found that the bulk motion of the spots was ~ 0.8 pixels perpendicular to dispersion, and 0.3 pixels in the dispersion direction. In each orientation, there was about 0.3 pixels of scatter between different data sets. Further, starting at one end of the scatter as the dewar is rotated, the points tend to stay near the same end of the scatter. For a given angle, the scatter amongst the points tends to lie along a line with less than 0.1 pixels of perpendicular scatter. The orientation of the scatter lines appears to rotate being approximately 20 degrees (y over x) when the dewar has a 90 degree from horizontal orientation, and changing to roughly 40 degrees at a dewar orientation of 0 degrees.

The scatter is very consistent with a loose optical element that is tipping in its mount during dewar rotation. The fact that the angle of dispersion changes as the dewar tips over may give some indication about which element is changing. In the 90 degree orientation, most elements have an axis that is parallel to gravity so one would not suspect a strong dispersion along either x or y. But, the middle optics sitting between (and possibly including) the fold mirrors always have an optical axis perpendicular to gravity and one might expect the relative amount of x versus y motion to depend strongly on orientation. We suspect that one of these lenses is moving a very small amount due to gravity.

In order to understand the possible source of the motion, coordinate breaks were added around each of the lenses in the Zemax optical model (Figure 2.6). The lenses were then shifted laterally and tilted to determine the magnitude and direction of spectral motion. We assume that the motion must be because of flexure in the system, if there was a loose element, we surmise that the shifts would be sudden and non-repeatable as they were for the prisms. Using the

---

to relax in their mounts

motions indicated in table 3.1, we determine the motion that the lens would have to undergo in order to generation the motion of the spot pattern that we see (Table 3.2).

The result of this testing is that a deflection of collimator elements 3 or 4 could move with gravity in a way which would also explain the shifts that are seen of the pupil pattern. Further, they require a small motion to produce the needed deflections. At an IFS review by GPI and Gemini, it was decided that these shifts are small enough to be compensated for in software, and further, due to the small nature of the movements, it is more likely that an attempt to reduce the lenslet pupil motion further would possibly damage or disrupt the already highly aligned optical elements.

3.10 IFS Thermal Management

A flexible copper strap is used to connect the IFS CCRs which are mounted to the outside of the dewar, to the internal optical bench which changes in size and position as the dewar cools from ambient temperature to $\sim$ 70K. Providing a thermal path to the IFS CCRs that was compact, had a high thermal conductivity, and provided enough flexibility so as to not damage the IFS CCR cold tips was a design challenge. At cryogenic temperatures, the conductive and radiative load does not substantially change over a few degrees Celsius. But, the cooling capacity of the CCRs changes substantially, thus for a given thermal load, they will always reach the same operating temperature. By reducing the thermal impedance in the link between the CCR tips and the IFS's optical bench, we can lower the optics bench's operating temperature. Proving a highly flexible link that provided the low thermal impedance for 15 watts of cooling capacity was challenging and took several designs.

Thermal conductivity is proportional to the cross-sectional area of the strap divided by its length. Making the copper strapping longer as to provide more flexibility decreased the thermal conductivity. Unfortunately, increasing the thickness of the strap bundle did not appreciably increase the thermal conductivity because thermal conductivity can be low as a result of touching / mated surfaces. Using higher amounts of solid copper did improve thermal conductivity, but at the expense of adding a high amount of weight and inflexibility to the end of the Sunpower GT CCRs.

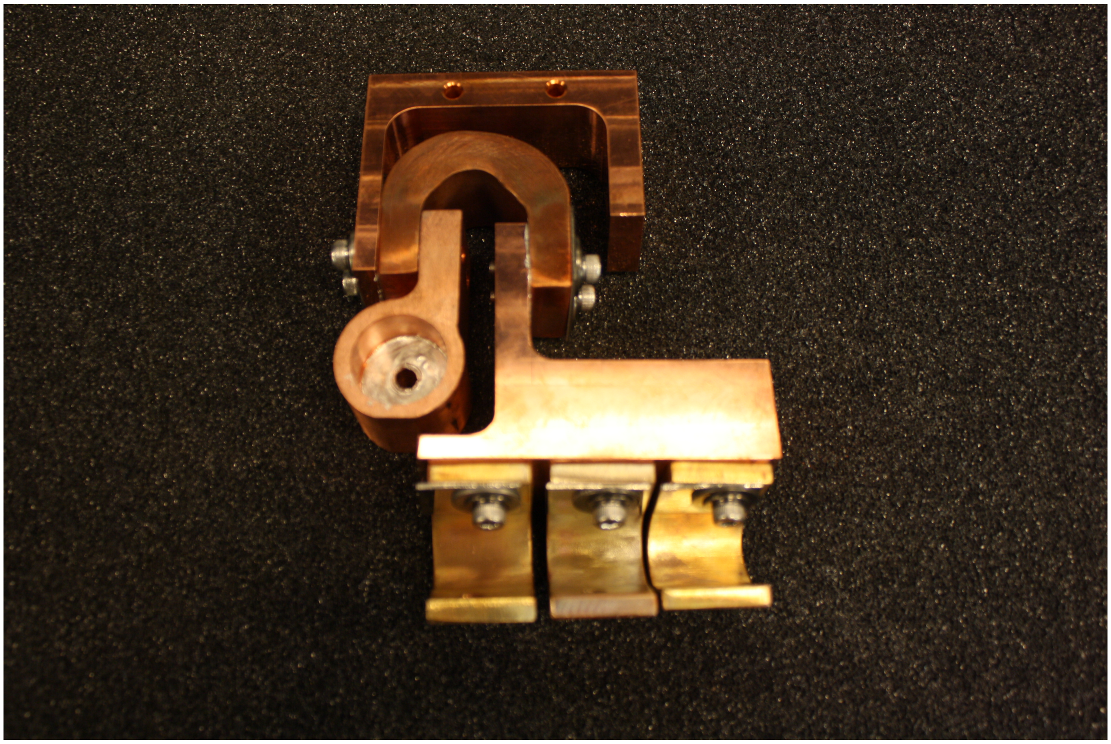

Figure 3.22: GPI IFS Press-welded copper straps. Assembled such as to attach the tip of the CCR to the optical bench, but to allow for the differential contraction between the cold bench at approximately 70 Kelvin and the dewar external walls, where the CCR is mounted, at ambient temperature ($0 - 20$ degrees Celsius).

While the straps were designed to be flexible, there was concern that limited flexibility in all orientations could put undue stress on the fragile CCR tips. As a result of in-lab testing, we found that some straps had $< 5\%$ of their theoretical conductivity. Attempting to weld the end of the straps caused the thin copper straps to disintegrate, while attempting to add solder to the tips of the strap bundles was difficult because the high thermal conductivity of copper resulted in the solder flowing further than desired.

In the end, our solution was to use press-welded copper straps (Figure 3.22). These straps are often used as flexible founding straps. Many different methods — such as passing a high current while pressing together multiple sheets of copper with a high amount of force — are used to bond the copper straps together so that the stack of copper straps shows little resistance (electrical / thermal) across the weld allowing the entire strap to carry the load. Lab testing showed that our conductivity to be $> 40\%$ across the strap[4]. This strap design has been used within the GPI IFS to couple the cryogenic optical bench to the CCR cold tips.

3.11 Additional Challenges

The IFS has had many additional challenges related to its design, construction, and performance. These are important to the overall operation of the IFS, and while worthy of mention, do not necessitate the detailed description demanded by the preceding sections. They are listed here for completeness, with a rudimentary summary.

- Initial testing and characterization of the IFS Pupil Camera. This includes many of the same types of tests that were performed on the astronomical detector, but the Pupil Camera uses a different technology, and method of reading out and reporting the frames back to the IFS computer. The camera was tested and configured to optimize performance for the environment and demands of an astronomical imaging instrument.

---

[4] This measurement is limited by test setup and procedures

- Diagnosis, operation, and repair of the IFS Vacuum gauges. The IFS vacuum cold cathode gauges have a finite life. This operational lifetime was used at an unexpected rate due to the need for 18 cooldowns of the instrument, instead of the original 8 which were initially planned, often leaving the Vacuum gauges at a high pressure for the cold cathode resulting in decreased operational life.

- Creating a seal around the uninterrupted JADE2 communications cable. My work with the JADE2 communications cable involved designing and testing a method of passing the continuous JADE2 cable through the pressure bulkhead of the dewar without introducing any cable breaks. This required that I investigate a variety of designs, create test components, and prove that the resulting design maintained a vacuum seal.

- Modeling thermal environment and copper strap performance. With initial difficulties in reaching the desired temperature, and later difficulty with overall CCR performance, understanding the thermal environment is critical.

- The reduction of light leaks in the IFS. This included a light leak caused by a caustic reflection before the lenslet array, and light leaks after the optics reflecting off the field flattening lens and falling onto the detector.

- Understanding IFS detector read time and overheads

- IFS software testing and verification. I verified that all alarms and software complied with the software acceptance test plan. Further, I independently wrote test code to check the robustness of all of the IFS detector algorithms written by Jason Weiss in C#.

3.12 Summary

UCLA has designed and constructed the Integral Field Spectrograph for the Gemini Planet imager. GPI is one of a new generation of instruments being built to carry out the difficult task of directly observing extrasolar planets. Our testing has shown that the GPI IFS has excellent optical quality, robust mechanisms, a high level of internal metrology, and excellent filter throughput. The optical design closely matches the predicted results from Zemax. While the Sunpower CryoTel GT closed cycle refrigerators have low vibration, they induce vibration at a few select frequencies. This was found to introduce microphonics noise into the IFS's H2RG detector. By isolating the vibration introduced from these coolers, the induced noise has been substantially mitigated. The read noise on the detector for a single CDS frame is near expectations, and the weighting scheme for UTR frames has been optimized to produce the optimal results. Finally, due to an unfixed gravity orientation, it is extremely difficult to prevent spaxel movement on the detector, but by improving the robustness of the IFS, spaxel shifts have been substantially reduced. All of these results meet the needs of GPI and should make the IFS an excellent addition to the overall instrument.

CHAPTER 4

A study of the massive planet Beta Pictoris b — L$'$ observations using the Keck Observatory

4.1 Introduction

Beta Pictoris (HD 39060) is an A6V (Gray et al., 2006) star located 19.44 ± 0.05 parsecs from Earth (van Leeuwen, 2007) and is one of a handful of stars with a directly imaged extra solar planet (β Pic b). The estimated age is $\sim$ 12 Myr old using the moving group's location on the H-R diagram, and lithium equivalent widths intermediate in strength between Tucana-Horologium and TW Hydrae stars as an estimator (Zuckerman et al., 2001). Recently, a revised estimate was proposed using the lithium depletion boundary age of 21 Myr for the Beta Pictoris moving group (Binks & Jeffries, 2014).

In 1983, IRAS observations indicated a significant IR excess from β Pic (Aumann, 1984; Aumann & Walker, 1984). The β Pic system represents one of the earliest examples in which high contrast imaging was used to directly detect a circumstellar disk by resolving the edge-on systems of freshly produced dust (Smith & Terrile, 1984). Scattered-light studies of the morphology of the β Pic circumstellar disk have revealed an inner warped component to the disk at less than 80AU, inclined by 2–5 degrees with respect to the main disk (Kalas & Jewitt, 1995; Heap et al., 2000; Golimowski et al., 2006). Asymmetries in the disk structure have been attributed to the possibility of planetary perturbations (Burrows et al., 1995; Mouillet et al., 1997; Heap et al., 2000). The deformed structure of the circumstellar disk can be attributed to a giant planet at a slightly inclined orbit (Gorkavyi et al., 2004; Augereau et al., 2001; Thébault & Beust, 2001; Lagrange et al., 2009a). Observations by Okamoto et al. (2004) at 10 μm found concentrations of silicate dust in several bands around β Pic, which was interpreted as resulting from planetesimal belts. These belts should not be stable over long periods of time, unless a planetary object is orbiting around the star enforcing the belts through resonant interactions. Simulations by Freistetter et al. (2007) found that a set of three planetary objects would explain these planetesimal belts. These different observations were made with the growing consensus that the young debris disk orbiting around β Pic hid a giant planet, and possibly held up to three giant planets forming and sculpting the debris disk. This led to a successful search for more evidence of an extra solar planet, or the direct detection of the planetary body.

In Lagrange et al. (2009a) finally discovered a planetary candidate around β pic using observations from 2003, in L' (3.5–4.1μm) on the Nasmith Adaptive Optics System (NACO) instrument. A single detection is not sufficient to determine whether this candidate source was a gravitationally bound companion, or an unrelated background star, whose projected position in the plane of the sky happened to be close to β Pictoris. Observations in January and February 2009 did not detect the companion (Lagrange et al., 2009b; Fitzgerald et al., 2009). However, the object was found in follow-up observations in 2009 (Lagrange et al., 2010), appearing on the opposite side of the host star from its initial 2003 observations. Until 2013, no confirmed observations of β Pic b were published with any other instrument besides NaCo and the Near-Infrared Imager and Spectrograph located on the Very Large Telescope (VLT) (Boccaletti et al., 2013). As more instruments have come online, and the object has moved further from its host star making it easier to detect, β Pic b has been detected by VLT/NACO (Lagrange et al., 2010), Gemini/NICI (Boccaletti et al., 2013), Magellan AO

(Morzinski et al., 2014), and Gemini/GPI (Macintosh et al., 2014).

The confirmation that β Pic b is a planet, buried in a well-studied, and prominent debris disk has led to a multi-epoch attempt to understand the orbital parameters of β Pic b, its temperature and atmospheric environment, and to discern if it is part of the main disk or the secondary inclined disk (Lagrange et al., 2012; Currie et al., 2011). Measurements of the position of β Pic b determined it to have an ~ 9.04 AU semi-major axis, with a $20^{+2.9}_{-1.4}$ year orbital period at a 90.60 ± 0.68 degree inclination (Macintosh et al., 2014) on the sky. SED fitting of broad band photometry has been performed on β Pic b to estimate an effective temperature of $1700 \pm 100K$, with a $\log g = 4.0 \pm 0.5$, and that β Pic b has a dusty atmosphere (Bonnefoy et al., 2013). Bonnefoy et al. (2013) finds that "hot-start" evolutionary models give a mass estimate of 10^{+3}_{-2} $\mathrm{M_{Jup}}$ and a mass of 9^{+3}_{-2} $\mathrm{M_{Jup}}$ from luminosity measurements.

Studying the orbit of β Pic b will allow us to reconcile the past three decades of observations of the disk, with a planet that is orbiting and sculpting that disk. Observations by the NACO team (Chauvin et al., 2012) are valuable in that they have the benefit of being performed with the same instrument, and over a long baseline to further constrain the orbit. They found that the planet is aligned with the inner warped disk, and that the planet is located above the mid-plane of the main disk. They also found that the position is compatible with a warped disk tilted by 3.5–4.0 degrees. This is in contrast to Currie et al. (2011) who in reanalyzing the data with his own version of LOCI argued that the observations are inconsistent with the inner disk position angle, which is offset by ~ 5 deg. GPI observations made in late 2013 are seen to have a position angle above the main disk, tilted by 2.8 ± 0.6 degrees with respect to the main disk, providing additional evidence that the planet is clearly misaligned with the main disk, but more nearly aligned with the inner warped disk (Macintosh et al., 2014). Observations over time, have given a sense of the orbital period and semi-major axis. Chauvin et al.

(2012) found the most probable range for the semi-major axis fell between 8.0 – 9.0 AU. GPI, using previous published NACO measurements, further constrains the semi-major axis to being $9.04^{+0.82}_{-0.41}$, having most likely observed β Pic b after having reached its maximum projected angular separation.

Starting in 2009 we attempted to observe the β Pic system in L′ using the Near Infra-Red Camera 2 on Keck. These observations are broad band. When this campaign was started, no other instruments besides NACO had published observations of β Pic b. While β Pic is only visible for part of the year from Mauna Kea, when it is up, it reaches a low altitude, and a high airmass. We present the work done from Keck using observations from 2009 and 2012 using the classical LOCI process. These observations provide a large baseline to compute the orbit of β Pic b.

4.2 A review of ADI, LOCI, & SDI

The primary problem with directly imaging planets is that the point spread function (PSF) of the star contains significant flux to much larger radii than the planet location. This PSF is not stable over long time scales such that it is easily subtracted by building a master reference PSF. This complication is described in more detail in section 1.2. Several techniques such as angular differential imaging (ADI), locally optimized combination of images (LOCI), and spectral differential imaging (SDI) have been employed to try and build reference PSFs. These techniques rely on using frames close in time or spectral coverage as the science frame of interest in order to estimate the PSF of the telescope and instrument and subtract it from the science frames. In order to suppress the PSF from β Pic A which obscures the image of β Pic b (Figures 4.2,4.3) we employ these techniques. We review the mathematics behind these algorithms below in sections 4.2.1,**??**,4.2.2.

4.2.1 Angular Differential Imaging

ADI exploits the fact that the sky and the pupil can be rotated with respect to each other allowing the observations of the pupil and PSF to be disentailed from the objects in the sky. A simple form of ADI (Marois et al., 2005b; Liu, 2004) takes a median of several images close in time, but where the pupil PSF pattern is stabilized on the detector and a companion rotates throughout the observing sequence due to field rotation. The subtraction avoids frames where the companion has not been displaced to avoid subtraction with itself. ADI can be summarized by the set of equations in Marois et al. (2006):

Given a set of images (I_n) taken at a given time (t_n) at a paralactic angle (θ_n):

$$I_1(t_1, \theta_1), I_2(t_2, \theta_2), I_3(t_3, \theta_3), \ldots, I_n(t_n, \theta_n) \tag{4.1}$$

the first goal is to remove the constant PSF component.

$$I_i^D = I_i - \text{median}(I_1, I_2, I_3, \ldots, I_n) \tag{4.2}$$

To remove the slowly varying time component, an optimized reference PSF is then obtained for each image by median combining four images (two images acquired before and two images after the image being processed) that show at least 1.5 full-width-at-half-max of rotation separation at a given radius of interest.

$$I_i^{ADI} = I_i^D - a \times \text{median}(I_{i-b}^D, I_{i-b-1}^D, I_{i+c}^D, I_{i+c+1}^D) \tag{4.3}$$

Having subtracted a significant portion of the constant, and slowly varying PSF components, the more rapidly varying components are suppressed by rotating the PSF so that the paralactic angle of rotation for each image is aligned, and the images median combined.

$$I_F^{ADI} = \text{median}\left[I_1^{ADI}, rot(I_2^{ADI}, \Delta\theta_{1-2}), rot(I_3^{ADI}, \Delta\theta_{1-3}), \ldots, rot(I_n^{ADI}, \Delta\theta_{1-n})\right] \tag{4.4}$$

Locally Optimized Combination of Images (LOCI) (Lafrenière et al., 2007) is a similar process to the simple ADI process above, but instead of choosing just the nearest set of images, with enough field rotation, a least-squares fit of the all the images is used, while looking in a sub-region. This process builds a unique reference PSF for each image, in an attempt to subtract the PSF from each individual image. This provides a gain in sensitivity of up to a factor of three at small separations over ADI (Lafrenière et al., 2007; Soummer et al., 2012).

LOCI can be summarized by the set of equations in Lafrenière et al. (2007): Since the subtraction region is based upon sub-regions of the image, we must define an area (A) over which that subtraction occurs. This is determined by W, the full-width-at-half-maximum (FWHM) of the PSF and N_A thus corresponds to the number of "PSF cores" that fit in the optimization subsection.

$$A = N_A\, \pi \left(\frac{W}{2}\right)^2 \tag{4.5}$$

It is necessary for the optimized PSF to be subtracted from a given subsection S^T by using only the subset of these images in which a companion point source appearing in S^T would be displaced such as to not interfere point source in the image being optimized over.

$$K = \{k \in [1, N]\ :\ |\mathbf{r}_k - \mathbf{r}_T| > \delta_{\min{}in}\ \vee\ f_k/f_T < \alpha\}, \tag{4.6}$$

The reference PSF for the optimization subsection is then constructed according to:

$$O^R = \sum_{k \in K} c^k O^k, \tag{4.7}$$

The minimum of σ^2 occurs when all its partial derivatives with respect to the coefficients c^k are equal to zero:

$$\frac{\partial \sigma^2}{\partial c^j} = \sum_i -2 m_i O_i^j \left(O_i^T - \sum_k c^k O_i^k \right) = 0, \quad \forall\, j \in K. \tag{4.8}$$

Reversing the summation order and rearranging the terms:

$$\sum_k c^k \left(\sum_i m_i O_i^j O_i^k \right) = \sum_i m_i O_i^j O_i^T, \quad \forall\, j \in K. \tag{4.9}$$

This is a system of linear equations:

$$A_{jk} = \sum_i m_i O_i^j O_i^k, \qquad x_k = c^k, \qquad b_j = \sum_i m_i O_i^j O_i^T. \tag{4.10}$$

Solving this system gives the coefficients c^k needed to construct the optimized reference PSF image for the subsection S^T. Using the set of optimized coefficients, the optimized reference PSF image subsection to be subtracted from S^T:

$$S^R = \sum_{k \in K} c^k S^k, \tag{4.11}$$

where S^k denotes the corresponding subtraction subsection in the reference PSF image k.

4.2.2 Spectral Differential Imaging

SDI is a technique where the PSF is built by acquiring images simultaneously at adjacent wavelengths. Because the location of a speckle is dependent on wavelength, taking simultaneous images at multiple wavelengths, with either an IFS (McElwain et al., 2007) or a dual-channel camera, can allow for the subtraction by building a PSF from other wavelengths. This is often done by rescaling the images so that the PSF will be fixed, but the planet will change position with wavelength (Figure: 4.1). Just as for ADI, this allows the PSF to be subtracted by combining the different measurements of the PSF with methods similar to those discussed in section 4.2.1. The images can then be combined to locate the companion. A lenslet based integral field spectrograph (IFS) has the advantage of sampling the focal plane before the spectrum is separated. Additionally, SDI does not suffer from the need to have the sky rotate but instead builds the PSF from the diffraction effects which cause the location of a given diffraction effect, resulting from a flaw in the optics, to change the position it falls on the focal plane depending upon the observed wavelength.

4.3 Observations and Data Reduction

We observed β Pic (HD 39060) on 24 November 2009 and 12 October 2012 using the Near Infra-Red Camera 2 (NIRC2) located behind the adaptive optics bench on the Left Nasmyth Platform of Keck II. All observations were performed with imaging mode in L$'$ (3.43 – 4.12μm) using the narrow camera field of view (10x10 arcsec) with a plate scale of 0.9942 ± 0.005 milliarcseconds/pixel. NIRC2 was put into vertical angle mode which fixes the telescope orientation to the instrument, but allows the sky to rotate with time. Thus the orientation of the PSF will stay fixed frame-to-frame but the planet will rotate in position angle around the central star. The 2009 data were taken without a chronographic spot, with the core of the PSF from β Pic A saturated, and sky frames interleaved with the observations. NIRC2 was used in a subarray mode, with only the central 512×512 pixel region ($\sim$ 5 square arcseconds) imaged. The data was taken in MCDS-2 mode with an exposure time of 0.5 seconds. β Pic underwent 21.5 degrees of sky rotation during this image set, and had an air-mass ~ 3. Immediately after the observations, a reference image of the star FS13 (selected from Leggett et al. (2003) standards catalog) was taken for photometric and core PSF generation.

The 2012 data were taken with the 200 milliarcsecond coronagraphic spot. The images were taken both behind the spot, and with the central star dithered in a three position pattern to avoid the bad quadrant on NIRC2. In lieu of taking sky frames, this dither pattern was used to generate sky frames for subtraction. The entire 1024×1024 chip was used for the 2012 observations. Exposure times were 0.18 seconds, 30 co-adds, taken in CDS mode.

For the 2012 data, β Pic was taken at an air-mass of ~ 3 and underwent 14.1 degrees of sky rotation during the entire image set, but the dither pattern data is bracketed by the under frames where the central star is located under the occulting spot and thus only underwent 9.4 degrees of sky rotation. This limited sky rotation does not allow the planet to be completely identified for positional information, and is instead cut off. For this reason, we only analyzed the on spot data, having significantly more sky rotation. For 2012 a reference image of the star FS13 and FS2 were taken for photometric and core PSF generation (selected from Leggett et al. (2003) standards catalog).

We separated the observational data sets by category: where the observations under the occulting spot are analyzed separately from the images taken as part of a dither pattern. With the addition of the 2009 data, there were three data sets, which were each analyzed using the same procedures. To align the images, we used a cross correlation, over a localized area. This localized area was defined such as to avoid regions of known detector or non-linear PSF effects. Additionally, regions far away from the PSF structure were avoided. This left only the central part of the PSF which in which the signal was dominated by the PSF to align the position of the central star and PSF between individual frames. We attempted to cross correlate unsaturated images of β Pic A with the entire data set to determine the location of the central star but were unsuccessful because the PSF wings were dominated by sky background noise and read noise. This made it difficult to determine the location of the central star. In order to determine the location of the central star we used the known sky rotation to forward model the location of the planet.

In order to identify the location of the planet and its flux, we attempted to forward model the solution with a five parameter fit consisting of the X-location of the central star (1), The Y-location of the central star (2), the radius of the planet from the central star (3), the position angle of the planet (4), and the flux of the planet (5). Using the time stamp recorded with each observation, we determined the position angle, and the location of β Pic A to calculate the sky rotation. Using this information and an estimate of the location of β Pic b, we attempted to subtract the planet from each frame using the reference PSF. Each image then is radial profile subtracted (the average flux at a given radius from the central star is subtracted), to remove halo effects, and then LOCI (Lafrenière et al., 2007) is used to subtract the remaining PSF. A Levenberg-Marquardt least-squares minimization (Markwardt, 2009) attempts to minimize the residuals after LOCI of the planet subtraction by adjusting the parameters of the injected PSF. The returned solution is the location and flux of the reference PSF which best subtracts the planet from the frame leaving the lowest residuals behind. We interpret this best subtraction solution as the location of β Pic A and b. Finally, the NIRC2 header coordinates have a known adjustment with respect to north. We use the measurement of 0.252 degrees in Yelda et al. (2010) to correct our PA.

We estimated the use of LOCI parameters by applying several different parameterizations and solving for the least squares fit in each case. The resulting points are then averaged together, where the averages are weighted by the Chi-squared. We estimated the errors by injecting several artificial points into the data set at various paratactic angles, but at the same angular separation as was estimated for the planet. We used this to estimate an error in our fitting routine by calculating the standard deviation of the fitted result errors from the original known PSF inject location. This is added in quadrature to the error that results from the covariance matrix as part of the Levenberg-Marquardt least-squares minimization.

4.4 Results

For 24 November 2009 (Figures 4.2,4.4), we find that the angular separation is 312.8 ± 18.3 milliarcseconds with a parallactic angle of 211.36 ± 2.29. For 12 October 2012 (Figures 4.3,4.5), we find that the angular separation is 466.35 ± 8.4 milliarcseconds with a parallactic angle of 212.0 ± 0.7 degrees.

Our 2009 measurements were taken while β Pic b was significantly closer to its host star than in 2012, making the measurements more difficult and requiring a significant amount of sky rotation. On Nov 24, 2009, we found that the separation was 312.8 ± 18.3 milliarcseconds. On September 25, 2009, observations using NACO found that the separation was 299 ± 14 milliarcseconds, and on December 29, 2009 306 ± 09 milliarcseconds (Chauvin et al., 2012). We find that our location for β Pic agrees to within error bars of these measurements.

Our 2012 measurements were taken while β Pic b was nearing its largest separation (as view from Earth) from β Pic A. We found a projected separation of 466.35 ± 8.4 milliarcseconds. This in good agreement with Magellan/MagAO measurements of 461 ± 14 milliarcseconds made on December 02, 2012 (Nielsen et al., 2014), and with current orbital parameters from Macintosh et al. (2014).

Observations by the NACO team (Chauvin et al., 2012) have shown that the inclination of the orbit of the planet is misaligned with the main disk and is more aligned with the inner warped disk. Independent analysis by Currie et al.

(2011) who in reanalyzing the data with his own version of LOCI argues that the position of the planet is inconsistent with the inner disk position angle and that the planet is not aligned with the inner warped disk. GPI observations have indicated that the inclination of the orbit of the planet is not consistent with the aligned disk, but more with the misaligned disk, though slightly less at an inclination 2.8 ± 0.6 degrees versus the 3.5–4.0 degrees as found with NACO. Our observations conclude that the planet is misaligned with the main disk with a PA$= 211.9 \pm 0.4$ degrees, making the planet misaligned by 2.9 ± 0.5 degrees above the main disk. This measurement is slightly less than the NACO measurements, but still confirms it presence above the disk, and is in excellent agreement with the GPI measurements presented in Macintosh et al. (2014).

4.5 Discussion

Our observations confirm the planet β Pic b in L′-band observations from Keck observatory. These observations were the first made from the northern hemisphere and are taken at a high airmass. These results agree well with the published literature, and provide two distinct locational estimates for the planet using the extremely well characterized NIRC2 instrument. The orbital separation of ∼9 AU agrees well with the picture that a giant planet is enforcing the inner belts of the β Pic system and provide a possible perturber to misalign the inner disk of β Pic. The next generation of extreme AO systems dedicated to observing extra solar planets will allow even more detailed and precise astrometric measurements of this system thus enabling the planet to be followed far closer to its parent star than these 2009 and 2012 observations were capable of.

4.6 Summary

The β Pic system has been the focus of intense study for the past three decades. It has long been speculated that the massive debris disk that surrounds this star, has hidden an extrasolar planet. Despite much speculation, and many supporting observations, only in the last five years has one actually been confirmed to exist. We have made follow-up observations in the L′-band of this system on the extremely well characterized NIRC II instrument located on Keck II. Our observations allow a comparison across a three-year baseline, and were taken at the same time as some of the closest observations to the central star, and near the furthest separation from the central star, providing a good lever arm to add to the current set of published observations. We find that our locations are consistent with the VLT/NACO, Magellan/MagAO, Gemini/NICI, and Gemini/GPI observations. Further, we find that the planet appears to be inclined with respect to the disk, and is not part of the main disk.

GEMINI South/GPI and VLT/SPHERE will continue to make key contributions to our understanding of the atmosphere of β Pic b. SPHERE and GPI will allow us to measure the planetary positions much more precisely than have been previously achievable, and will provide for much more detailed analysis of their atmosphere through the inclusion of integral field spectrographs. The work of the next generation of direct imagers will allow for an investigation of the orbital path closer to the central star than other instruments had been previously capable of.

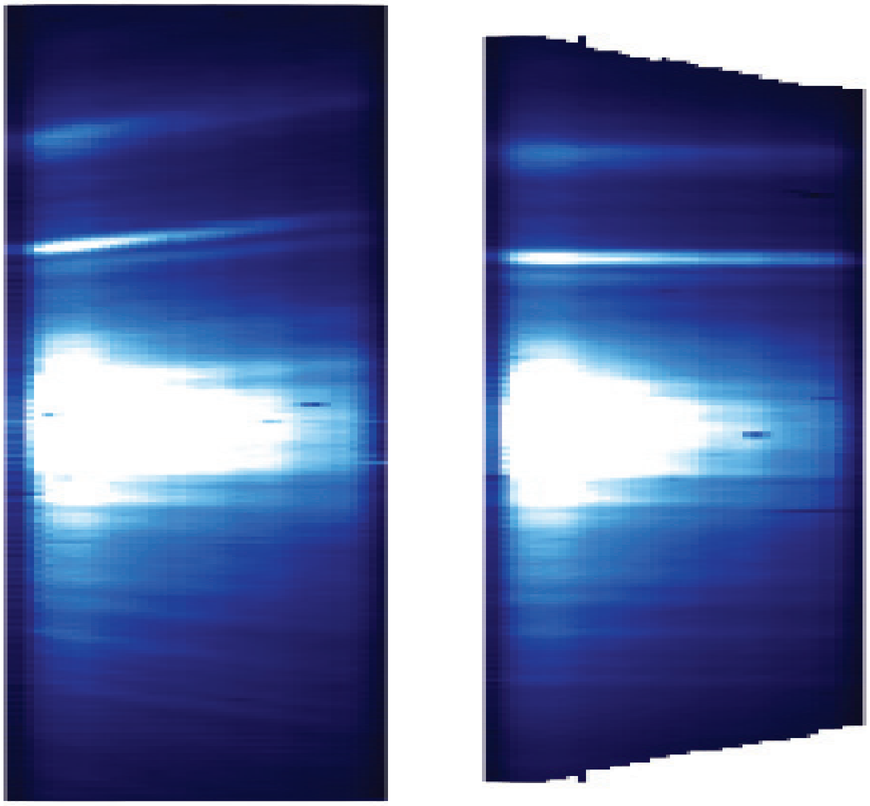

Figure 4.1: Cuts through a GPI data cube with one spatial and one spectral dimension. In the original cube (left), the diffraction artifacts diverge outward with wavelength (X-axis), while in the spatially resampled cube (right), they form straight lines running vertically in the plot and showing only low-frequency structures. This image is from GPI in H-band.

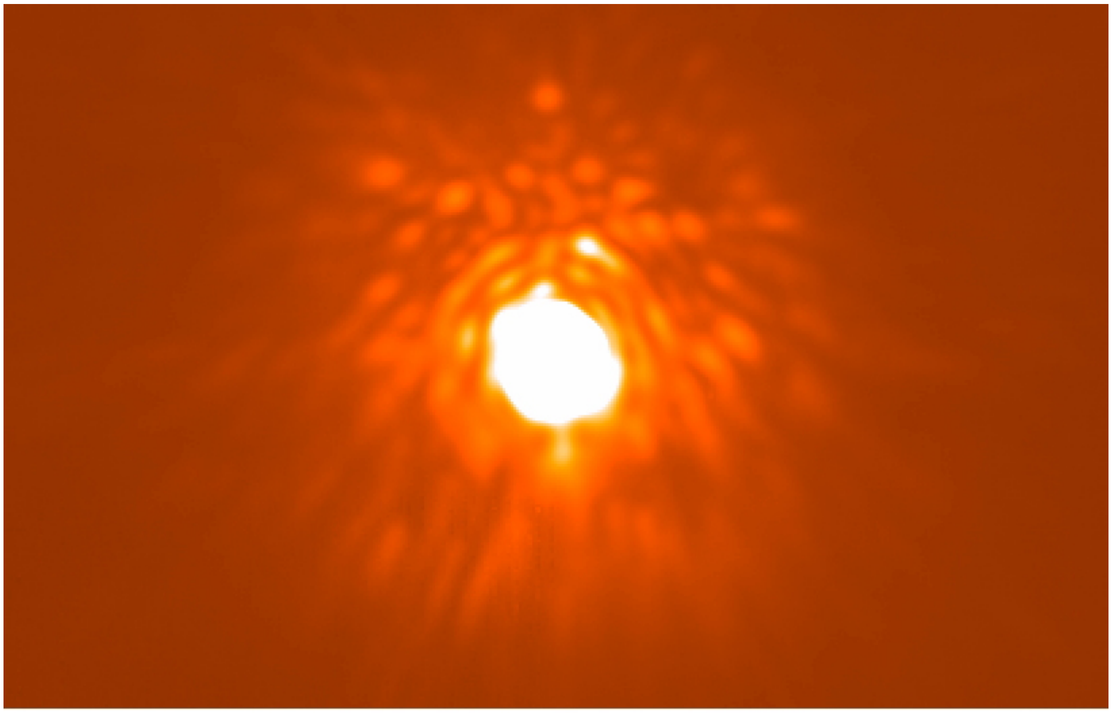

Figure 4.2: A 2009 median stacked image of β Pic b without any processing.

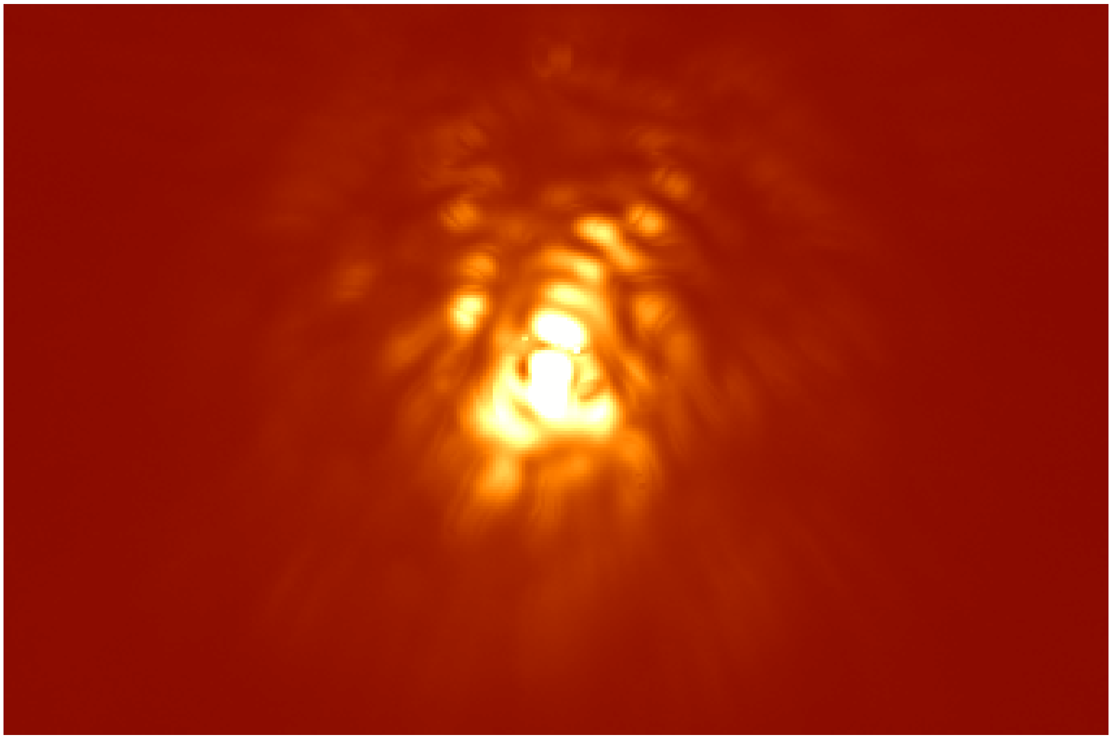

Figure 4.3: A 2012 median stacked image of β Pic b without any processing.

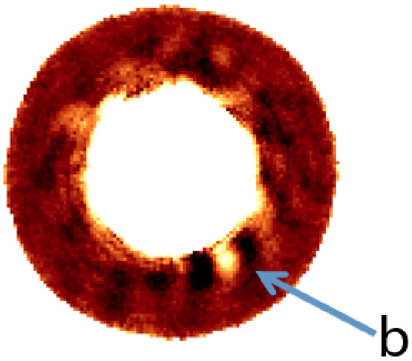

Figure 4.4: A 2009 median stacked image of β Pic b after processing with LOCI. The ring is defined as a set of subregions over which LOCI has processed the image, where areas farther away from the center are not processed due to the time required for many iterations.

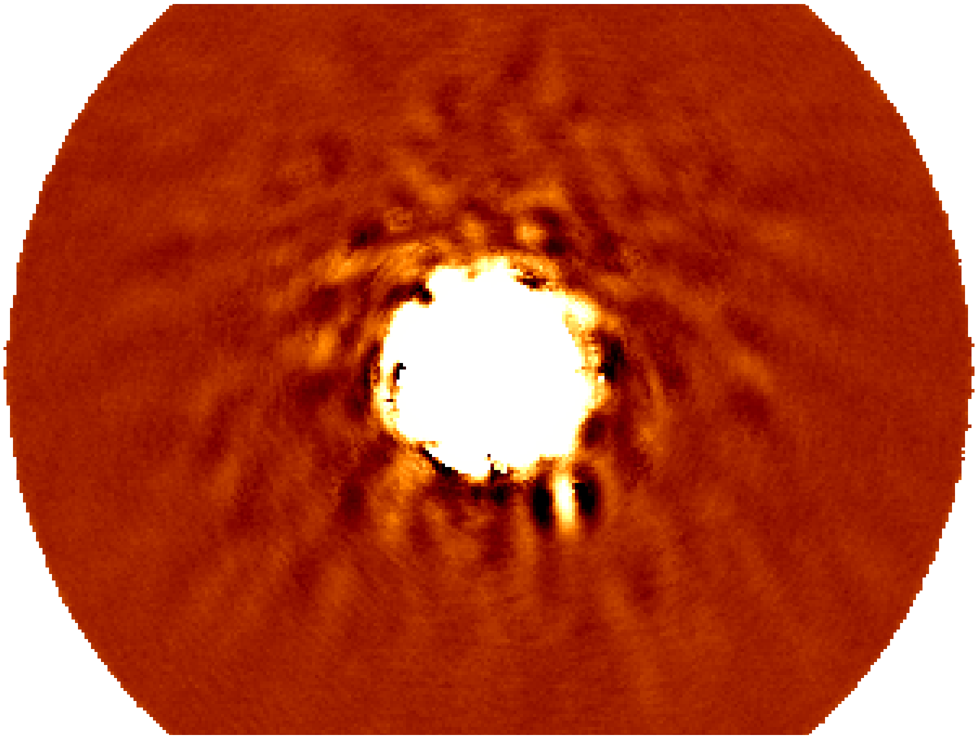

Figure 4.5: A 2012 median stacked image of β Pic b after processing with LOCI. The ring is defined as a set of subregions over which LOCI has processed the image, where areas farther away from the center are not processed due to the time required for many iterations.

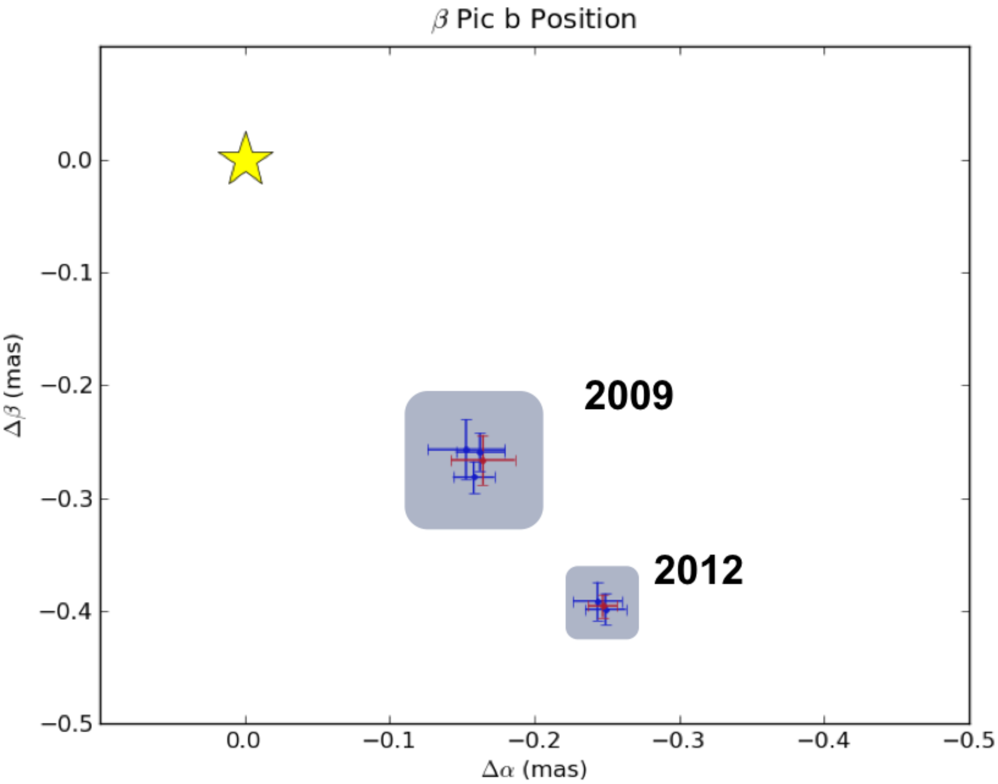

Figure 4.6: The positions of β Pic b as observed from Keck (Red) vs other observations taken at approximately the same time (2009: NICI & NACO, 2012: NICI & Magellan) (Chauvin et al., 2012; Nielsen et al., 2014).

CHAPTER 5

The First H-band Spectrum of the Massive Gas Giant Planet beta Pictoris b

Submitted to the Astrophysical Journal Letters, 2014 July 15

5.1 Introduction

For over a decade, there have been ongoing efforts to directly image young Jupiter mass exoplanets still luminous in the infrared (IR) from their formation process. Examples of such planets include 2M1207b (Chauvin et al., 2005), Fomalhaut b (Kalas et al., 2008), the HR8799 system (Marois et al., 2008, 2010), β Pic b (Lagrange et al., 2010), IRXS J1609 b (Lafrenière et al., 2010), HD 95086 b (Rameau et al., 2013), and GJ 504 b (Kuzuhara et al., 2013).

Beta Pictoris (HD 39060) is an A6V star located 19.44 ± 0.05 pc from Earth (Gray et al., 2006; van Leeuwen, 2007). Zuckerman et al. (2001) estimates the age of β Pic at 12^{+8}_{-4} Myr, but that has recently been revised upwards to 21 ± 4 Myr (Binks & Jefferies 2014). β Pic represents the earliest examples of using high contrast imaging to directly detect a circumstellar disk (Smith & Terrile 1984). The disk is seen edge-on and shows asymmetric structure that has been attributed to planetary perturbations (Burrows et al., 1995; Kalas & Jewitt, 1995; Golimowski et al., 2006; Mouillet et al., 1997; Heap et al., 2000). The planet possibly responsible for these perturbations was eventually discovered by direct imaging (Lagrange et al., 2010). β Pic b has been detected by VLT/NACO (Lagrange et al., 2010), Gemini/NICI (Boccaletti et al., 2013), Magellan AO

(Males et al., 2014; Morzinski et al., 2014), and Gemini/GPI (Macintosh et al., 2014). This has led to a multi-epoch attempt to understand the planet's orbital parameters and to discern if it is aligned with the main disk or the secondary inclined disk (Lagrange et al., 2012; Chauvin et al., 2012; Macintosh et al., 2014). The basic properties of β Pic b have been estimated using SED fitting of broad band photometry, resulting in an effective temperature of $1700 \pm 100K$, with a $\log g = 4.0 \pm 0.5$(Bonnefoy et al., 2013). Previous comparisons of the planet's bolometric luminosity and system age to evolutionary cooling tracks resulted in a mass from 9 to 13 $\mathrm{M_{Jup}}$ (Bonnefoy et al., 2013; Males et al., 2014). Using a cross-correlation technique and high-spectral resolution over a narrow wavelength range, Snellen et al. (2014) were able to measure the planet's spin ($vsin(i) \sim 25$ km/s) and detect carbon monoxide absorption in the K band.

Understanding the atmospheres of these very young giant exoplanets is a challenging task because we have only a handful of objects to study spectroscopically. The theoretical models used to compute the emergent flux from these planetary atmospheres are often extensions of those generated for brown dwarfs, yet the spectra of the HR8799 planets exhibit significant differences relative to brown dwarfs (Barman et al., 2011a; Marley et al., 2012). Spectroscopy of β Pic b offers another opportunity to study the atmospheric properties of a young giant planet that is substantially hotter than the HR8799 planets.

Here we present the first H-band spectral mode observations of β Pic b with GPI. An analysis of the orbital parameters using astrometric measurements from these data has been published in Macintosh et al. (2014). In section 5.2, we briefly review the recently delivered Gemini Planet Imager being commissioned on the Gemini South telescope. In section 5.3, we discuss the observations and data reduction used to analyze the spectrum with this new instrument. Analysis of the H-band spectrum, along with existing photometry, is presented in section 5.4. Conclusions are discussed in Section 5.5.

5.2 Gemini Planet Imager

The Gemini Planet Imager is a facility class instrument that was designed and built to directly image and spectroscopically characterize young, Jupiter sized, self-luminous extrasolar planets. GPI was built for the Gemini Observatory, and installed at Gemini South in the fall of 2013. The high dynamic ranges involved in directly imaging extrasolar planets required GPI to be designed to pay special attention to speckle suppression (Macintosh et al., 2006; Graham et al., 2007).

GPI uses different sub-systems to combine several key technologies into one instrument. The GPI adaptive optics (AO) system incorporates a large number of degrees of freedom and uses a spatially filtered wavefront sensor to enhance contrast near the star. GPI first light and commissioning tests demonstrate that the AO system lowers the total wavefront error from dynamic sources and quasi-static errors by an order of magnitude compared to earlier AO systems (Macintosh et al., 2014). The GPI AO system is composed of a low spatial frequency, high stroke, 11 actuator diameter woofer deformable mirror, and a 64×64 Micro-electro-mechanical-system low stroke, high frequency, deformable mirror from Boston Micromachines (Poyneer et al., 2011), with a 43-actuator-diameter region for high order corrections. Light travels through a spatially-filtered wave-front sensor, to remove high spatial frequency signals that would violate the sampling theorem and be aliased as low-frequency signals. Spatial filtering is implemented as a hard-edged stop in the focal plane before the wavefront sensor (Poyneer & Macintosh, 2003).

Diffraction is suppressed by an apodized-pupil Lyot coronagraph (Soummer et al., 2011; Macintosh et al., 2014).

A grid of narrow, widely-spaced lines printed onto the apodizer forms a two-dimensional grating, producing diffracted images of the central star in a square pattern. These four satallite spots allow for a sampling of the central star spectrum, instrumental, and atmospheric effects in the same image as the object of interest (Wang et al., 2014).

A infrared (IR) calibration wavefront sensor was designed to suppress non-common path wavefront errors (Wallace et al., 2010) by providing feedback about these errors to the AO sytem. Finally, the science instrument is a near-IR (1-2.5 μm) integral field spectrograph (IFS) with an imaging polarimetry mode (Chilcote et al., 2012; Larkin et al., 2014). The spatial field is sampled by a lenslet array and then dispersed, resulting in $\sim$ 37,000 individual spectra with a spectral resolving power R= $\lambda/\delta\lambda \sim 30-90$. The spatial plane is sampled at 14.14 ± 0.01 milliarcseconds per pixel (Konopacky et al., 2014). In first light observations, GPI achieved a 5-σ contrast of 10^5 at 0.35 arcseconds and 10^6 at 0.75 arcseconds (Macintosh et al., 2014).

5.3 Observations and Data Reduction

β Pic was observed with GPI in the H band (1.5072μm - 1.7899μm[1], R ~44-49) by the GPI Verification and Commissioning team on Gemini South during first light and then during the first verification and commissioning runs on 18 November 2013 and 10 December 2013, respectively. During the November observations, 32 individual 59.6-second images were obtained in coronagraphic mode, with the cryocoolers (Chilcote et al., 2012; Larkin et al., 2014) operating at a reduced power level to reduce the effects of vibration introduced into the telescope. Seeing conditions were on average $0.68''$as measured by the Gemini South DIMM. As the observations were performed during instrument commissioning, various operational modes were used during a specific data set to evaluate performance of the instrument. During the December 2013 observations, 14 individual 59.6-second images were obtained in coronagraphic mode. For eight of the images,

---

[1] Defined by the 80% power-point of the filters

the IFS cryocoolers were operating at full power, while in the remaining six images, the cryocoolers were operating in a reduced power state similar to the November observations. Each image has a different spatial filter size & woofer integrator memory value in an attempt to optimize AO performance (Macintosh et al., 2014). Immediately after the observing sequence was completed, and at the same telescope orientation and flexure, a single observation of the flood illuminated argon calibration source was taken to accurately track the shift of the spectral solution on the HAWAII-2RG detector.

The images were first processed using the GPI data reduction pipeline (Perrin et al., 2014). The pipeline requires the location and spectral solution for every lenslet. These lenslet locations were determined by using a cross correlation of the single argon image taken during the observing sequence as β Pic and high S/N, deep images made during daytime calibrations. The telescope elevation differed between the science images and the daytime calibration sequence. The resultant shift was used to determine the overall change of the wavelength solution between the daytime calibrations and that appropriate for the observations of β Pic.

With a shifted wavelength calibration, the GPI data reduction pipeline was used to reduce all images, apply dark corrections, remove bad pixels, track satellite spot locations, and convert each microspectra into a 37-channel spectral cube $(1.490 - 1.802\mu\mathrm{m})$. Each data set was processed in an identical way.

Further data processing was done outside of the GPI pipeline. The GPI atmospheric dispersion corrector was not commissioned at the time these observations were made; therefore, each image and each spectral slice are independently registered using the stellar position found by the four satellite spots. GPI is mounted on a Cassegrain port with derotator disabled so each image has a different sky orientation. In post processing, these images are rotated so that the planet has a fixed location.

Since the satellite spots are imaged at an identical time under identical conditions, in theory their PSFs should closely match the planet PSF especially when the four spots are averaged together. Instrumental effects and atmospheric effects are estimated from satellite spot spectra. An 8000K, log $g = 4.0$ BT-Nexgen model (Allard et al., 2012) convolved to the resolution of GPI, was used to approximate the A6V stellar spectrum of β Pic A. This allows the instrumental and telluric features under identical conditions to be estimated for the planet spectrum and removed.

We found that the remaining halo in these initial first light images was smooth, and dominated by uncorrected atmospheric halo speckles, rather than quasistatic speckles. In order to remove this halo, we fit a third-order spline surface to an aperture of radius=57.2–114.4 mas centered on the location of the planet, which includes the space around the planet but does not include the planet itself. A PSF, generated by the average of the four satellite spot cores, was scaled and subtracted from the planet position in parallel to the spline fit. This average PSF of the four satellite spots was generated for each particular image and wavelength channel to which it corresponds. This spline surface + reference PSF is generated to subtract the smooth halo and estimate the flux of the PSF. A Levenberg-Marquardt least-squares minimization (Markwardt, 2009) was performed to find the best fit of the underlying halo and the planet PSF in each image and at each spectral channel (Figure 5.1).

We determined the spectrum using the flux of the PSF component of the background subtraction technique of the spline fit + PSF to measure the flux from the injected reference PSF. This produces a measurement of the planet's flux in each spectral channel. Each of the individual spectra measured from the individual frames is independently normalized and combined together (Figure 5.2). To estimate the systematic errors and residuals, PSFs were generated from the satellite spots, injected with a flat spectrum at an identical radius from the host star into the individual frames, and then reduced in an identical manner. Given that this is one of the first extracted spectrum from the new GPI instrument, and that the halo of the star has significant color variation, it is possible that the overall spectral slope has an uncertainty of approximately 10%.

5.4 Results & Discussion

The spectrum discussed above has an SNR (per wavelength channel) that matches or exceeds most previous broad band photometry. With this spectrum, we can estimate surface gravity and effective temperature as well as search for molecular absorption features and departures from stellar abundances.

The *H*-band spectrum has a clear peak at 1.68 μm defined by absorption on either side. The location of this peak and the slopes on either side are consistent with water absorption frequently seen in brown dwarf spectra. Based on previous photometric estimates of the effective temperature (1600–1700 K), the primary opacity sources across the near-infrared are water, collision-induced absorption (CIA) from H_2, and dust. There is no evidence for additional molecular absorption (e.g., from methane or ammonia). The *H*-band spectrum has a very triangular shape, a hallmark of low surface gravity and further evidence of β Pic b's low mass and youth.

The GPI *H*-band spectrum and existing ground-based photometry were compared to the model grids described in Barman et al. (2011a,b). An effective temperature of 1650±50 K was found to best match these spectral data, in excellent agreement with previous photometric studies (Bonnefoy et al., 2013; Currie et al., 2013; Males et al., 2014). The best matching model is shown in Figure 5.4 and it agrees well with the visible to IR photometry. Broad-band photometric colors, however, are only modestly sensitive to surface gravity, emphasizing the need for spectral data. Our *H*-band spectrum, as previously discussed, has an triangular shape that sensitively depends on surface gravity. Our best matching models have $\log(g) = 4.0 \pm 0.25$ (cgs units) that, when taken into consideration along with the effective temperature of 1650 K, is consistent with evolutionary models between 10 and 20 Myrs for masses between 10 and 12 $M_{\rm Jup}$ (Burrows et al., 1997; Chabrier et al., 2000).

Figure 5.3 compares the December 2013 β Pic b spectrum to those of other directly imaged planetary-mass companions: ROXs 42B b (Bowler et al., 2014), 2M1207B (Patience et al., 2010), HR8799 b (Barman et al., 2011a) and HR8799 c (Oppenheimer et al., 2013). All of these objects are reported to exhibit low gravity. ROXs 42B b has a similar H-band spectrum as β Pic b, though the former has a slightly steeper spectrum on either side of the peak, consistent with ROXs 42B b being slightly younger (5–10 Myr) or lower mass. The other three planets shown in Figure 5.3 are all cooler than β Pic b by $\sim$ 500K to 800K. Despite this large temperature difference, 2M1207b and β Pic b have similar H-band spectra. 2M1207b's H-band spectrum is shaped by a combination of low gravity, opacity from thick dusty clouds, and non-equilibrium chemistry that favors CO over methane (Barman et al., 2011b). Non-equilibrium chemistry is less important in hotter objects like β Pic b that will have large CO/CH_4 ratio, regardless of vertical mixing. Consequently, despite very different temperatures, ROXs 42B b, 2M1207b and β Pic b have atmospheres with similar dominant opacity sources. The H-band similarities between these objects supports the idea that β Pic b is low gravity (and hence low mass) and 1 to 2 pressure scale heights near the photosphere. The differences between β Pic b and HR8799 b and c seen in Figure 5.3 highlight the spectral evolution of low gravity objects from high to low effective temperatures.

The model spectra (Fig. 5.4), however, do not match the H-band spectrum particularly well. The best matching model under predicts the fluxes at $\lambda >$ 1.7 μm while slightly over predicting the fluxes on the blue side of the H-band peak. The net effect is a systematic tilt of 5 to 10% between the model and the data. Though a spectral offset of this magnitude may be present in the data, we found that most *H*-band spectra from a low gravity brown dwarf spectral sequence (Allers & Liu, 2013) agree extremely well with our GPI spectrum. The best matching brown dwarf, 2M2213-21, has a reduced $\chi^2 = 1.7$ (see Fig. 5.4) and the red-optical through *K*-band spectrum of 2M2213-21 also closely follows the β Pic b photometry. Like β Pic b, 2M2213-21 is a young object with low gravity features and is possibly a member of the β Pic moving group, at the $\sim 30\%$ level (Manjavacas et al., 2014). The agreement between the GPI spectrum and that of known low-gravity brown dwarfs strongly suggests that our GPI spectrum is mostly free of chromatic systematic errors and the discrepancies with the synthetic spectra are most likely the result of imperfect modeling (e.g., treatment of dust clouds). Such a systematic discrepancy in the model spectra could bias the derived surface gravity, but it is unclear by how much. Allowing for a slight, ±10% tilt in the model *H*-band spectra yields much improved fits, but does not noticeably change the resulting surface gravity.

5.5 Conclusion

We present the first *H*-band spectrum of the extrasolar planet β Pic b from the recently commissioned Gemini Planet Imager — located on the Gemini South telescope — which began commissioning in the Fall of 2013. The Gemini Planet Imager is a facility class instrument built to directly image and spectroscopically characterize young, Jupiter sized, self-luminous, extrasolar planets. We find that the spectrum of β Pic b provides a new and insightful look at the atmospheres of these high-temperature low-gravity objects. While the best matching model does not perfectly match the *H*-band spectrum, the spectrum is remarkably similar to the young, low gravity brown dwarf 2M2213-21. We thus conclude that error most likely is derived from imperfect modeling of the atmosphere. With so few directly imaged planet spectra, the other known objects are estimated to be cooler than β Pic b, and have a slightly different spectral shape.

Currently, and in the near future, several extreme-AO instruments will be on-line with the capability to directly image the spectra of the extrasolar planets they find. While our β Pic b data only cover the H-band, GPI is designed to measure spectra from $0.95 - 2.4\mu$m at a similar capability as our H-band data. These spectra will further our understanding of these high temperature low-gravity objects. The low resolution but great sensitivity of GPI is well designed to identify and characterize low gravity young exoplanets, as is demonstrated in our β Pic b spectrum.

5.6 Acknowledgements

The authors would like to acknowledge the financial support of the Gemini Observatory, the NSF Center for Adaptive Optics at UC Santa Cruz, the NSF (AST-0909188; AST-1211562, AST-1405505), NASA Origins (NNX11AD21G; NNX10AH31G, NNX14AC21G), the University of California Office of the President (LFRP-118057), and the Dunlap Institute, University of Toronto. Portions of this work were performed under the auspices of the U.S. Department of Energy by Lawrence Livermore National Laboratory under Contract DE-AC52-07NA27344 and under contract with the California Institute of Technology/Jet Propulsion Laboratory funded by NASA through the Sagan Fellowship Program executed by the NASA Exoplanet Science Institute. We are indebted to the international team of engineers and scientists who worked to make GPI a reality.

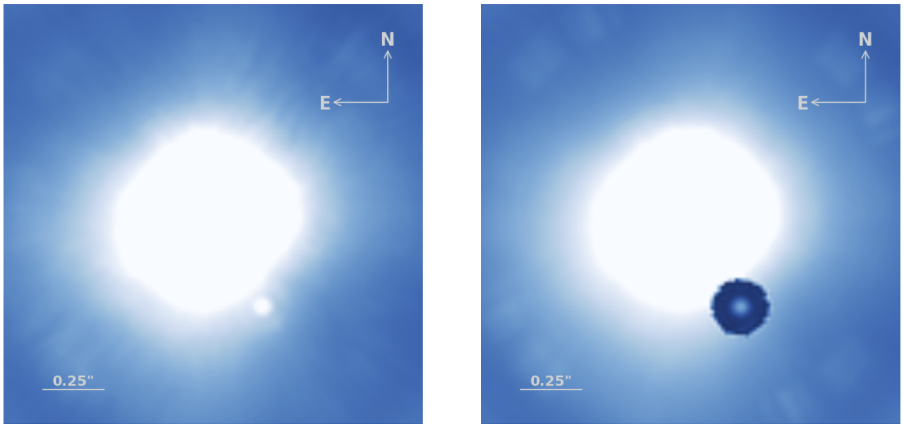

Figure 5.1: *Left:* An average combined set of GPI images of β Pic b from November 2013 with no additional post processing removal of the background. *Right:* An average combined set of images from November with a circular annulus defined around the estimated location of the planet, which has been used to define a surface in each image and spectral channel to subtract the remaining halo light. In order to remove this halo, we fit a third-order spline surface to an aperture of radius=57.2–114.4 mas centered on the location of the planet, which includes the space around the planet but does not include the planet itself. A PSF, generated by the average of the four satellite spot cores, was scaled and subtracted from the planet position in parallel to the spline fit. Images are averaged along the 37 spectral channels in H-band ($\sim 1.5 - 1.8\mu$m).

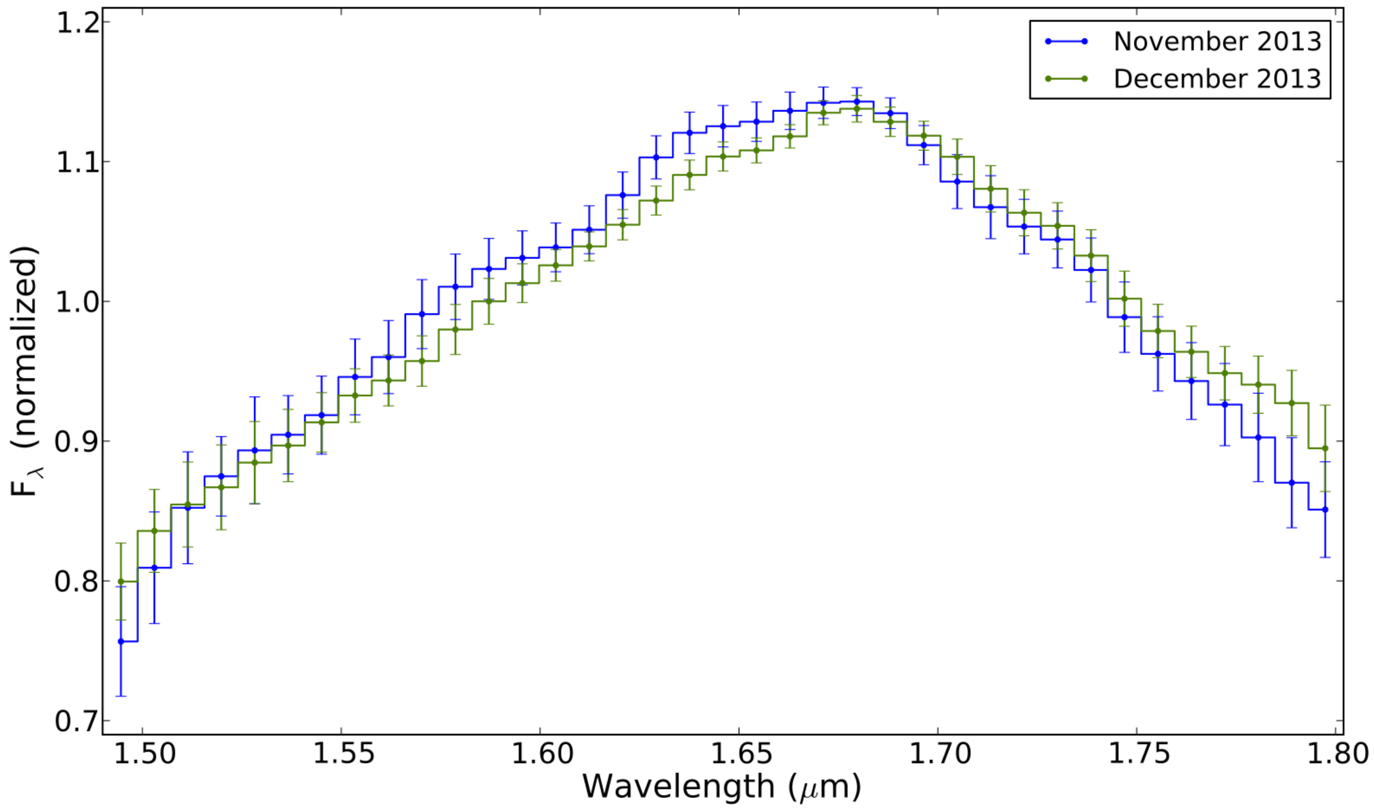

Figure 5.2: H-band spectra of β Pic b using both November and December 2013 observations from GPI. Both spectra are in agreement. The spectra were taken at different phases of the GPI commissioning process resulting in different effects on the light in the halo and PSF shape.

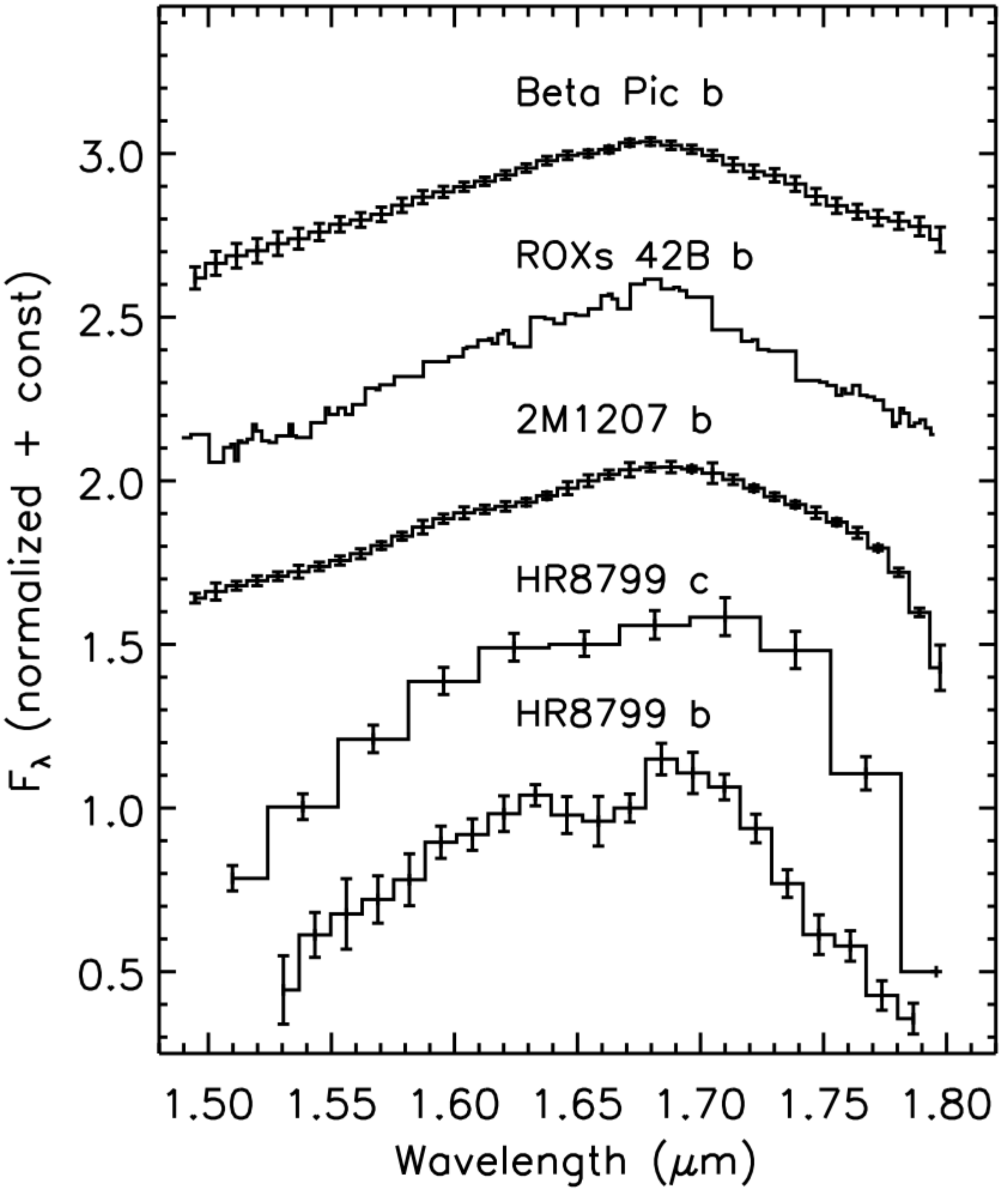

Figure 5.3: *H*-band spectra of young, directly imaged planets. The December 2013 Gemini Planet Imager spectrum of β Pic b is plotted above the spectra of ROX 42b b (Bowler et al., 2014), 2M1207b (Patience et al., 2010), HR8799 c (Oppenheimer et al., 2013) and HR8799 b (Barman et al., 2011a). Each of these objects is cooler than β Pic b. Despite very different temperatures, ROXs 42B b, 2M1207b and β Pic b have atmospheres with similar dominant opacity sources. The differences between β Pic b and HR8799 b and c highlights the spectral evolution of low gravity objects.

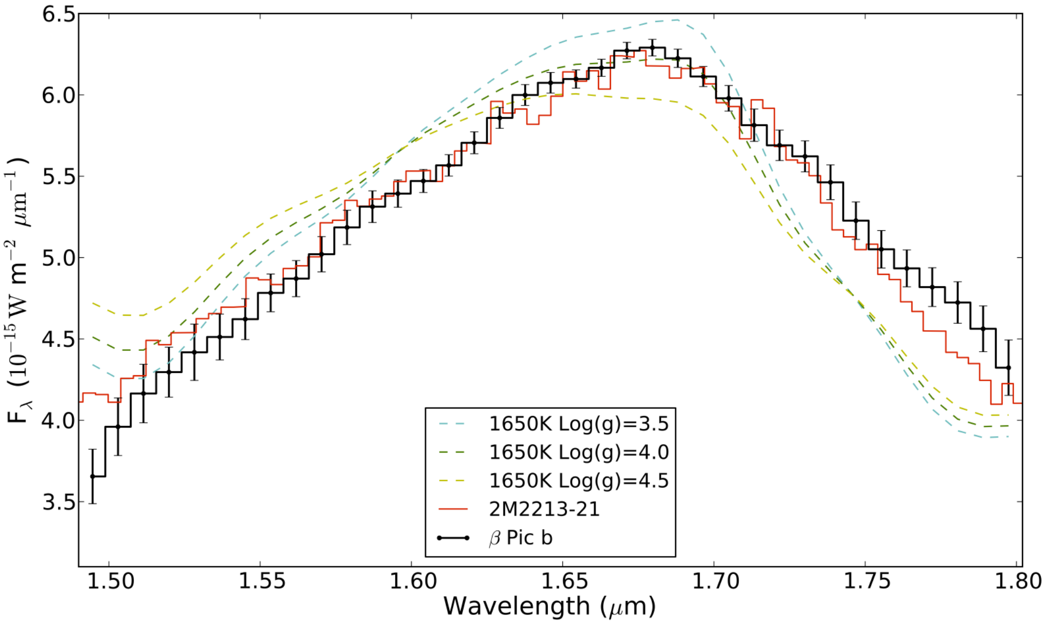

Figure 5.4: The comparison of the H-band spectrum (black) to a 1650K model with 3 different gravities. All three models do not provide a perfect match to the spectrum. The $\log(g) = 4.0$ model (green) comparison has the best fit but is offset from the observations by a constant slope. The young, low-gravity brown dwarf 2M2213-21 (red) has a better match to the spectrum than all 3 models. The agreement between the GPI spectrum and that of known low-gravity brown dwarfs strongly suggests that our GPI spectrum is mostly free of chromatic systematic errors and the discrepancies with the synthetic spectra are most likely the result of imperfect modeling (e.g., treatment of dust clouds). The spectra are normalized to match the flux measured in Males et al. (2014).

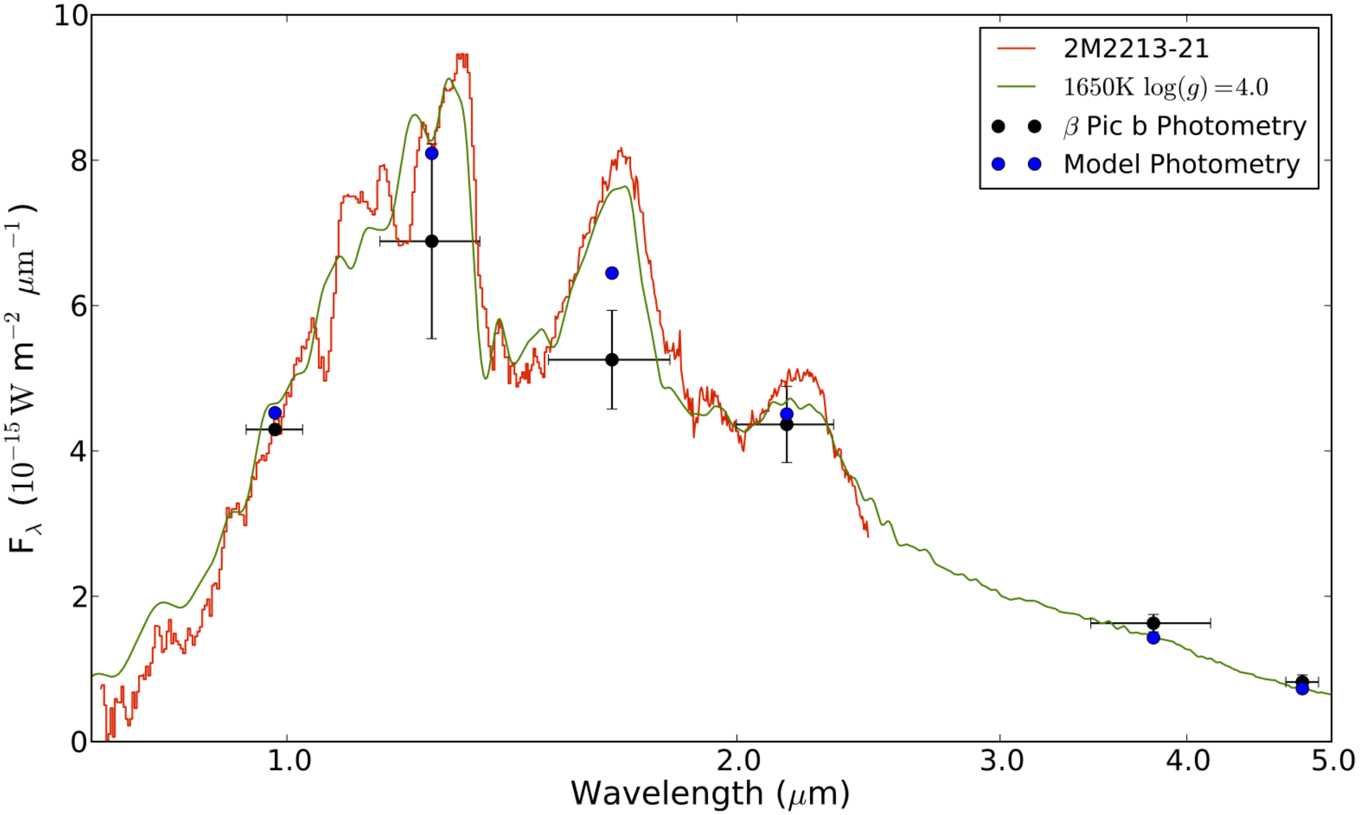

Figure 5.5: We compare the model 1650K $\log(g) = 4.0$ spectrum (green), and its predicted photometric points (blue) to the spectrum of 2M2213-21 (red) and the measured photometric points of β Pic b (black) (Males et al., 2014).

CHAPTER 6

Discussion

In this thesis, I have presented my role in the development of a new planet detection system and its first use to measure the spectrum of the planet β Pic b. Direct detection of extrasolar Jovian planets offers us the best opportunity to discover solar systems like our own and understand the variety of solar systems. But to date, the majority of the extrasolar planets have been found as a result of indirect searches. Only a handful of the known extrasolar planets observed have been detected through direct imaging. The GPI system is the most advanced planet imaging system built to date.

I was part of the team that built the IFS for GPI and that integrated and delivered the GPI system to the Gemini South observatory. GPI's IFS was designed and built at the UCLA Infrared Laboratory. The construction, testing, improvement, and performance characterization of the GPI IFS has been a major component of this work. Our testing has shown that the GPI IFS has excellent optical quality, robust mechanisms, a high level of internal metrology, and excellent filter throughput.

Our preliminary results from November 2013 show that GPI is much more sensitive than existing systems. Observations of β Pic b easily reveled a planet in a single raw 60-second exposure. In comparison to other instruments, a lower signal-to-noise H-band detection using NICI required 3962 s of exposure and extensive PSF subtraction (Macintosh et al., 2014). Beta Pictoris b is detected at a signal-to-noise of ~ 100 in ~ 30 min of imaging.

The science team for GPI has been awarded 890 hours on Gemini South over three years to conduct the GPI Exoplanet Survey (GPIES). The goal of this survey is to observe about 600 stars spanning spectral types A-M. Simulations by McBride et al. (2011) showed that GPI will be capable of detecting 10% of gas giant planets with masses $> 0.5\mathrm{M_{Jup}}$, around stars which are younger than 100 Myr, and closer than 75 parsecs.

Integral field spectrographs have an important role to play in the future of astronomical instrumentation. These types of instruments are rapidly becoming more common and in higher demand. For the future of extrasolar planet finding instruments, IFSs were identified as a science camera for use with the AFTA Coronagraph in the WFIRST-AFTA Final Report (Spergel et al., 2013).

While the IFS and GPI were being constructed and commissioned, I undertook a multi-year set of observations using the NIRC2 camera located on Keck II to directly observe β Pic in L'. Our observations of its orbital inclination strongly support that the planet is elevated above the plane of the main disk. We made observations spanning three years observing β Pic b at the same time as the current closed published observations of the planet, and near the furthest projected angular separation from the central star. These observations agree well with previous observations and orbital solutions.

Using the early commissioning data from GPI we have been able to make the first spectral observations of β Pic b with the Gemini Planet Imager. We presented the first H-band spectrum of the extrasolar planet β Pic b from the recently commissioned Gemini Planet Imager located on Gemini South. The spectrum was found to match the low gravity field brown dwarf 2M2213-21 very well, but had trouble matching models at the 10% level, indicating that at these temperatures and gravities, the models most likely need to be improved. The few planetary objects which have been spectroscopically imaged to date have all shown slightly different atmospheric profiles. Our best matching models have $\log(g) = 4.0 \pm$

0.25 (cgs units) that, when combined with $1650K$, is remarkably consistent with evolutionary models at 20 Myrs (Chabrier et al., 2000) and "hot-start" models.

My thesis work has followed the overall arch of observing the young, self-luminous extrasolar planet β Pic b with current, well characterized, instruments and AO systems, while simultaneously constructing a next generation of instrument with the capability to look at self-luminous extrasolar planets in a detail never before available to the astronomical community. Some of the first objects observed with GPI have been the currently known directly imaginable extrasolar planets, of which β Pic b is one. I have presented the first H-band spectrum analysis of the planet, and the implications it has for the temperature, gravity and metallically of the planet. GPI will make further significant contributions to our understanding of extrasolar planets.

Bibliography

Allard, F., Homeier, D., & Freytag, B. 2012, Royal Society of London Philosophical Transactions Series A, 370, 2765

Allers, K. N. & Liu, M. C. 2013, Astrophysical Journal, 772, 79

Augereau, J. C., Nelson, R. P., Lagrange, A. M., Papaloizou, J. C. B., & Mouillet, D. 2001, Astronomy and Astrophysics, 370, 447

Aumann, H. H. 1984, in Bulletin of the American Astronomical Society, Vol. 16, Bulletin of the American Astronomical Society, 483

Aumann, H. H. & Walker, R. G. 1984, in Bulletin of the American Astronomical Society, Vol. 16, Bulletin of the American Astronomical Society, 689

Bacon, R., Adam, G., Baranne, A., Courtes, G., Dubet, D., Dubois, J. P., Emsellem, E., Ferruit, P., Georgelin, Y., Monnet, G., Pecontal, E., Rousset, A., & Say, F. 1995, , 113, 347

Barman, T. S., Macintosh, B., Konopacky, Q. M., & Marois, C. 2011a, Astrophysical Journal, 733, 65

—. 2011b, Astrophysical Journal, Letters, 735, L39

Batalha, N. M., Rowe, J. F., Bryson, S. T., Barclay, T., Burke, C. J., Caldwell, D. A., Christiansen, J. L., Mullally, F., Thompson, S. E., Brown, T. M., Dupree, A. K., Fabrycky, D. C., Ford, E. B., Fortney, J. J., Gilliland, R. L., Isaacson, H., Latham, D. W., Marcy, G. W., Quinn, S., Ragozzine, D., Shporer, A., Borucki, W. J., Ciardi, D. R., Gautier, III, T. N., Haas, M. R., Jenkins, J. M., Koch, D. G., Lissauer, J. J., Rapin, W., Basri, G. S., Boss, A. P., Buchhave, L. A., Charbonneau, D., Christensen-Dalsgaard, J., Clarke, B. D., Cochran, W. D., Demory, B.-O., Devore, E., Esquerdo, G. A., Everett, M., Fressin, F., Geary,

J. C., Girouard, F. R., Gould, A., Hall, J. R., Holman, M. J., Howard, A. W., Howell, S. B., Ibrahim, K. A., Kinemuchi, K., Kjeldsen, H., Klaus, T. C., Li, J., Lucas, P. W., Morris, R. L., Prsa, A., Quintana, E., Sanderfer, D. T., Sasselov, D., Seader, S. E., Smith, J. C., Steffen, J. H., Still, M., Stumpe, M. C., Tarter, J. C., Tenenbaum, P., Torres, G., Twicken, J. D., Uddin, K., Van Cleve, J., Walkowicz, L., & Welsh, W. F. 2012, ArXiv e-prints

Beuzit, J.-L., Feldt, M., Dohlen, K., Mouillet, D., Puget, P., Wildi, F., Abe, L., Antichi, J., Baruffolo, A., Baudoz, P., Boccaletti, A., Carbillet, M., Charton, J., Claudi, R., Downing, M., Fabron, C., Feautrier, P., Fedrigo, E., Fusco, T., Gach, J.-L., Gratton, R., Henning, T., Hubin, N., Joos, F., Kasper, M., Langlois, M., Lenzen, R., Moutou, C., Pavlov, A., Petit, C., Pragt, J., Rabou, P., Rigal, F., Roelfsema, R., Rousset, G., Saisse, M., Schmid, H.-M., Stadler, E., Thalmann, C., Turatto, M., Udry, S., Vakili, F., & Waters, R. 2008, in Society of Photo-Optical Instrumentation Engineers (SPIE) Conference Series, Vol. 7014, Society of Photo-Optical Instrumentation Engineers (SPIE) Conference Series

Binks, A. S. & Jeffries, R. D. 2014, Monthly Notices of the RAS, 438, L11

Boccaletti, A., Lagrange, A.-M., Bonnefoy, M., Galicher, R., & Chauvin, G. 2013, Astronomy and Astrophysics, 551, L14

Bonnefoy, M., Boccaletti, A., Lagrange, A.-M., Allard, F., Mordasini, C., Beust, H., Chauvin, G., Girard, J. H. V., Homeier, D., Apai, D., Lacour, S., & Rouan, D. 2013, Astronomy and Astrophysics, 555, A107

Bowler, B. P., Liu, M. C., Kraus, A. L., & Mann, A. W. 2014, Astrophysical Journal, 784, 65

Burrows, A., Marley, M., Hubbard, W. B., Sudarsky, D., Sharp, C., Lunine, J. I., Guillot, T., Saumon, D., & Freedman, R. 1997, arXiv.org, astro-ph

Burrows, A., Saumon, D., Guillot, T., Hubbard, W. B., & Lunine, J. I. 1995, Nature, 375, 299

Chabrier, G., Baraffe, I., Allard, F., & Hauschildt, P. 2000, Astrophysical Journal, 542, 464

Charbonneau, D., Brown, T. M., Latham, D. W., & Mayor, M. 2000, Astrophysical Journal, Letters, 529, L45

Chauvin, G., Lagrange, A.-M., Beust, H., Bonnefoy, M., Boccaletti, A., Apai, D., Allard, F., Ehrenreich, D., Girard, J. H. V., Mouillet, D., & Rouan, D. 2012, Astronomy and Astrophysics, 542, A41

Chauvin, G., Lagrange, A.-M., Dumas, C., Zuckerman, B., Mouillet, D., Song, I., Beuzit, J.-L., & Lowrance, P. 2005, Astronomy and Astrophysics, 438, L25

Chilcote, J. K., Larkin, J. E., Maire, J., Perrin, M. D., Fitzgerald, M. P., Doyon, R., Thibault, S., Bauman, B., Macintosh, B. A., Graham, J. R., & Saddlemyer, L. 2012, in Society of Photo-Optical Instrumentation Engineers (SPIE) Conference Series, Vol. 8446, Society of Photo-Optical Instrumentation Engineers (SPIE) Conference Series

Currie, T., Burrows, A., Madhusudhan, N., Fukagawa, M., Girard, J. H., Dawson, R., Murray-Clay, R., Kenyon, S., Kuchner, M., Matsumura, S., Jayawardhana, R., Chambers, J., & Bromley, B. 2013, Astrophysical Journal, 776, 15

Currie, T., Thalmann, C., Matsumura, S., Madhusudhan, N., Burrows, A., & Kuchner, M. 2011, Astrophysical Journal, Letters, 736, L33

Dorn, R. J., Eschbaumer, S., Hall, D. N. B., Finger, G., Mehrgan, L., Meyer, M., & Stegmeier, J. 2008, in Society of Photo-Optical Instrumentation Engineers (SPIE) Conference Series, Vol. 7021, Society of Photo-Optical Instrumentation Engineers (SPIE) Conference Series

Fitzgerald, M. P., Kalas, P. G., & Graham, J. R. 2009, Astrophysical Journal, Letters, 706, L41

Freistetter, F., Krivov, A. V., & Löhne, T. 2007, Astronomy and Astrophysics, 466, 389

Golimowski, D. A., Ardila, D. R., Krist, J. E., Clampin, M., Ford, H. C., Illingworth, G. D., Bartko, F., Benítez, N., Blakeslee, J. P., Bouwens, R. J., Bradley, L. D., Broadhurst, T. J., Brown, R. A., Burrows, C. J., Cheng, E. S., Cross, N. J. G., Demarco, R., Feldman, P. D., Franx, M., Goto, T., Gronwall, C., Hartig, G. F., Holden, B. P., Homeier, N. L., Infante, L., Jee, M. J., Kimble, R. A., Lesser, M. P., Martel, A. R., Mei, S., Menanteau, F., Meurer, G. R., Miley, G. K., Motta, V., Postman, M., Rosati, P., Sirianni, M., Sparks, W. B., Tran, H. D., Tsvetanov, Z. I., White, R. L., Zheng, W., & Zirm, A. W. 2006, Astronomical Journal, 131, 3109

Gorkavyi, N., Heap, S., Ozernoy, L., Taidakova, T., & Mather, J. 2004, in IAU Symposium, Vol. 202, Planetary Systems in the Universe, ed. A. Penny, 331

Graham, J. R. 2009, Available at: http://www.gemini.edu/sciops/instruments/gpi/GPI_OCDD_CDR.pdf

Graham, J. R., Macintosh, B., Doyon, R., Gavel, D., Larkin, J., Levine, M., Oppenheimer, B., Palmer, D., Saddlemyer, L., Sivaramakrishnan, A., Veran, J.-P., & Wallace, K. 2007, ArXiv e-prints

Gray, R. O., Corbally, C. J., Garrison, R. F., McFadden, M. T., Bubar, E. J., McGahee, C. E., O'Donoghue, A. A., & Knox, E. R. 2006, Astronomical Journal, 132, 161

Heap, S. R., Lindler, D. J., Lanz, T. M., Cornett, R. H., Hubeny, I., Maran, S. P., & Woodgate, B. 2000, Astrophysical Journal, 539, 435

Hinkley, S., Oppenheimer, B. R., Soummer, R., Sivaramakrishnan, A., Roberts, Jr., L. C., Kuhn, J., Makidon, R. B., Perrin, M. D., Lloyd, J. P., Kratter, K., & Brenner, D. 2007, Astrophysical Journal, 654, 633

Howard, A. W., Marcy, G. W., Johnson, J. A., Fischer, D. A., Wright, J. T., Isaacson, H., Valenti, J. A., Anderson, J., Lin, D. N. C., & Ida, S. 2010, Science, 330, 653

Kalas, P., Graham, J. R., Chiang, E., Fitzgerald, M. P., Clampin, M., Kite, E. S., Stapelfeldt, K., Marois, C., & Krist, J. 2008, Science, 322, 1345

Kalas, P. & Jewitt, D. 1995, Astronomical Journal, 110, 794

Konopacky, Q. M., Thomas, S. J., Macintosh, B. A., Dillon, D., Sadakuni, N., Maire, J., Fitzgerald, M., Hinkley, S., Kalas, P., Esposito, T., Marois, C., Ingraham, P. J., Marchis, F., Perrin, M. D., Graham, J. R., Wang, J. J., Rosa, R. J. D., Morzinski, K., Pueyo, L., Chilcote, J. K., Larkin, J. E., Fabrycky, D., Goodsell, S. J., Oppenheimer, B., Patience, J., Saddlemeyer, L., & Sivaramakrishnan, A. 2014, in

Kuzuhara, M., Tamura, M., Kudo, T., Janson, M., Kandori, R., Brandt, T. D., Thalmann, C., Spiegel, D., Biller, B., Carson, J., Hori, Y., Suzuki, R., Burrows, A., Henning, T., Turner, E. L., McElwain, M. W., Moro-Martín, A., Suenaga, T., Takahashi, Y. H., Kwon, J., Lucas, P., Abe, L., Brandner, W., Egner, S., Feldt, M., Fujiwara, H., Goto, M., Grady, C. A., Guyon, O., Hashimoto, J., Hayano, Y., Hayashi, M., Hayashi, S. S., Hodapp, K. W., Ishii, M., Iye, M., Knapp, G. R., Matsuo, T., Mayama, S., Miyama, S., Morino, J.-I., Nishikawa, J., Nishimura, T., Kotani, T., Kusakabe, N., Pyo, T.-S., Serabyn, E., Suto, H., Takami, M., Takato, N., Terada, H., Tomono, D., Watanabe, M., Wisniewski, J. P., Yamada, T., Takami, H., & Usuda, T. 2013, Astrophysical Journal, 774, 11

Lafrenière, D., Jayawardhana, R., & van Kerkwijk, M. H. 2010, Astrophysical Journal, 719, 497

Lafrenière, D., Marois, C., Doyon, R., Nadeau, D., & Artigau, É. 2007, Astrophysical Journal, 660, 770

Lagrange, A.-M., Boccaletti, A., Milli, J., Chauvin, G., Bonnefoy, M., Mouillet, D., Augereau, J. C., Girard, J. H., Lacour, S., & Apai, D. 2012, Astronomy and Astrophysics, 542, A40

Lagrange, A.-M., Bonnefoy, M., Chauvin, G., Apai, D., Ehrenreich, D., Boccaletti, A., Gratadour, D., Rouan, D., Mouillet, D., Lacour, S., & Kasper, M. 2010, Science, 329, 57

Lagrange, A.-M., Gratadour, D., Chauvin, G., Fusco, T., Ehrenreich, D., Mouillet, D., Rousset, G., Rouan, D., Allard, F., Gendron, É., Charton, J., Mugnier, L., Rabou, P., Montri, J., & Lacombe, F. 2009a, Astronomy and Astrophysics, 493, L21

Lagrange, A.-M., Kasper, M., Boccaletti, A., Chauvin, G., Gratadour, D., Fusco, T., Ehrenreich, D., Apai, D., Mouillet, D., & Rouan, D. 2009b, , 506, 927

Larkin, J., Barczys, M., Krabbe, A., Adkins, S., Aliado, T., Amico, P., Brims, G., Campbell, R., Canfield, J., Gasaway, T., Honey, A., Iserlohe, C., Johnson, C., Kress, E., LaFreniere, D., Lyke, J., Magnone, K., Magnone, N., McElwain, M., Moon, J., Quirrenbach, A., Skulason, G., Song, I., Spencer, M., Weiss, J., & Wright, S. 2006, in Society of Photo-Optical Instrumentation Engineers (SPIE) Conference Series, Vol. 6269, Society of Photo-Optical Instrumentation Engineers (SPIE) Conference Series

Larkin, J. E., Chilcote, J. K., Aliado, T., Bauman, B. J., Brims, G., Canfield, J. M., Cardwell, A., Dillon, D., Doyon, R., Dunn, J., Fitzgerald, M. P., Graham,

J. R., Goodsell, S., Hartung, M., Hibon, P., Ingraham, P., Johnson, C. A., Kress, E., Konopacky, Q. M., Macintosh, B. A., Magnone, K. G., Maire, J., McLean, I. S., Palmer, D., Perrin, M. D., Quiroz, C., Rantakyr, F., Sadakuni, N., Saddlemyer, L., Serio, A., Thibault, S., Thomas, S. J., Vallee, P., & Weiss, J. L. 2014, in Society of Photo-Optical Instrumentation Engineers (SPIE) Conference Series, Vol. 9147, Society of Photo-Optical Instrumentation Engineers (SPIE) Conference Series

Leggett, S. K., Hawarden, T. G., Currie, M. J., Adamson, A. J., Carroll, T. C., Kerr, T. H., Kuhn, O. P., Seigar, M. S., Varricatt, W. P., & Wold, T. 2003, , 345, 144

Lissauer, J. J., Fabrycky, D. C., Ford, E. B., Borucki, W. J., Fressin, F., Marcy, G. W., Orosz, J. A., Rowe, J. F., Torres, G., Welsh, W. F., Batalha, N. M., Bryson, S. T., Buchhave, L. A., Caldwell, D. A., Carter, J. A., Charbonneau, D., Christiansen, J. L., Cochran, W. D., Desert, J.-M., Dunham, E. W., Fanelli, M. N., Fortney, J. J., Gautier, III, T. N., Geary, J. C., Gilliland, R. L., Haas, M. R., Hall, J. R., Holman, M. J., Koch, D. G., Latham, D. W., Lopez, E., McCauliff, S., Miller, N., Morehead, R. C., Quintana, E. V., Ragozzine, D., Sasselov, D., Short, D. R., & Steffen, J. H. 2011, Nature, 470, 53

Liu, M. C. 2004, Science, 305, 1442

Macintosh, B., Graham, J., Palmer, D., Doyon, R., Gavel, D., Larkin, J., Oppenheimer, B., Saddlemyer, L., Wallace, J. K., Bauman, B., Evans, J., Erikson, D., Morzinski, K., Phillion, D., Poyneer, L., Sivaramakrishnan, A., Soummer, R., Thibault, S., & Veran, J.-P. 2006, in Society of Photo-Optical Instrumentation Engineers (SPIE) Conference Series, Vol. 6272, Society of Photo-Optical Instrumentation Engineers (SPIE) Conference Series

Macintosh, B., Graham, J. R., Ingraham, P., Konopacky, Q., Marois, C., Perrin, M., Poyneer, L., Bauman, B., Barman, T., Burrows, A., Cardwell, A., Chilcote, J., De Rosa, R. J., Dillon, D., Doyon, R., Dunn, J., Erikson, D., Fitzgerald, M., Gavel, D., Goodsell, S., Hartung, M., Hibon, P., Kalas, P. G., Larkin, J., Maire, J., Marchis, F., Marley, M., McBride, J., Millar-Blanchaer, M., Morzinski, K., Norton, A., Oppenheimer, B. R., Palmer, D., Patience, J., Pueyo, L., Rantakyro, F., Sadakuni, N., Saddlemyer, L., Savransky, D., Serio, A., Soummer, R., Sivaramakrishnan, A., Song, I., Thomas, S., Wallace, J. K., Wiktorowicz, S., & Wolff, S. 2014, ArXiv e-prints

Macintosh, B. A., Anthony, A., Atwood, J., Barriga, N., Bauman, B., Caputa, K., Chilcote, J., Dillon, D., Doyon, R., Dunn, J., Gavel, D. T., Galvez, R., Goodsell, S. J., Graham, J. R., Hartung, M., Isaacs, J., Kerley, D., Konopacky, Q., Labrie, K., Larkin, J. E., Maire, J., Marois, C., Millar-Blanchaer, M., Nunez, A., Oppenheimer, B. R., Palmer, D. W., Pazder, J., Perrin, M., Poyneer, L. A., Quirez, C., Rantakyro, F., Reshtov, V., Saddlemyer, L., Sadakuni, N., Savransky, D., Sivaramakrishnan, A., Smith, M., Soummer, R., Thomas, S., Wallace, J. K., Weiss, J., & Wiktorowicz, S. 2012, in Society of Photo-Optical Instrumentation Engineers (SPIE) Conference Series, Vol. 8446, Society of Photo-Optical Instrumentation Engineers (SPIE) Conference Series

Macintosh, B. A., Graham, J. R., Palmer, D. W., Doyon, R., Dunn, J., Gavel, D. T., Larkin, J., Oppenheimer, B., Saddlemyer, L., Sivaramakrishnan, A., Wallace, J. K., Bauman, B., Erickson, D. A., Marois, C., Poyneer, L. A., & Soummer, R. 2008, in Society of Photo-Optical Instrumentation Engineers (SPIE) Conference Series, Vol. 7015, Society of Photo-Optical Instrumentation Engineers (SPIE) Conference Series

Maire, J., Perrin, M. D., Doyon, R., Artigau, E., Dunn, J., Gavel, D. T., Graham, J. R., Lafrenière, D., Larkin, J. E., Lavigne, J.-F., Macintosh, B. A., Marois, C., Oppenheimer, B., Palmer, D. W., Poyneer, L. A., Thibault, S., & Véran, J.-P. 2010, in Society of Photo-Optical Instrumentation Engineers (SPIE) Conference

Series, Vol. 7735, Society of Photo-Optical Instrumentation Engineers (SPIE) Conference Series

Maire, J., Perrin, M. D., Doyon, R., Chilcote, J., Larkin, J. E., Weiss, J. L., Marois, C., Konopacky, Q. M., Millar-Blanchaer, M., Graham, J. R., Dunn, J., Galicher, R., Marchis, F., Wiktorowicz, S. J., Labrie, K., Thomas, S. J., Goodsell, S. J., Rantakyro, F. T., Palmer, D. W., & Macintosh, B. A. 2012, in Society of Photo-Optical Instrumentation Engineers (SPIE) Conference Series, Vol. 8451, Society of Photo-Optical Instrumentation Engineers (SPIE) Conference Series

Males, J. R., Close, L. M., Morzinski, K. M., Wahhaj, Z., Liu, M. C., Skemer, A. J., Kopon, D., Follette, K. B., Puglisi, A., Esposito, S., Riccardi, A., Pinna, E., Xompero, M., Briguglio, R., Biller, B. A., Nielsen, E. L., Hinz, P. M., Rodigas, T. J., Hayward, T. L., Chun, M., Ftaclas, C., Toomey, D. W., & Wu, Y.-L. 2014, Astrophysical Journal, 786, 32

Manjavacas, E., Bonnefoy, M., Schlieder, J. E., Allard, F., Rojo, P., Goldman, B., Chauvin, G., Homeier, D., Lodieu, N., & Henning, T. 2014, Astronomy and Astrophysics, 564, A55

Marcy, G. W. & Butler, R. P. 1996, Astrophysical Journal, Letters, 464, L147

Markwardt, C. B. 2009, in Astronomical Society of the Pacific Conference Series, Vol. 411, Astronomical Data Analysis Software and Systems XVIII, ed. D. A. Bohlender, D. Durand, & P. Dowler, 251

Marley, M. S., Fortney, J. J., Hubickyj, O., Bodenheimer, P., & Lissauer, J. J. 2007, Astrophysical Journal, 655, 541

Marley, M. S., Saumon, D., Cushing, M., Ackerman, A. S., Fortney, J. J., & Freedman, R. 2012, Astrophysical Journal, 754, 135

Marois, C., Doyon, R., Nadeau, D., Racine, R., Riopel, M., Vallée, P., & Lafrenière, D. 2005a, Publications of the ASP, 117, 745

Marois, C., Doyon, R., Racine, R., Nadeau, D., Lafreniere, D., Vallee, P., Riopel, M., & Macintosh, B. 2005b, Journal of the RAS of Canada, 99, 130

Marois, C., Lafrenière, D., Doyon, R., Macintosh, B., & Nadeau, D. 2006, Astrophysical Journal, 641, 556

Marois, C., Macintosh, B., Barman, T., Zuckerman, B., Song, I., Patience, J., Lafrenière, D., & Doyon, R. 2008, Science, 322, 1348

Marois, C., Zuckerman, B., Konopacky, Q. M., Macintosh, B., & Barman, T. 2010, Nature, 468, 1080

Mayor, M. & Queloz, D. 1995, Nature, 378, 355

McBride, J., Graham, J. R., Macintosh, B., Beckwith, S. V. W., Marois, C., Poyneer, L. A., & Wiktorowicz, S. J. 2011, Publications of the ASP, 123, 692

McElwain, M. W., Metchev, S. A., Larkin, J. E., Barczys, M., Iserlohe, C., Krabbe, A., Quirrenbach, A., Weiss, J., & Wright, S. A. 2007, Astrophysical Journal, 656, 505

Morzinski, K. M., Close, L. M., Males, J. R., Hinz, P. M., Puglisi, A., Esposito, S., Riccardi, A., Pinna, E., Xompero, M., Briguglio, R., Follette, K., Kopon, D., Gasho, V., Uomoto, A., Hare, T., Skemer, A., Arcidiacono, C., Quiros-Pacheco, F., Argomedo, J., Busoni, L., Rodigas, T. J., & Wu, Y.-L. 2014, in IAU Symposium, Vol. 299, IAU Symposium, ed. M. Booth, B. C. Matthews, & J. R. Graham, 252–256

Mouillet, D., Larwood, J. D., Papaloizou, J. C. B., & Lagrange, A. M. 1997, Monthly Notices of the RAS, 292, 896

Nielsen, E. L., Liu, M. C., Wahhaj, Z., Biller, B. A., Hayward, T. L., Males, J. R., Close, L. M., Morzinski, K. M., Skemer, A. J., Kuchner, M. J., Chun, M., Ftaclas, C., & Toomey, D. W. 2014, ArXiv e-prints

Offenberg, J. D., Fixsen, D. J., Rauscher, B. J., Forrest, W. J., Hanisch, R. J., Mather, J. C., McKelvey, M. E., McMurray, Jr., R. E., Nieto-Santisteban, M. A., Pipher, J. L., Sengupta, R., & Stockman, H. S. 2001, Publications of the ASP, 113, 240

Okamoto, Y. K., Kataza, H., Honda, M., Yamashita, T., Onaka, T., Watanabe, J.-i., Miyata, T., Sako, S., Fujiyoshi, T., & Sakon, I. 2004, Nature, 431, 660

Oppenheimer, B. R., Baranec, C., Beichman, C., Brenner, D., Burruss, R., Cady, E., Crepp, J. R., Dekany, R., Fergus, R., Hale, D., Hillenbrand, L., Hinkley, S., Hogg, D. W., King, D., Ligon, E. R., Lockhart, T., Nilsson, R., Parry, I. R., Pueyo, L., Rice, E., Roberts, J. E., Roberts, Jr., L. C., Shao, M., Sivaramakrishnan, A., Soummer, R., Truong, T., Vasisht, G., Veicht, A., Vescelus, F., Wallace, J. K., Zhai, C., & Zimmerman, N. 2013, Astrophysical Journal, 768, 24

Oppenheimer, B. R., Beichman, C., Brenner, D., Burruss, R., Cady, E., Crepp, J., Hillenbrand, L., Hinkley, S., Ligon, E. R., Lockhart, T., Parry, I., Pueyo, L., Rice, E., Roberts, L. C., Roberts, J., Shao, M., Sivaramakrishnan, A., Soummer, R., Vasisht, G., Vescelus, F., Wallace, J. K., Zhai, C., & Zimmerman, N. 2012, in Society of Photo-Optical Instrumentation Engineers (SPIE) Conference Series, Vol. 8447, Society of Photo-Optical Instrumentation Engineers (SPIE) Conference Series

Patience, J., King, R. R., de Rosa, R. J., & Marois, C. 2010, Astronomy and Astrophysics, 517, A76

Perrin, M., Maire, J., Ingraham, P. J., Savransky, D., Millar-Blanchaer, M., Wolff,

S. G., Ruffio, J.-B., Wang, J. J., Draper, Z. H., Sadakuni, N., Marois, C., Fitzgerald, M. P., Macintosh, B., Graham, J. R., Doyon, R., Larkin, J. E., Chilcote, J. K., Goodsell, S. J., Palmer, D. W., Labrie, K., Beaulieau, M., Rosa, R. J. D., Greenbaum, A. Z., Hartung, M., Hibon, P., Konopacky, Q. M., Lafreniere, D., Lavigne, J.-F., Marchis, F., Patience, J., Pueyo, L. A., Soummer, R., Thomas, S. J., Ward-Duong, K., & Wiktorowicz, S. 2014, in

Perrin, M. D., Graham, J. R., Larkin, J. E., Wiktorowicz, S., Maire, J., Thibault, S., Fitzgerald, M. P., Doyon, R., Macintosh, B. A., Gavel, D. T., Oppenheimer, B. R., Palmer, D. W., Saddlemyer, L., & Wallace, J. K. 2010, in

Peters, M. A., Groff, T., Kasdin, N. J., McElwain, M. W., Galvin, M., Carr, M. A., Lupton, R., Gunn, J. E., Knapp, G., Gong, Q., Carlotti, A., Brandt, T., Janson, M., Guyon, O., Martinache, F., Hayashi, M., & Takato, N. 2012, in Society of Photo-Optical Instrumentation Engineers (SPIE) Conference Series, Vol. 8446, Society of Photo-Optical Instrumentation Engineers (SPIE) Conference Series

Pollack, J. B., Hubickyj, O., Bodenheimer, P., Lissauer, J. J., Podolak, M., & Greenzweig, Y. 1996, Icarus, 124, 62

Poyneer, L. A., Bauman, B., Cornelissen, S., Isaacs, J., Jones, S., Macintosh, B. A., & Palmer, D. W. 2011, in Society of Photo-Optical Instrumentation Engineers (SPIE) Conference Series, Vol. 7931, Society of Photo-Optical Instrumentation Engineers (SPIE) Conference Series

Poyneer, L. A. & Macintosh, B. 2004, Journal of the Optical Society of America A, 21, 810

Poyneer, L. A. & Macintosh, B. A. 2003, in Society of Photo-Optical Instrumentation Engineers (SPIE) Conference Series, Vol. 5169, Astronomical Adaptive Optics Systems and Applications, ed. R. K. Tyson & M. Lloyd-Hart, 190–200

Rameau, J., Chauvin, G., Lagrange, A.-M., Boccaletti, A., Quanz, S. P., Bonnefoy, M., Girard, J. H., Delorme, P., Desidera, S., Klahr, H., Mordasini, C., Dumas, C., & Bonavita, M. 2013, Astrophysical Journal, Letters, 772, L15

Schneider, G. & Silverstone, M. 2003, in Astronomical Society of the Pacific Conference Series, Vol. 291, Hubble's Science Legacy: Future Optical/Ultraviolet Astronomy from Space, ed. K. R. Sembach, J. C. Blades, G. D. Illingworth, & R. C. Kennicutt, Jr., 69

Sivaramakrishnan, A. & Oppenheimer, B. R. 2006, , 647, 620

Sivaramakrishnan, A., Soummer, R., Carr, G. L., Dorrer, C., Bolognesi, A., Zimmerman, N., Oppenheimer, B. R., Roberts, R., & Greenbaum, A. 2009, in Society of Photo-Optical Instrumentation Engineers (SPIE) Conference Series, Vol. 7440, Society of Photo-Optical Instrumentation Engineers (SPIE) Conference Series

Smith, B. A. & Terrile, R. J. 1984, Science, 226, 1421

Snellen, I. A. G., Brandl, B. R., de Kok, R. J., Brogi, M., Birkby, J., & Schwarz, H. 2014, Nature, 509, 63

Soummer, R., Pueyo, L., & Larkin, J. 2012, Astrophysical Journal, Letters, 755, L28

Soummer, R., Sivaramakrishnan, A., Pueyo, L., Macintosh, B., & Oppenheimer, B. R. 2011, Astrophysical Journal, 729, 144

Spergel, D., Gehrels, N., Breckinridge, J., Donahue, M., Dressler, A., Gaudi, B. S., Greene, T., Guyon, O., Hirata, C., Kalirai, J., Kasdin, N. J., Moos, W., Perlmutter, S., Postman, M., Rauscher, B., Rhodes, J., Wang, Y., Weinberg, D., Centrella, J., Traub, W., Baltay, C., Colbert, J., Bennett, D., Kiessling, A., Macintosh, B., Merten, J., Mortonson, M., Penny, M., Rozo, E., Savransky, D., Stapelfeldt, K., Zu, Y., Baker, C., Cheng, E., Content, D., Dooley, J., Foote, M., Goullioud, R., Grady, K., Jackson, C., Kruk, J., Levine, M., Melton, M., Peddie, C., Ruffa, J., & Shaklan, S. 2013, ArXiv e-prints

Thébault, P. & Beust, H. 2001, Astronomy and Astrophysics, 376, 621

Thibault, S., Vallée, P., Artigau, E., Maire, J., Doyon, R., Lavigne, J.-F., & Larkin, J. 2010, in

van Leeuwen, F. 2007, Astronomy and Astrophysics, 474, 653

Wallace, J. K., Burruss, R. S., Bartos, R. D., Trinh, T. Q., Pueyo, L. A., Fregoso, S. F., Angione, J. R., & Shelton, J. C. 2010, in Society of Photo-Optical Instrumentation Engineers (SPIE) Conference Series, Vol. 7736, Society of Photo-Optical Instrumentation Engineers (SPIE) Conference Series

Wang, J. J., Rajan, A., Graham, J. R., Savransky, D., Ingraham, P. J., Ward-Duong, K., Patience, J., Rosa, R. J. D., Bulger, J., Sivaramakrishnan, A., Perrin, M. D., Thomas, S. J., Sadakuni, N., Greenbaum, A. Z., Pueyo, L., Marois, C., Oppenheimer, B. R., Kalas, P., Cardwell, A., Goodsell, S., Hibon, P., & Rantakyrö, F. T. 2014, in

Wright, J. T., Fakhouri, O., Marcy, G. W., Han, E., Feng, Y., Johnson, J. A., Howard, A. W., Fischer, D. A., Valenti, J. A., Anderson, J., & Piskunov, N. 2011, Publications of the ASP, 123, 412

Yelda, S., Lu, J. R., Ghez, A. M., Clarkson, W., Anderson, J., Do, T., & Matthews, K. 2010, Astrophysical Journal, 725, 331

Zuckerman, B., Song, I., Bessell, M. S., & Webb, R. A. 2001, Astrophysical Journal, Letters, 562, L87